University of Regensburg
Quantum Transport and Dissipation

Spin-orbit induced dynamics in driven single molecule junctions

Master Thesis

by

Moritz Frankerl

Supervisor: PD. Dr. Andrea Donarini
Second referee: Prof. Dr. Jascha Repp

October 2019

Für Papa
The show must go on.

Contents

1. Introduction

In 1965 Gordon Moore predicted that the number of transistors in an integrated circuit would double every year for the next ten years [1]. This prediction became self fulfilling and was labeled "Moore's law" later. It held for a much longer time than the predicted ten years but as transistors get smaller quantum effects play a larger role and thus Moore's law will slow down [2]. To keep up technological progress it is, therefore, necessary to find alternatives to the predominance of silicon based devices.
A possible solution to further downsize electronic devices is molecular electronics. The size of molecules is on the (sub) nanoscale and they are perfectly reproducible. The starting point for the research of molecular electronics was the proposal of a single molecule rectifier by Aviram and Ratner [3]. However, it took 21 years until the first successful electric contact with an individual molecule was reported by Joachim et. al. [4]. They used a scanning tunnelling microscope to measure the dependence of the current flowing through a C_{60} molecule with respect to the tip-molecule distance. Seminal experiments [5, 6] have boosted intense investigations in the transport properties of single molecule junctions [7–10]. A very useful tool to probe single molecule junctions is the scanning tunnelling microscope (STM). It was invented by Binnig and Rohrer in 1982 [11] and is widely used to study surfaces with atomic resolution [12, 13], to manipulate single atoms [14, 15] and to perform spectroscopy on single atoms [16]. It is a very useful tool to realize single molecule junctions due to its high spatial resolution.
In semiconductors a widely used technique to obtain spectral information directly in the time domain is THz-spectroscopy [17]. The reason is that in many-body systems energy differences between relevant states are usually of the order of the energy of a THz photon.
A new trend is to combine the ultrafast temporal resolution of THz spectroscopy with the high spatial resolution of an STM [18–20].
In this thesis, we consider a single copper phthalocyanine molecule, from now on denoted as CuPc, in a THz-STM junction. We focus on the spin-orbit induced dynamics in this junction and how to make a connection between them and charge measurements in pump probe experiments.
In the second chapter we derive a many-body Hamiltonian able to describe CuPc and analyse its spectrum. Furthermore, we explore how to model the leads of our single molecule junction and describe the tunnelling processes.
The third chapter is used to derive a transport formalism for the THz-STM. We start by deriving a transport formalism for the reduced density matrix and neglect the special geometry and the effect of the THz laser pulses in the beginning. After having derived our general transport formalism, we discuss how to incorporate these effects into the

transport formalism.
The fourth chapter is dedicated to a simplified model of CuPc in the THz-STM set up. We neglect the spin in this chapter and only model the molecule by two quasi degenerate orbitals. We investigate the pseudospin dynamics of this model to gain a better understanding of what to expect from the full model. Furthermore, we investigate pump probe schemes to obtain a connection between the internal dynamics and experimentally possible charge measurements.
In the fifth chapter the numerical investigation of the full model for the molecule in the junction is presented. The spin orbit driven dynamics are investigated and again pump probe schemes as a possible way for electronic measurements of the dynamics are explored.
The sixth chapter is used to investigate the spin-orbit driven dynamics with an analytical approach. Therefore, we show how to expand the density matrix in its irreducible components and how to get information about the spin and pseudospin dynamics from this approach.

2. Theoretical Model of Copper Phthalocyanine

To describe any quantum mechanical system one needs to know its Hamiltonian. In many-body problems it is quite a hard task to then solve the resulting Schrödinger equation since the possible solutions scale exponentially with the degrees of freedom. There are many electrons in molecules so one needs to treat them in a many-body framework. A useful tool to describe many-body problems is the second quantization formalism. In the following chapter a scheme will be presented which allows the derivation of a many-body molecular Hamiltonian, in second quantization, which can be treated with analytical and numerical methods. We will present this scheme on the example of Copper Phthalocyanine but there is no fundamental reason why it should not be applicable to other molecules. Furthermore, we will discuss how to model the leads and tunnelling processes for our transport calculations.

2.1. General many-body Hamiltonian

For a molecule with N_e electrons and N_n nuclei the general many-body Hamiltonian in first quantization reads [21]

$$\hat{H} = \hat{T}_n + \hat{T}_e + \hat{V}_{n-n} + \hat{V}_{e-e} + \hat{V}_{e-n}. \tag{2.1}$$

The individual parts are the kinetic energy of the nuclei with mass M_n

$$\hat{T}_n = \sum_{k=1}^{N_n} \frac{\hat{P}_\alpha^2}{2M_n}, \tag{2.2}$$

the kinetic energy of the electrons with the electron mass m_e

$$\hat{T}_e = \sum_{i=1}^{N_e} \frac{\hat{p}_i^2}{2m_e}, \tag{2.3}$$

the interactions between the nuclei

$$\hat{V}_{n-n} = \sum_{k<l} v_{n-n} |\hat{R}_\alpha - \hat{R}_\beta|, \tag{2.4}$$

the electron-electron interactions

$$\hat{V}_{e-e} = \sum_{i<j} v_{e-e}|\hat{r}_i - \hat{r}_j|, \tag{2.5}$$

and the interactions between electrons and nuclei

$$\hat{V}_{e-n} = \sum_{i,k} v_{e-n}\left|\hat{r}_i - \hat{R}_\alpha\right|. \tag{2.6}$$

$\hat{R}_\alpha$ and $\hat{P}_\alpha$ are the position and momentum operators of the nucleus α, whereas $\hat{r}_i$ and $\hat{p}_i$ are the ones of the i-th electron. Unfortunately, solving the Schrödinger equation for the Hamiltonian in Eq. (2.1) completely is not feasible for systems of realistic size. The reason is that too many electrons and nuclei are involved and the resulting Hilbert space is too big. To obtain a solvable problem we will concentrate on the valence electrons and incorporate the core ones with the nuclei which are thus replaced by atomic ions. Furthermore, a commonly used simplification is the Born-Oppenheimer approximation.[22] It is based on the observation that the masses of the ions are much larger than those of the electrons, i.e. $M_i > m_e$, which makes them move slower. This fact allows us to decouple the movement of the ions from that of the electrons. We will concentrate in this thesis on the electronic dynamics and assume the ions to be "frozen" in equilibrium positions.

2.1.1. Second quantization formulation in the atomic basis

With the Born-Oppenheimer approximation and complete freezing of the ions, we can write Eq. (2.1) in second quantization as [23]

$$\begin{aligned}\hat{H} = &\sum_{\substack{\alpha\beta\\ln}}\sum_{\sigma\sigma'}\langle\alpha l\sigma|\frac{\hat{p}^2}{2m_e} + \sum_\gamma \hat{V}_\gamma|\beta n\sigma'\rangle \hat{d}^\dagger_{\alpha l\sigma}\hat{d}_{\beta n\sigma'}\\ &+\frac{1}{2}\sum_{\substack{\alpha\beta\gamma\delta\\mnpq}}\sum_{\sigma\sigma'} V^{mnpq}_{\alpha\beta\gamma\delta}\hat{d}^\dagger_{\alpha l\sigma}\hat{d}^\dagger_{\gamma p\sigma'}\hat{d}_{\delta q\sigma'}\hat{d}_{\beta n\sigma}.\end{aligned} \tag{2.7}$$

Here $\hat{d}^\dagger_{\alpha l\sigma}$ is the creation operator of an electron in an atomic valence orbital at position $\mathbf{r}_\alpha$ with angular momentum l and spin σ. $\hat{V}_\gamma$ is the nuclear (attractive) potential stemming from the ion at position $\mathbf{r}_\gamma$. The Hamiltonian in Eq. (2.7) consists of a single particle part and electron-electron interactions. Let us first focus on the single particle part. We rewrite it as

$$H^0 = \sum_{\substack{\alpha\beta\\ln}}\sum_{\sigma\sigma'}\left(h_{\alpha l\sigma,\beta n\sigma'} + V^{\text{ion}}_{\alpha l\sigma,\beta n\sigma'}\right)\hat{d}^\dagger_{\alpha l\sigma}\hat{d}_{\beta n\sigma'}, \tag{2.8}$$

accounting for the crystal field corrections with the single particle part,

$$V^{\text{ion}}_{\alpha l\sigma,\beta n\sigma'} = \sum_{\substack{\gamma \\ \gamma\neq\alpha,\beta}} \langle \alpha l\sigma | V_\gamma | \beta n\sigma' \rangle \,. \tag{2.9}$$

The single particle part can be represented in matrix notation by

$$h_{\alpha l\sigma,\beta n\sigma'} = \varepsilon_{\alpha l\sigma}\delta_{\alpha\beta}\delta_{ln}\delta_{\sigma\sigma'} + b_{\alpha l\sigma,\beta n\sigma'}(1-\delta_{\alpha\beta}). \tag{2.10}$$

Here $\varepsilon_{\alpha l\sigma}$ is the on site energy and $b_{\alpha l\sigma,\beta n\sigma'}$ are the hopping integrals between atoms. To set up the hopping integrals we use the linear combination of atomic orbitals (LCAO) approach by Slater and Koster [24]. The hopping integrals then adopt the following form

$$b_{\alpha l\sigma,\beta n\sigma'} = \sum_\xi V_{ln\xi}(r_{\alpha\beta}) f_\xi(\varphi_{\alpha\beta}). \tag{2.11}$$

In this representation l and n are the sub-shells of the orbitals $|\alpha l\rangle$ and $|\beta n\rangle$, ξ denotes the character of the bond between the sub shells of orbitals l and n. The possible values are $\xi = \sigma, \pi, \delta$. To determine the type of a molecular bond one can take a cross section along the bonding axis and compare it to the cross section of a s, p or d type atomic orbital. A σ bond will resemble a s-orbital, a π bond a p-orbital and a δ bond a d-orbital, in their respective cross section [25]. The matrix elements $V_{ln\xi}$ depend only on the distance and can be calculated by the method proposed by Froyen and Harrison [26]. The $f_\xi(\varphi_{\alpha\beta})$ depend on the angle $\varphi_{\alpha\beta}$ which is the angle between the vector connecting the two bonding atoms $\mathbf{r}_{\alpha\beta} = \mathbf{r}_\beta - \mathbf{r}_\alpha$ and the different coordinate axis corresponding to the involved orbitals. They can be found in the paper by Slater and Koster [24].
The second part in Eq. (2.7) describes the Coulomb interaction between the electrons. $V^{mnpq}_{\alpha\beta\gamma\delta}$ is the matrix element of this interaction and has the following form

$$V^{mnpq}_{\alpha\beta\gamma\delta} = \int \mathrm{d}^3r_1 \mathrm{d}^3r_2 \Phi^*_{\alpha l}(\mathbf{r}_1)\Phi_{\beta n}(\mathbf{r}_1) V(r_{12}) \Phi^*_{\gamma p}(\mathbf{r}_2)\Phi_{\delta q}(\mathbf{r}_2) \tag{2.12}$$

Here $V(r) = \frac{e^2}{4\pi\varepsilon_0 r}$ is the Coulomb potential and $r_{12} \equiv |\mathbf{r}_1 - \mathbf{r}_2|$ is the norm of the difference between the positions $\mathbf{r}_1$ and $\mathbf{r}_2$. The wave functions are $\Phi_{\alpha l}(\mathbf{r}) = \langle \mathbf{r} | \alpha l \rangle$ where we have omitted the spin indices.

2.1.2. Transformation to the molecular orbital basis

We assume that the states $|\alpha l\sigma\rangle$ and $|\beta n\sigma'\rangle$ are orthogonal, i.e.

$$\langle \alpha l\sigma | \beta n\sigma' \rangle = \delta_{\alpha\beta}\delta_{ln}\delta_{\sigma\sigma'}. \tag{2.13}$$

This is not true in general since they can be centered on different atoms and thus have a finite overlap. Numerical checks performed in Ref. [23] showed no qualitative difference

by using this approximation because the overlaps are very small. Diagonalizing the matrix $\mathbf{h}$ of elements $h_{\alpha l\sigma,\beta n\sigma'}$ yields the molecular orbital basis $\{|i\sigma\rangle\}$ which can be expressed in terms of the atomic basis as

$$|i\sigma\rangle = \sum_{\alpha l} c_{i\alpha l}|\alpha l\sigma\rangle, \tag{2.14}$$

with the expansion coefficients $c_{i\alpha l}$. In this basis, the Hamiltonian from Eq. (2.7) is

$$\begin{aligned}\hat{H}_{\mathrm{mol}} = &\sum_{ij\sigma}\left(\varepsilon_i\delta_{ij} + V_{ij}^{\mathrm{ion}}\right)\hat{d}_{i\sigma}^{\dagger}\hat{d}_{j\sigma} \\ &+\frac{1}{2}\sum_{ijkl}\sum_{\sigma\sigma'} V_{ijkl}\hat{d}_{i\sigma}^{\dagger}\hat{d}_{k\sigma'}^{\dagger}\hat{d}_{l\sigma'}\hat{d}_{j\sigma}.\end{aligned} \tag{2.15}$$

It consists of the single particle eigenenergies ε_i, the transformed crystal field corrections

$$V_{ij}^{\mathrm{ion}} = \sum_{\substack{\alpha\beta\\ ln}} c_{i\alpha l}^{*} c_{j\beta n} V_{\alpha l,\beta n}^{\mathrm{ion}} \tag{2.16}$$

and the matrix elements of the Coulomb interaction

$$V_{ijkl} = \int \mathrm{d}^3 r_1 \mathrm{d}^3 r_2 \psi_i^{*}(\mathbf{r}_1)\psi_j(\mathbf{r}_1)V(r_{12})\psi_k^{*}(\mathbf{r}_2)\psi_l(\mathbf{r}_2). \tag{2.17}$$

The molecular basis has some advantages over the atomic one. Firstly, we can take the single particle energies of the molecule and fill the molecular orbitals according to the Aufbau principle. By doing this we will obtain the energy of the highest occupied orbital of the molecule and also an approximate solution to the electronic many-body problem. Furthermore, it allows us to make a huge simplification in the calculations by enabling us to choose an appropriate set of orbitals which are relevant to transport and neglect the rest. We do this by splitting the orbitals in $\mathrm{N_{fr}}$ frozen orbitals and $\mathrm{N_d}$ dynamical orbitals. In the frozen orbitals we include $\mathrm{N_f}$ orbitals which are always double occupied, as well as $\mathrm{N_e}$ orbitals which are always empty. The occupation of the $\mathrm{N_d}$ dynamical orbitals depends on the chemical potential of the molecule and the possibility of exchange with the environment. In the smaller space of the dynamical orbitals we will then incorporate electronic correlations in our calculations to obtain the full solution of the many-body problem.

2.2. A many-body Hamiltonian for Copper Phthalocyanine

Copper Phthalocyanine (from now an denoted as CuPc) is a planar organic macrocycle which consists of an inner ring, made up by alternating nitrogen and carbon atoms. It possesses four outer benzene rings which are covalently bond to the inner ring. In

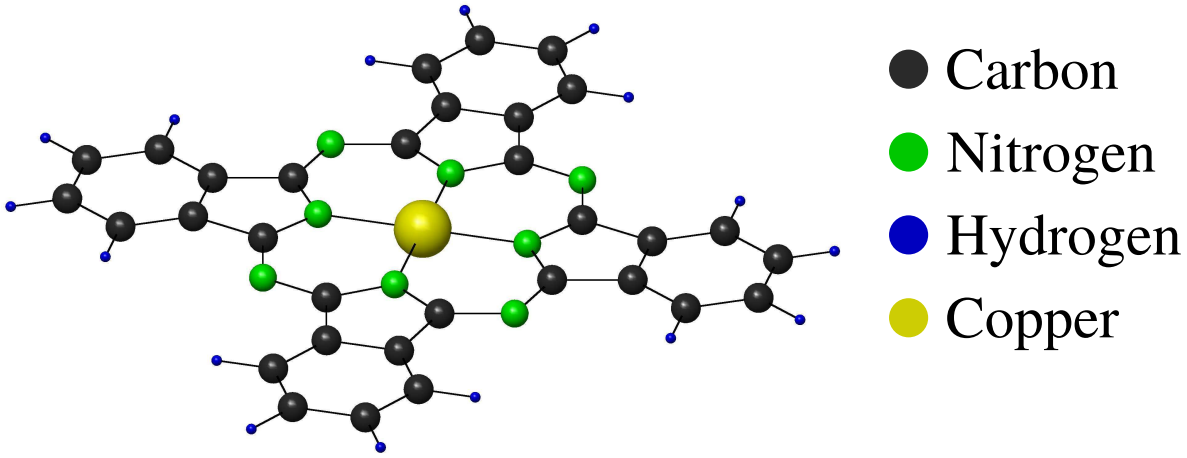

Figure 2.1.: Schematic depiction of a CuPc molecule. Taken from Ref. [23].

the center sits a Copper atom, see Fig. 2.1. However, there are many other classes of metal Phthalocyanines with a different atom in the center, e.g. Mn, Co, Fe etc. CuPc possesses 195 valence electrons which come from the 1s, 2s and 2p orbitals of the organic ligand, i.e. the nitrogen, carbon and hydrogen atoms and from the 3d and 4s orbitals of the copper center. In this section we will make use of the molecular orbital basis introduced in the previous section to derive a many-body Hamiltonian for CuPc which is able to account for single particle energies, electron-electron correlations and also for spin-orbit interaction. The general Hamiltonian will have the form

$$\hat{H}_{\text{mol}} = \hat{H}_0 + \hat{V}_{\text{ee}} + \hat{V}_{\text{SO}}, \tag{2.18}$$

with the single particle part $\hat{H}_0$, the electron-electron interactions $\hat{V}_{\text{ee}}$ and the spin orbit interaction $\hat{V}_{\text{SO}}$. Since this work is essentially an extension of the work done by Siegert et al. [23, 27] we will closely follow this works in the following sections.

2.2.1. Single particle spectrum

Considering that we want to use the methodology introduced in the first two sections to build a Hamiltonian for the CuPc molecule, in the molecular orbital basis, the first thing to do is to calculate the single particle Hamiltonian which was presented in Eq. (2.10). We will use the LCAO schemes introduced by Slater-Koster [24] and Froyen-Harrison [26] so we need to determine the bonding types between the valence electrons of CuPc. The molecule is planar, thus its orbitals can be classified into a σ and π system depending on their even or odd parity with respect to a reflection symmetry operation. Accordingly the s, $2p_x$, and $2p_x$ orbitals of the ligand are part of the σ system. The $2p_z$ orbitals are contained in the π system. The $3d_{xy}$, $3d_{x^2-y^2}$, $3d_{z^2}$ and 4s orbitals of the copper atom are part of the σ system. The remaining two d-orbitals, namely $3d_{xz}$ and $3d_{yz}$ belong to the π system instead. Furthermore, we need the geometrical parameters which were taken from [28] and the on site energies from [29]. Then, the single particle

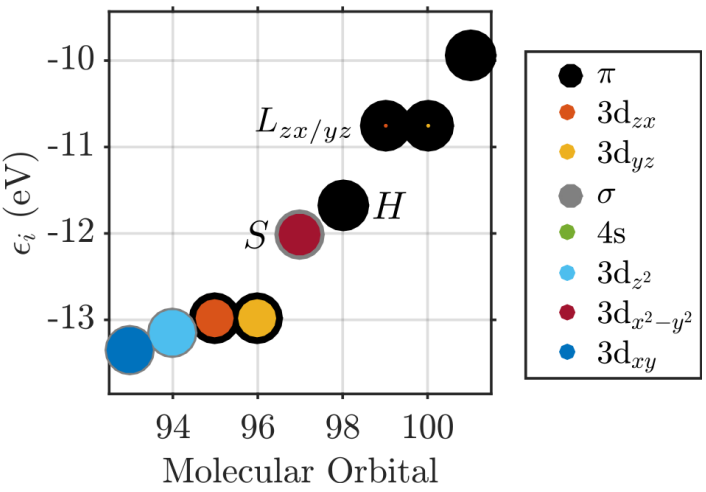

Figure 2.2.: CuPc Single particle spectrum in the interesting region. The color of the inner circle depicts the π ,black, or the σ,grey, bonding character. The inner circle shows the type of the orbital via its color and the weight on the metal center via the diameter. The energies of the SOMO, HOMO and the two LUMOs are marked by S, H, and $L_{xz/yz}$. Taken from Ref. [23].

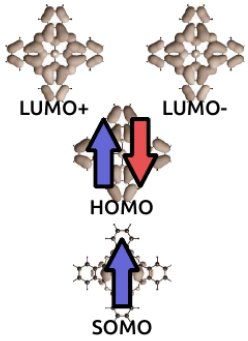

Figure 2.3.: Ground state configuration in the frontier orbitals for the neutral molecule. The arrows represent electrons with spin up and spin down. Taken from Ref. [23].

Hamiltonian **h** can be numerically diagonalized to yield the single particle energies ε_i, shown in Fig. 2.2, and also reveal the molecular orbital basis $|i\rangle = \sum_\alpha c_{i\alpha}|\alpha\rangle$.
CuPc has 195 valence electrons, hence there is a molecular orbital which is occupied by a single electron. By using the Aufbau principle we assume that this is the 98th molecular orbital. Here we can see why using the single particle energies and the Aufbau principle is not enough to describe a many-body system, by anticipating results from the next sections. The reason is that even though the 97th orbital has a lower single particle energy its charging energy is much higher than the one of the 98th, see Table 2.2.1. Therefore, in reality the 97th orbital is singly occupied, whereas the 98th is doubly occupied. We will thus, like in the literature [30–32], refer to the 97th orbital as SOMO (single occupied molecular orbital) and to the 98th as HOMO (highest occupied molecular orbital). The next two orbitals which are degenerate in their single particle energy are the two lowest unoccupied molecular orbitals ($LUMO_{xz}$ and $LUMO_{yx}$). These four orbitals will form our dynamical orbitals, also called frontier orbitals, as introduced in Sec. 2.1.2. They are displayed in Fig. 2.4. The single particle energies of the frontier orbitals are $\varepsilon_S = -12.0$ eV, $\varepsilon_H = -11.7$ eV and $\varepsilon_{L\pm} = -10.7$ eV. This means that we assume the lower 96 orbitals to be doubly filled at all times. Moreover, we assume the orbitals above the two LUMOs to be empty. These two blocks of orbitals will make up the set of frozen orbitals and will be ignored in our transport calculations as discussed in Sec. 2.1.2. Following this analysis we can conclude that the number of electrons in the frontier orbitals is, in the neutral state, $N_0 = 3$. The filling of the frontier orbitals in the neutral state can be seen in Fig. 2.3. We will see in the following sections that by treating the full many-body problem this filling of the frontier orbitals is the correct one.

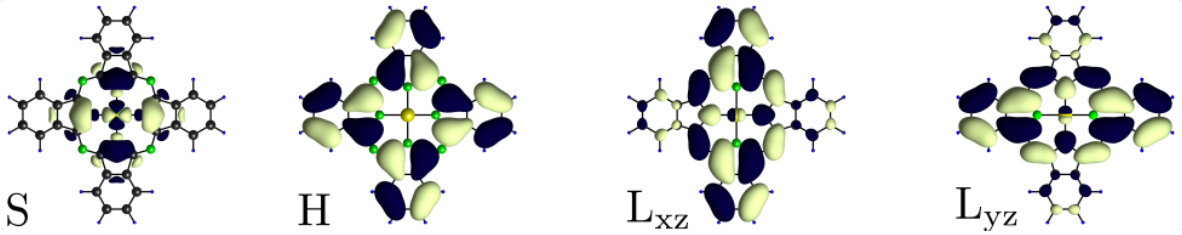

Figure 2.4.: Images of the four dynamical orbitals: SOMO, HOMO, LUMO_{xz} and LUMO_{yz}. Taken from Ref. [23].

We can see from figs. 2.2 and 2.4 that the frontier orbitals have different contributions on the copper center and the ligand. To distinguish them we introduce $|\,\rangle_{Cu}$ and $|\,\rangle_{Pc}$. This discrimination will become useful in the analysis of spin-orbit effects. This allows us to write

$$|L_{xz/yz}\rangle = \sqrt{1-c_L^2}|L_{xz/yz}\rangle_{Pc} + c_L|3d_{xz/yz}\rangle_{Cu}, \tag{2.19}$$

where $c_L \approx 0.097$ is the contribution of the LUMOs, $|L_{xz}\rangle$ and$|L_{yz}\rangle$, on the $3d_{xz}$ and $3d_{yz}$ orbitals of the Copper atom. The SOMO can, in this notation, be expressed as

$$|S\rangle = \sqrt{1-c_S^2}|S\rangle_{Pc} + c_S|3d_{x^2-y^2}\rangle_{Cu}, \tag{2.20}$$

where $c_S \approx 0.9$ is the contribution of the SOMO on the $3d_{x^2-y^2}$ orbital in the center. Due to symmetry reasons the HOMO does not contribute to the metallic center. Therefore it is just expressed as

$$|H\rangle = |H\rangle_{Pc}. \tag{2.21}$$

2.2.2. Imaginary representation of the frontier orbitals

The four frontier orbitals can be represented in a rotationally symmetric basis. For the SOMO and HOMO this representation is the same as before whereas the complex LUMOs are obtained via a linear combination of the two degenerate LUMOs $|L_{xz/yx}\rangle$ yielding

$$|L\pm\rangle = \frac{1}{\sqrt{2}}\left(|L_{xz}\rangle \pm i|L_{yz}\rangle\right). \tag{2.22}$$

The complex LUMO orbitals are depicted in Fig. 2.5. In the rotationally symmetric basis we can classify them by the phase they acquire under a rotation of $\frac{\pi}{2}$ around a main rotational symmetry axis, e.g. the x-axis. This phase is $\Phi_S = \pi$, $\Phi_H = 0$ and $\Phi_{L\pm} = \pm\frac{\pi}{2}$, for the SOMO, HOMO and the LUMOs.

Let us take a look at the Coulomb interaction which was introduced in Eq. (2.17).

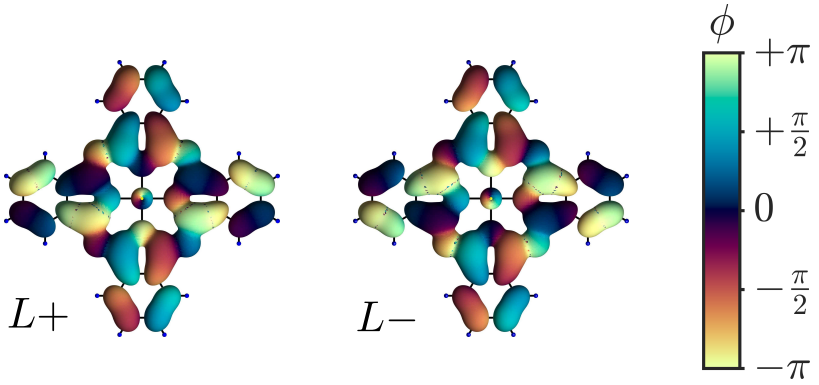

Figure 2.5.: The LUMOs in their complex representation. The color describes the complex phase. Taken from Ref. [23].

The potential

$$V(r_{12}) = \frac{1}{4\pi\varepsilon_0}\frac{e^2}{|\mathbf{r}_1 - \mathbf{r}_2|} \tag{2.23}$$

only depends on the distance between two electrons and is therefore rotationally invariant. We can define a rotation R which shall be again a rotation of $\frac{\pi}{2}$ around the main rotational symmetry axis of the molecule with $\mathbf{r}' = R^{-1}\mathbf{r}$. This rotation has the effect

$$R|j\rangle = \mathrm{e}^{\mathrm{i}\Phi_j}|j\rangle, \tag{2.24}$$

where $\{|j\rangle\}$ are now the four dynamical orbitals. Under the action of R, the wave functions acquire the phase

$$\psi_j(R^{-1}\mathbf{r}) = \psi_j(\mathbf{r}') = \langle\mathbf{r}'|j\rangle = \langle\mathbf{r}|R|j\rangle = \mathrm{e}^{\mathrm{i}\Phi_j}\langle\mathbf{r}|j\rangle = \mathrm{e}^{\mathrm{i}\Phi_j}\psi_j(\mathbf{r}). \tag{2.25}$$

For the matrix elements of the Coulomb interaction one can deduce now

$$\begin{aligned} V_{ijkl} &= \int \mathrm{d}^3r_1 \int \mathrm{d}^3r_2 \psi_i^*(\mathbf{r}_1)\psi_j(\mathbf{r}_1)V(r_{12})\psi_k^*(\mathbf{r}_2)\psi_l(\mathbf{r}_2) \\ &= \int \mathrm{d}^3r_1' \int \mathrm{d}^3r_2' \psi_i^*(\mathbf{r}_1')\psi_j(\mathbf{r}_1')V(r_{12}')\psi_k^*(\mathbf{r}_2')\psi_l(\mathbf{r}_2') \\ &= \int \mathrm{d}^3r_1 \int \mathrm{d}^3r_2 \psi_i^*(\mathbf{r}_1)\mathrm{e}^{-\mathrm{i}\Phi_i}\psi_j(\mathbf{r}_1)\mathrm{e}^{\mathrm{i}\Phi_j}V(r_{12})\psi_k^*(\mathbf{r}_2)\mathrm{e}^{-\mathrm{i}\Phi_k}\psi_l(\mathbf{r}_2)\mathrm{e}^{\mathrm{i}\Phi_l} \\ &= \mathrm{e}^{-\mathrm{i}(\Phi_i-\Phi_j+\Phi_k-\Phi_l)}V_{ijkl}. \end{aligned} \tag{2.26}$$

This relation puts some constraints on the orbitals which can be coupled by the Coulomb interaction. Their phases, under the rotation R, have to fulfill

$$\Phi_i - \Phi_j + \Phi_k - \Phi_l = 2n\pi, \ n \in \mathbb{Z} \tag{2.27}$$

in order to have non-vanishing contributions. This constraint reduces the number of matrix elements V_{ijkl} to take into account in the calculations.

For the crystal field correction V_{ij}^{ion} we see:

$$V^{\text{ion}} = R^{-1} V_{ij}^{\text{ion}} R = R^{-1} \sum_{\gamma} \langle i | V_{\gamma} | j \rangle \, R = \mathrm{e}^{-i(\Phi_i - \Phi_j)} V_{ij}^{\text{ion}} \tag{2.28}$$

The phases of the frontier orbitals are all different so we can conclude from Eq. (2.28) that the crystal field correction is diagonal in our basis.

$$V_{ij}^{\text{ion}} = V_{ij}^{\text{ion}} \delta_{ij} \tag{2.29}$$

In our theory the crystal field corrections are four free parameters and need to be fitted to experimental data. This gives us a way to express the first two terms of Eq. (2.18) in the frontier orbital basis of CuPc. Those terms then read:

$$\begin{aligned} \hat{H}_{\text{mol}}^{(1)} = & \sum_i (\varepsilon_i + \delta_i) \, \hat{n}_i + \sum_i U_i \hat{n}_{i\uparrow} \hat{n}_{i\downarrow} + \frac{1}{2} \sum_{[ij]} U_{ij} \hat{n}_i \hat{n}_j \\ & - \frac{1}{2} \sum_{[ij]} \sum_{\sigma} J_{ij}^{\text{ex}} \left(\hat{n}_{i\sigma} \hat{n}_{j\sigma} - \hat{d}_{i\sigma}^{\dagger} \hat{d}_{j\bar{\sigma}}^{\dagger} \hat{d}_{i\bar{\sigma}} \hat{d}_{j\sigma} \right) \\ & + \frac{1}{2} \sum_{[ij]} \sum_{\sigma} J_{ij}^{P} \hat{d}_{i\sigma}^{\dagger} \hat{d}_{i\bar{\sigma}}^{\dagger} \hat{d}_{j\bar{\sigma}} \hat{d}_{j\sigma} \\ & + \frac{1}{2} \sum_{[ijk]} \sum_{\sigma} \left(\tilde{J}_{ijk}^{P} \hat{d}_{i\sigma}^{\dagger} \hat{d}_{i\bar{\sigma}}^{\dagger} \hat{d}_{j\bar{\sigma}} \hat{d}_{k\sigma} + \text{h.c.} \right) \end{aligned} \tag{2.30}$$

The indices i,j and k denote the frontier orbitals SOMO, HOMO and the LUMOs, whereas σ stands for the spin. We assume a constant shift for the crystal field corrections with value $\delta = \delta_i = 1.83$ eV. The notation $[ijk]$ denotes that the indices have to run over different orbitals and $\hat{n}_i$ counts the number of electrons in an orbital irrespective of its spin. We introduced some abbreviations for the Coulomb matrix elements in Eq. (2.30) which are the following: $U_i = V_{iiii}$ denotes the orbital Coulomb interaction, $U_{ij} = V_{iijj}$ the Coulomb interaction between different orbitals, $J_{ij}^{\text{ex}} = V_{ijji}$ the exchange interaction, $J_{ij}^{P} = V_{ijij}$ is the pair hopping contribution and lastly the split pair hopping is $\tilde{J}_{ijk}^{P} = V_{ijik}$. The Coulomb integrals with four different indices are very small and are thus neglected. The values for the integrals have been taken from Ref. [23] where they have been calculated by Monte Carlo integration. The values of the non vanishing integrals can be seen in table 2.2.1. We can see that the charging energy of the SOMO, U_{S}, is more than five times larger than the one of the HOMO, U_{H}, thus it becomes clear why the HOMO is doubly occupied although it has a higher single particle energy.

U_{S}	11.352 eV	$J^{\mathrm{ex}}_{\mathrm{HL}} = -\tilde{J}^{P}_{\mathrm{H}+-}$	548 meV
U_{H}	1.752 eV	J^{ex}_{+-}	258 meV
$U_{+/-} = U_{+-}$	1.808 eV	J^{P}_{+-}	168 meV
U_{SH}	1.777 eV	$J^{\mathrm{ex}}_{\mathrm{SL}} = -\tilde{J}^{P}_{\mathrm{S}+-}$	9 meV
U_{SL}	1.993 eV	$J^{\mathrm{ex}}_{\mathrm{SH}} = J^{P}_{\mathrm{SH}}$	2 meV
U_{HL}	1.758 eV		

Table 2.2.1.: Coulomb integrals between the frontier orbitals, SOMO(S), HOMO(H), LUMO+ (+) and LUMO- (-). Taken from Ref. [23].

2.2.3. Spin-orbit interaction in the frontier orbital basis

In this section we will derive the last missing part of our Hamiltonian in Eq. (2.18), which is the spin-orbit interaction (from now on SOI). The SOI operator reads in the atomic basis

$$\hat{V}_{\mathrm{SO}} = \sum_{\alpha, l_\alpha} \xi_{l_\alpha} \hat{\mathbf{L}}_\alpha \hat{\mathbf{S}}_\alpha, \tag{2.31}$$

with α running over all atoms and l_α denoting the shells of atom α. Since, ξ_{l_α} is negligible for the H,C, and N atoms we evaluate Eq. (2.31) only on the central copper atom, i.e. $\alpha = \mathrm{Cu}$ and $l = 2$ corresponding to the d-orbitals, we obtain in second quantization

$$\begin{aligned} \hat{V}_{\mathrm{SO}} = \xi_{\mathrm{Cu}} \Bigg(& \sum_{m=-2}^{2} \frac{m}{2} \left(\hat{d}^\dagger_{m\uparrow} \hat{d}_{m\uparrow} - \hat{d}^\dagger_{m\downarrow} \hat{d}_{m\downarrow} \right) \\ & + \sqrt{\frac{3}{2}} \left(\hat{d}^\dagger_{0\downarrow} \hat{d}_{-1\uparrow} + \hat{d}^\dagger_{1\downarrow} \hat{d}_{0\uparrow} + \mathrm{h.c.} \right) \\ & + \left(\hat{d}^\dagger_{2\downarrow} \hat{d}_{1\uparrow} + \hat{d}^\dagger_{-1\downarrow} \hat{d}_{-2\uparrow} + \mathrm{h.c.} \right) \Bigg). \end{aligned} \tag{2.32}$$

The operator $\hat{d}^\dagger_{m\sigma}$ creates an electron with spin σ on the copper atom in the orbital with the set of quantum numbers $(l = 2, m)$. The parameter ξ_{Cu} can be found in the literature [33] and is set to $\xi_{\mathrm{Cu}} \approx 100$ meV. Like all other operators we project Eq (2.32) on the frontier orbital basis set $\{\mathrm{S}, \mathrm{H}, \mathrm{L}\pm\}$. By doing this we obtain

$$\begin{aligned} \hat{V}_{\mathrm{SO}} = & \lambda_1 \sum_{\tau=\pm} \tau \left(\hat{d}^\dagger_{\mathrm{L}\tau\uparrow} \hat{d}_{\mathrm{L}\tau\uparrow} - \hat{d}^\dagger_{\mathrm{L}\tau\downarrow} \hat{d}_{\mathrm{L}\tau\downarrow} \right) \\ & + \lambda_2 \left(\hat{d}^\dagger_{\mathrm{S}\uparrow} \hat{d}_{\mathrm{L}-\downarrow} + \hat{d}^\dagger_{\mathrm{L}+\uparrow} \hat{d}_{\mathrm{S}\downarrow} + \mathrm{h.c.} \right). \end{aligned} \tag{2.33}$$

We get effective SOI constants $\lambda_1 = \frac{1}{2}\xi_{\mathrm{Cu}} |\mathrm{c_L}|^2 = 0.47\mathrm{meV}$ and $\lambda_2 = \xi_{\mathrm{Cu}} \frac{\mathrm{c_S c_L}}{\sqrt{2}} = 6.16\mathrm{meV}$. Thereby all the pieces necessary to write Eq. (2.18) in the basis of our frontier orbitals

are there. It then reads in full glory

$$\begin{aligned}\hat{H}_{\mathrm{mol}} = &\sum_i (\varepsilon_i + \delta)\,\hat{n}_i + \sum_i U_i \hat{n}_{i\uparrow}\hat{n}_{i\downarrow} + \frac{1}{2}\sum_{[ij]} U_{ij}\hat{n}_i\hat{n}_j \\ &- \frac{1}{2}\sum_{[ij]}\sum_\sigma J_{ij}^{\mathrm{ex}}\left(\hat{n}_{i\sigma}\hat{n}_{j\sigma} - \hat{d}_{i\sigma}^\dagger \hat{d}_{j\bar{\sigma}}^\dagger \hat{d}_{i\bar{\sigma}}\hat{d}_{j\sigma}\right) \\ &+ \frac{1}{2}\sum_{[ij]}\sum_\sigma J_{ij}^P \hat{d}_{i\sigma}^\dagger \hat{d}_{i\bar{\sigma}}^\dagger \hat{d}_{j\bar{\sigma}}\hat{d}_{j\sigma} \\ &+ \frac{1}{2}\sum_{[ijk]}\sum_\sigma \left(\tilde{J}_{ijk}^P \hat{d}_{i\sigma}^\dagger \hat{d}_{\bar{\sigma}}^\dagger \hat{d}_{\bar{\sigma}}\hat{d}_{k\sigma} + \mathrm{h.c.}\right) \\ &+ \lambda_1 \sum_{\tau=\pm} \tau\left(\hat{d}_{\mathrm{L}\tau\uparrow}^\dagger \hat{d}_{\mathrm{L}\tau\uparrow} - \hat{d}_{\mathrm{L}\tau\downarrow}^\dagger \hat{d}_{\mathrm{L}\tau\downarrow}\right) \\ &+ \lambda_2\left(\hat{d}_{\mathrm{S}\uparrow}^\dagger \hat{d}_{\mathrm{L}-\downarrow} + \hat{d}_{\mathrm{L}+\uparrow}^\dagger \hat{d}_{\mathrm{S}\downarrow} + \mathrm{h.c.}\right).\end{aligned} \tag{2.34}$$

Through numerical diagonalization of $\hat{H}_{\mathrm{mol}}$ it is now possible to obtain many-body eigenenergies $\mathrm{E_{Nk}}$ and eigenstates $|\mathrm{N,k}\rangle$ which are categorized by the number of particles and the state index k. The Fock space spanned by $\hat{H}_{\mathrm{mol}}$ has a dimension of $4^4 = 256$ and thus the corresponding Liouville space a dimension of 256^2 which makes it difficult to deal with if one wants to keep coherences. Since in our transport calculations we will work at low energies only many-body eigenstates with low energies are assumed to play a role in transport. Thus, we will truncate the Fock space quite heavily as will be discussed in later sections. Now we will focus on the low energy spectrum of CuPc in the many-body basis.

2.3. Low energy spectrum of CuPc

The first thing to realize is that $\hat{H}_{\mathrm{mol}}$ as given in Eq. (2.34) possesses three different energy scales. They are sorted by $U > J > \lambda$. Here, U is a collection of all Hubbard like parameters (U_i, U_{ij}), J represents the exchange parameters $(J_{ij}^{\mathrm{ex}}, J_{ij}^P, \tilde{J}_{ijk}^P)$ and λ represents the SOI parameters (λ_1, λ_2). To clarify the effect these parameters have on the spectrum we will set $J, \lambda = 0$ in the beginning and determine the ground states for the neutral and anionic case. Then in two different steps we will analyse what happens if we let $J, \lambda \neq 0$.

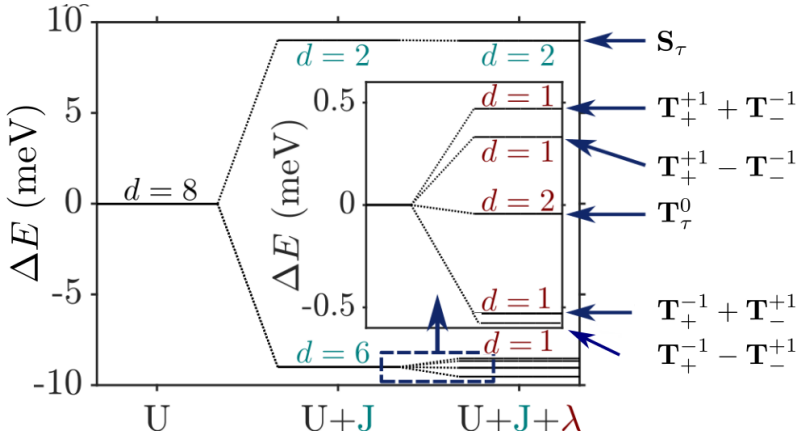

Figure 2.6.: The anionic low energy spectrum of CuPc with the number of degenerate states d. With only Hubbard like interaction (U) there is an eightfold degenerate ground state. The exchange interaction introduces a splitting between the two sets of singlets and triplets. SOI introduces further splitting in the triplet states yielding the spectrum on the right which is used in the numerical calculations. Adapted from Ref. [23].

2.3.1. Neutral low energy spectrum

First we define the state $|\Omega\rangle$ as

$$|\Omega\rangle := \hat{d}^\dagger_{\mathrm{H}\uparrow}\hat{d}^\dagger_{\mathrm{H}\downarrow}|0\rangle, \tag{2.35}$$

where $|0\rangle$ is the molecule with zero particles in the frontier orbitals. $|\Omega\rangle$ is therefore the state in which the HOMO is the only occupied orbital. The neutral ground states found by full numerical diagonalization are

$$|\mathrm{N}_0, \sigma\rangle = \hat{d}^\dagger_{\mathrm{S}\sigma}|\Omega\rangle, \tag{2.36}$$

which are two spin degenerate states and $\mathrm{N}_0 = 3$, like already concluded in Sec. 2.2.1. We will refer to them by

$$\begin{aligned} |D_0^\uparrow\rangle &= \hat{d}^\dagger_{\mathrm{S}\uparrow}|\Omega\rangle \\ |D_0^\downarrow\rangle &= \hat{d}^\dagger_{\mathrm{S}\downarrow}|\Omega\rangle. \end{aligned} \tag{2.37}$$

The reason for that configuration is like presented in Sec. 2.2.2 that $U_\mathrm{S} >> U_\mathrm{H}$. Therefore, these configurations are energetically the most favourable. One of the two possible configurations can be seen in Fig. 2.3. We denote the energy of those states as $\mathrm{E}^\mathrm{g}_{\mathrm{N}_0}$. These ground states are not affected by SOI. There are some exchange terms in $\hat{H}_\mathrm{mol}$ which create admixtures in these ground states, e.g. $\tilde{J}^P_{\mathrm{HL+L-}}$. However, these admixtures are very small and do not affect transitions between neutral and anionic states and can therefore be neglected here. We talk about them in a bit more detail in App. A.1.

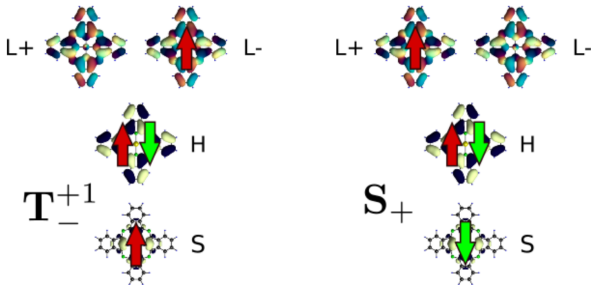

Figure 2.7.: Schematic depiction of the states $|\mathbf{T}_{-}^{+1}\rangle$ and $|\mathbf{S}_{+}\rangle$. The four frontier orbitals are shown and the arrows indicate occupation by an electron with spin up or down.

2.3.2. Anionic low energy spectrum

With $J, \lambda = 0$ the anionic ground state is eightfold degenerate and reads

$$|\mathrm{N}_0 + 1, \tau\sigma\sigma'\rangle = \hat{d}^{\dagger}_{\mathrm{S}\sigma}\hat{d}^{\dagger}_{\mathrm{L}\tau\sigma'}|\Omega\rangle. \tag{2.38}$$

Here $\tau = \pm$ denotes which LUMO is occupied and σ and σ' are the spin indices of the SOMO and LUMO respectively. The spectrum and its evolution with respect to the energy scales is depicted in Fig. 2.6. We label the energy in the same way as for the neutral ground state with $\mathrm{E}^{\mathrm{g}}_{\mathrm{N}_0+1}$. There are two possible spin values for the electron in the SOMO and the LUMO has 4 possible configurations (2 for the spin and 2 for the orbital part) since the LUMO+ and LUMO- are degenerate. This leads to the eightfold degeneracy of the ground state. To obtain also eigenstates of the operators $\hat{\mathbf{S}}^2$ and $\hat{S}_z$ we rewrite the ground states as

$$|\mathbf{S}_{\tau}\rangle = \frac{1}{\sqrt{2}}\left(\hat{d}^{\dagger}_{\mathrm{S}\uparrow}\hat{d}^{\dagger}_{\mathrm{L}\tau\downarrow} - \hat{d}^{\dagger}_{\mathrm{S}\downarrow}\hat{d}^{\dagger}_{\mathrm{L}\tau\uparrow}\right)|\Omega\rangle, \tag{2.39a}$$

$$|\mathbf{T}^{+1}_{\tau}\rangle = \hat{d}^{\dagger}_{\mathrm{S}\uparrow}\hat{d}^{\dagger}_{\mathrm{L}\tau\uparrow}|\Omega\rangle, \tag{2.39b}$$

$$|\mathbf{T}^{0}_{\tau}\rangle = \frac{1}{\sqrt{2}}\left(\hat{d}^{\dagger}_{\mathrm{S}\uparrow}\hat{d}^{\dagger}_{\mathrm{L}\tau\downarrow} + \hat{d}^{\dagger}_{\mathrm{S}\downarrow}\hat{d}^{\dagger}_{\mathrm{L}\tau\uparrow}\right)|\Omega\rangle, \tag{2.39c}$$

$$|\mathbf{T}^{-1}_{\tau}\rangle = \hat{d}^{\dagger}_{\mathrm{S}\downarrow}\hat{d}^{\dagger}_{\mathrm{L}\tau\downarrow}|\Omega\rangle. \tag{2.39d}$$

In this representation one can see that there are two sets of singlets, which have zero total spin, and two sets of triplets, with total spin equal to one. The two sets arise because there is orbital degeneracy in the LUMOs. Without exchange effects and SOI they are degenerate. Analogous to the neutral ground states the split pair hopping introduces small admixtures and a slight energy shift of all states. Since, the admixtures are small and the energy shift is the same for all states we neglect them here. The effects of the split pair hopping on the anionic states can be seen in App. A.1. A schematic depiction of the states $|\mathbf{T}_{-}^{+1}\rangle$ and $|\mathbf{S}_{+}\rangle$ can be seen in Fig. 2.7.

We explore now the effect of including exchange coupling in the analysis of the spectrum. Since, there are two unpaired spins in the ground state (one in the SOMO and LUMO) only one term of the exchange coupling part in Eq. (2.34) has an effect on the

spectrum, which is

$$-\sum_{\tau\sigma} J_{\mathrm{SL}}^{\mathrm{ex}} \left(\hat{n}_{\mathrm{S}\sigma} \hat{n}_{\mathrm{L}\tau\sigma} - \hat{d}_{\mathrm{S}\sigma}^{\dagger} \hat{d}_{\mathrm{L}\tau\sigma'}^{\dagger} \hat{d}_{\mathrm{S}\sigma'} \hat{d}_{\mathrm{L}\tau\sigma} \right). \tag{2.40}$$

This is the combination of the terms with $i = \mathrm{S}, j = \mathrm{L}$ and $i = \mathrm{L}, j = \mathrm{S}$. They can be written in one term by applying $J_{\mathrm{SL}}^{\mathrm{ex}} = J_{\mathrm{LS}}^{\mathrm{ex}}$ and using anticommutator relations for fermionic creation and annihilation operators. This term lifts the degeneracy between the singlets and the triplets. The energy of the singlets is raised while the triplets experience a downshift

$$\begin{aligned} \mathrm{E}_{\mathbf{S}} &= \mathrm{E}_{\mathrm{N}_0+1}^{\mathrm{g}} + J_{\mathrm{SL}}^{\mathrm{ex}}, \\ \mathrm{E}_{\mathbf{T}} &= \mathrm{E}_{\mathrm{N}_0+1}^{\mathrm{g}} - J_{\mathrm{SL}}^{\mathrm{ex}}. \end{aligned} \tag{2.41}$$

Finally, we will take a closer look at the influence of $\hat{V}_{\mathrm{SO}}$ on the anionic low energy spectrum. Since the SOI constants are much smaller than the Coulomb interaction terms one can treat the contribution of λ in the framework of perturbation theory. To analyse the effect of SOI on the states $|\mathbf{T}_{-}^{+1}\rangle$ and $|\mathbf{T}_{+}^{-1}\rangle$ we will separately take a look at the effect of the terms corresponding to λ_1 and λ_2 in Eq. (2.34). The λ_1-term is just a counting term and shifts the energy by

$$\Delta E_{\mathbf{T}_{-}^{+1}} = \Delta E_{\mathbf{T}_{+}^{-1}} = -\lambda_1. \tag{2.42}$$

If we apply the λ_2 term to $|\mathbf{T}_{+}^{-1}\rangle$ we get

$$|\tilde{a}\rangle = \lambda_2 \hat{d}_{\mathrm{L}+\downarrow}^{\dagger} \hat{d}_{\mathrm{L}+\uparrow}^{\dagger} |\Omega\rangle \tag{2.43}$$

and for $|\mathbf{T}_{-}^{+1}\rangle$

$$|\tilde{b}\rangle = \lambda_2 \hat{d}_{\mathrm{L}-\downarrow}^{\dagger} \hat{d}_{\mathrm{L}-\uparrow}^{\dagger} |\Omega\rangle. \tag{2.44}$$

The states $|\tilde{a}\rangle$ and $|\tilde{b}\rangle$ are not eigenstates of the full Hamiltonian but are coupled by the pair-hopping term

$$\frac{1}{2} J_{+-}^{P} \sum_{\sigma} \left(\hat{d}_{\mathrm{L}+\sigma}^{\dagger} \hat{d}_{\mathrm{L}+\sigma'}^{\dagger} \hat{d}_{\mathrm{L}-\sigma'} \hat{d}_{\mathrm{L}-\sigma} + \mathrm{h.c.} \right). \tag{2.45}$$

To obtain eigenstates of the full Hamiltonian we can form their linear combinations

$$\begin{aligned} |a\rangle &= \frac{1}{\sqrt{2}} \left(|\tilde{a}\rangle - |\tilde{b}\rangle \right), \\ |b\rangle &= \frac{1}{\sqrt{2}} \left(|\tilde{a}\rangle + |\tilde{b}\rangle \right). \end{aligned} \tag{2.46}$$

With this we conclude that also for $|\mathbf{T}_{-}^{+1}\rangle$ and $|\mathbf{T}_{+}^{-1}\rangle$ the formation of linear combinations is necessary to obtain the correct eigenstates

$$\begin{aligned} |\mathbf{T}_1\rangle &= \frac{1}{\sqrt{2}} \left(|\mathbf{T}_{+}^{-1}\rangle - |\mathbf{T}_{-}^{+1}\rangle \right), \\ |\mathbf{T}_2\rangle &= \frac{1}{\sqrt{2}} \left(|\mathbf{T}_{+}^{-1}\rangle + |\mathbf{T}_{-}^{+1}\rangle \right). \end{aligned} \tag{2.47}$$

The energy of $|\mathbf{T}_1\rangle$ and $|\mathbf{T}_2\rangle$ without λ_2 is

$$E_{\mathbf{T}_1} = E_{\mathbf{T}_2} = 2E_{\mathrm{H}} + E_{\mathrm{S}} + E_{\mathrm{L}} + 4\delta + U_{\mathrm{H}} - J_{\mathrm{SL}}^{\mathrm{ex}} - \lambda_1. \tag{2.48}$$

The energy of $|a\rangle$ is

$$E_a = 2E_{\mathrm{H}} + 2E_{\mathrm{L}} + 4\delta + U_{\mathrm{H}} + U_{\mathrm{L}} + 4U_{\mathrm{HL}} - J_{+-}^{P} \tag{2.49}$$

and the one of $|b\rangle$

$$E_b = E_a + 2J_{+-}^{P}. \tag{2.50}$$

To capture the effect of the λ_2-term we write an effective Hamiltonian in the basis $\{|\mathbf{T}_1\rangle, |a\rangle, |\mathbf{T}_2\rangle, |b\rangle\}$, with subtraction of a constant background

$$\Delta E = 2E_{\mathrm{H}} + E_{\mathrm{S}} + E_{\mathrm{L}} + 4\delta + U_{\mathrm{H}}, \tag{2.51}$$

it reads

$$H = \begin{pmatrix} H_{1a} & 0 \\ 0 & H_{2b} \end{pmatrix}, \tag{2.52}$$

with

$$H_{1a} = \begin{pmatrix} -J_{\mathrm{SL}}^{\mathrm{ex}} - \lambda_1 & \lambda_2 \\ \lambda_2 & E_a \end{pmatrix}, \tag{2.53}$$

and

$$H_{2b} = \begin{pmatrix} -J_{\mathrm{SL}}^{\mathrm{ex}} - \lambda_1 & \lambda_2 \\ \lambda_2 & E_b \end{pmatrix}. \tag{2.54}$$

Through diagonalization we obtain four states but we only look at the two interesting ones for the low energy spectrum, namely

$$\begin{aligned} |1\rangle &= \frac{1}{\sqrt{1-\gamma_a^2}} \left(|\mathbf{T}_1\rangle + \gamma_a |a\rangle\right), \\ |2\rangle &= \frac{1}{\sqrt{1-\gamma_b^2}} \left(|\mathbf{T}_2\rangle + \gamma_b |b\rangle\right), \end{aligned} \tag{2.55}$$

with $\gamma_{a/b} \approx \frac{-\lambda_2}{E_{a/b} + J_{\mathrm{SL}}^{\mathrm{ex}}}$. Their energies are

$$\begin{aligned} E_1 &\approx -\lambda_1 - \frac{\lambda_2^2}{E_a + J_{\mathrm{SL}}^{\mathrm{ex}} + \lambda_1} \\ E_2 &\approx -\lambda_1 - \frac{\lambda_2^2}{E_b + J_{\mathrm{SL}}^{\mathrm{ex}} + \lambda_1}. \end{aligned} \tag{2.56}$$

The admixtures are very small and thus we will neglect them in further parts of this thesis. They are however present in our numerical calculations. Nevertheless, with this analysis we can conclude that $\mathbf{T}_1$ and $\mathbf{T}_2$ are the lowest lying states of the anionic

molecule with an approximate energy splitting of

$$\Delta E_{\mathbf{T}_1\mathbf{T}_2} \approx \frac{2\lambda_2^2 J_{+-}^P}{E_a^2} \approx 20\ \mu\text{eV}, \tag{2.57}$$

which corresponds well to the values observed in the full numerical diagonalization. We write thus in the notation $|\mathrm{N}, \mathrm{k}\rangle$, introduced in the end of Sec. 2.2.3

$$|4,0\rangle = |\mathbf{T}_1\rangle = \frac{1}{\sqrt{2}}\left(|\mathbf{T}_+^{-1}\rangle - |\mathbf{T}_-^{+1}\rangle\right), \tag{2.58a}$$

$$|4,1\rangle = |\mathbf{T}_2\rangle = \frac{1}{\sqrt{2}}\left(|\mathbf{T}_+^{-1}\rangle + |\mathbf{T}_-^{+1}\rangle\right). \tag{2.58b}$$

In the full numerical calculations also other admixtures are present but they do not introduce a qualitative difference to this analysis and can therefore be ignored here. The state $|\mathbf{T}_+^0\rangle$ is coupled via λ_2 to

$$\hat{d}^\dagger_{\mathbf{L}+\downarrow}\hat{d}^\dagger_{\mathbf{L}-\downarrow}|\Omega\rangle, \tag{2.59}$$

whereas $|\mathbf{T}_-^0\rangle$ to

$$\hat{d}^\dagger_{\mathbf{L}+\uparrow}\hat{d}^\dagger_{\mathbf{L}-\uparrow}|\Omega\rangle. \tag{2.60}$$

Therefore, they stay degenerate also under the influence of $\hat{V}_{\mathrm{SO}}$ and experience a shift in energy [23]

$$\Delta E^0_{\mathbf{T}^0_+} = \Delta E^0_{\mathbf{T}^0_-} = -\frac{\lambda_1^2}{2J^{\mathrm{ex}}_{\mathrm{SL}}} - \frac{\lambda_2^2}{\Delta_1 - J^{\mathrm{ex}}_{\mathrm{SL}}}, \tag{2.61}$$

where Δ_1 is the energy corresponding to the states defined in eqs. (2.59) and (2.60). This energy shift is very small since its dependence on the SOI parameters is quadratic. We can now write the next excited states as

$$|4,2\rangle = |\mathbf{T}_+^0\rangle, \tag{2.62a}$$

$$|4,3\rangle = |\mathbf{T}_-^0\rangle, \tag{2.62b}$$

by neglecting very small admixtures.
The λ_1 term of $\hat{V}_{\mathrm{SO}}$ changes the energy of $|\mathbf{T}_+^{+1}\rangle$ and $|\mathbf{T}_-^{-1}\rangle$, with respect to $\mathrm{E}_{\mathbf{T}}$, by

$$\Delta E_{\mathbf{T}_+^{+1}} = \Delta E_{\mathbf{T}_-^{-1}} = \lambda_1. \tag{2.63}$$

To shorten the notation in the following we introduce two additional states

$$|\mathrm{L}+\uparrow, \mathrm{L}-\downarrow\rangle \equiv \hat{d}^\dagger_{\mathrm{L}+\uparrow}\hat{d}^\dagger_{\mathrm{L}-\downarrow}|\Omega\rangle, \tag{2.64}$$

$$|\mathrm{S}\uparrow, \mathrm{S}\downarrow\rangle \equiv \hat{d}^\dagger_{\mathrm{S}\uparrow}\hat{d}^\dagger_{\mathrm{S}|\downarrow}|\Omega\rangle. \tag{2.65}$$

The application of the λ_2 term on $|\mathbf{T}_+^{+1}\rangle$ yields

$$\lambda_2\left(\hat{d}^\dagger_{\mathrm{S}\uparrow}\hat{d}_{\mathrm{L}-\downarrow} + \hat{d}^\dagger_{\mathrm{L}+\uparrow}\hat{d}_{\mathrm{S}\downarrow} + \mathrm{h.c.}\right)|\mathbf{T}_+^{+1}\rangle = \lambda_2|\mathrm{S}\uparrow, \mathrm{S}\downarrow\rangle - \lambda_2|\mathrm{L}+\uparrow, \mathrm{L}-\downarrow\rangle \tag{2.66}$$

and on $|\mathbf{T}_{-}^{-1}\rangle$

$$\lambda_2 \left(\hat{d}^{\dagger}_{\mathrm{S}\uparrow}\hat{d}_{\mathrm{L}-\downarrow} + \hat{d}^{\dagger}_{\mathrm{L}+\uparrow}\hat{d}_{\mathrm{S}\downarrow} + \mathrm{h.c.}\right)|\mathbf{T}_{-}^{-1}\rangle = -\lambda_2|\mathrm{S}\uparrow,\mathrm{S}\downarrow\rangle + \lambda_2|\mathrm{L}+\uparrow,\mathrm{L}-\downarrow\rangle \tag{2.67}$$

We can conclude that the linear combination

$$|\alpha\rangle = \frac{1}{\sqrt{2}}\left(\mathbf{T}_{+}^{+1} + \mathbf{T}_{-}^{-1}\right) \tag{2.68}$$

is an eigenstate of $\hat{H}_{\mathrm{mol}}$. The last missing eigenstate is

$$|\beta\rangle = \frac{1}{\sqrt{2}}\left(\mathbf{T}_{+}^{+1} - \mathbf{T}_{-}^{-1}\right) + \frac{2\lambda_2}{\Delta_1 + J_{\mathrm{SL}}^{\mathrm{ex}}}|\mathrm{L}+\uparrow,\mathrm{L}-\downarrow\rangle - \frac{2\lambda_2}{\Delta_2 + J_{\mathrm{SL}}^{\mathrm{ex}}}\lambda_2|\mathrm{S}\uparrow,\mathrm{S}\downarrow\rangle, \tag{2.69}$$

with Δ_1 being the energy of $|\mathrm{L}+\uparrow,\mathrm{L}-\downarrow\rangle$ and Δ_2 the one of $|\mathrm{S}\uparrow,\mathrm{S}\downarrow\rangle$. The energy of $|\alpha\rangle$ is not influenced by λ_2 and thus the energy shift, once again with respect to $\mathrm{E}_{\mathbf{T}}$, is the one given in Eq. (2.63). The energy shift for $|\beta\rangle$ reads

$$\Delta E_\beta = \lambda_1 - 4\lambda_2\left(\frac{1}{\Delta_1 + J_{\mathrm{SL}}^{\mathrm{ex}}} + \frac{1}{\Delta_2 + J_{\mathrm{SL}}^{\mathrm{ex}}}\right). \tag{2.70}$$

Thus, we write

$$|4,4\rangle = |\beta\rangle = \frac{1}{\sqrt{2}}\left(\mathbf{T}_{+}^{+1} - \mathbf{T}_{-}^{-1}\right), \tag{2.71a}$$

$$|4,5\rangle = |\alpha\rangle = \frac{1}{\sqrt{2}}\left(\mathbf{T}_{+}^{+1} + \mathbf{T}_{-}^{-1}\right), \tag{2.71b}$$

where we have omitted the small admixtures to $|\beta\rangle$. Finally, the analysis of the Singlets, $|\mathbf{S}_{+}\rangle$ and $|\mathbf{S}_{-}\rangle$, is very similar to the one of $|\mathbf{T}_{+}^{0}\rangle$ and $|\mathbf{T}_{+}^{0}\rangle$. They stay degenerate and their energy is shifted, now with respect to $\mathrm{E}_{\mathbf{S}}$, by

$$\Delta E_{\mathbf{S}_+} = \Delta E_{\mathbf{S}_-} = \frac{\lambda_1^2}{2J_{\mathrm{SL}}^{\mathrm{ex}}} - \frac{\lambda_2^2}{\Delta_1 - J_{\mathrm{SL}}^{\mathrm{ex}}}. \tag{2.72}$$

To finalize the discussion of the anionic low energy spectrum we write

$$|4,6\rangle = |\mathbf{S}_{+}\rangle, \tag{2.73a}$$

$$|4,7\rangle = |\mathbf{S}_{-}\rangle. \tag{2.73b}$$

We can capture the effects of the SOI on the unperturbed triplet states by an effective Hamiltonian, in the basis $\{|\mathbf{T}_+^{+1}\rangle, |\mathbf{T}_+^{0}\rangle, |\mathbf{T}_+^{-1}\rangle, |\mathbf{T}_-^{+1}\rangle, |\mathbf{T}_-^{0}\rangle, |\mathbf{T}_-^{-1}\rangle, \}$,

$$\hat{H}^{\text{eff}} \equiv \alpha_5 \mathbb{1}_6 + \begin{pmatrix} \alpha_1/2 & 0 & 0 & 0 & 0 & \alpha_2 \\ 0 & \alpha_4 & 0 & 0 & 0 & 0 \\ 0 & 0 & -\alpha_1/2 & \alpha_3 & 0 & 0 \\ 0 & 0 & \alpha_3 & -\alpha_1/2 & 0 & 0 \\ 0 & 0 & 0 & 0 & \alpha_4 & 0 \\ \alpha_2 & 0 & 0 & 0 & 0 & \alpha_1/2 \end{pmatrix}. \tag{2.74}$$

The parameters α_1 - α_5 can be obtained from our numerical calculations and are $\alpha_1 = 0.860$ meV, $\alpha_2 = 2.26 \times 10^{-2}$ meV, $\alpha_3 = 1.66 \times 10^{-2}$ meV, $\alpha_4 = -1.01 \times 10^{-2}$ meV, and $\alpha_5 = -13.1$ eV. This Hamiltonian is able to reproduce the correct energy changes and correct linear combinations corresponding to the ones we got by our analysis of the anionic low energy spectrum.

2.4. Modelling of the leads and tunnelling processes

To describe transport through our system we need to clarify how we should treat the leads which are connected to the system and how we describe tunnelling. In this thesis we will model the leads as non-interacting Fermi seas which can be described by a Hamiltonian of the following form

$$\hat{H}_{\text{lead}} = \sum_{\mathbf{k}\sigma} \varepsilon_{\mathbf{k}\sigma} \hat{c}^\dagger_{\mathbf{k}\sigma} \hat{c}_{\mathbf{k}\sigma}, \tag{2.75}$$

with $\varepsilon_{\mathbf{k}\sigma}$ being the energy of an electron with momentum $\mathbf{k}$ and spin σ, $\hat{c}^\dagger_{\mathbf{k}\sigma}$ creates an electron in the lead. Since, they are considered to be large reservoirs we describe their density matrix as

$$\hat{\rho} = \frac{\mathrm{e}^{-\beta\left(\hat{H}_{\text{lead}} - \mu\hat{N}\right)}}{Z}, \tag{2.76}$$

where $\beta = \frac{1}{\mathrm{k_B T}}$, $\hat{N}$ is the particle number operator and Z the canonical partition function.
To describe the tunnelling between our system and the leads we use a Hamiltonian according to Bardeen's tunnelling theory which reads [34]

$$\hat{H}_{\text{tun}} = \sum_{\substack{\eta i \\ \sigma \mathbf{k}}} t^\eta_{i\mathbf{k}} \hat{c}^\dagger_{\eta\mathbf{k}\sigma} \hat{d}_{i\sigma} + \text{h.c.}. \tag{2.77}$$

In Eq. (2.77) η denotes the different leads, $\hat{c}^\dagger_{\eta\mathbf{k}\sigma}$ is the creation operator for the lead η, whereas $\hat{d}^\dagger_{i\sigma}$ creates an electron on the system in the orbital i with spin σ. The last part are the $t^\eta_{i\mathbf{k}}$ which are the tunnelling matrix elements between lead η and

the system. They are calculated as the overlap between the states in the lead $|\eta\mathbf{k}\sigma\rangle$ and the molecular orbitals $|i\sigma\rangle$ renormalized by the single particle eigenenergies of the molecule [35]

$$t^{\eta}_{i\mathbf{k}} = \varepsilon_{i\sigma} \langle \eta\mathbf{k}\sigma | i\sigma \rangle \,. \tag{2.78}$$

3. A Transport Formalism For The THz-STM

In this chapter we will derive a transport formalism for the THz-STM. Firstly, we will deduce a general transport formalism without taking the special geometry of the STM into account. Then we will make a short excursion into the general functioning of an STM and how to describe it within our transport formalism. In the end we will explore what effects the THz laser pulses will have on the treatment of the transport problem.

3.1. Transport within the density matrix formalism

In this section we will derive a general transport formalism in the density matrix framework. We will follow refs. [36, 37] for this purpose.

3.1.1. Liouville equation for the reduced density matrix

The density operator can describe a mixture of states $|\psi_n\rangle$ ($n \in \mathbb{N}$) with statistical weights W_n. The most general form is

$$\hat{\rho} = \sum_n W_n |\psi_n\rangle\langle\psi_n|. \tag{3.1}$$

To obtain a matrix representation of this operator we choose an orthonormal basis set, $\{|\Phi_m\rangle\}$. The states $|\psi_n\rangle$ can then be expressed in terms of this basis set as

$$|\psi_n\rangle = \sum_m a_{nm} |\Phi_m\rangle. \tag{3.2}$$

By plugging Eq. (3.2) into Eq. (3.1) we obtain

$$\hat{\rho} = \sum_{nmm'} W_n a_{nm} a^*_{nm'} |\Phi_m\rangle\langle\Phi_{m'}|. \tag{3.3}$$

This is the matrix representation of the density operator in the basis of the Hilbert space. We will now start to develop a transport formalism for it. The necessary building blocks

of an Hamiltonian able to describe transport through a system are

$$\hat{H} = \hat{H}_{\text{mol}} + \hat{H}_{\text{leads}} + \hat{H}_{\text{tun}}, \tag{3.4}$$

namely the central system part $\hat{H}_{\text{mol}}$, which in our case is a molecule, the leads $\hat{H}_{\text{leads}}$ and the tunnelling Hamiltonian $\hat{H}_{\text{tun}}$. They will have the form introduced in the previous chapter. Let us for now assume that the Hamiltonian $\hat{H}$ in Eq. (3.4) is time independent. Then we can write the time evolution operator as

$$\hat{U}(t) = \mathrm{e}^{-\frac{\mathrm{i}}{\hbar}\hat{H}(t)}. \tag{3.5}$$

This operator transforms a state $|\psi(0)\rangle$ into a state $|\psi(t)\rangle$

$$|\psi(t)\rangle = \hat{U}(t)|\psi(0)\rangle. \tag{3.6}$$

The time evolution of the density operator is given by

$$\hat{\rho}(t) = \hat{U}(t)\hat{\rho}_0\hat{U}^\dagger(t). \tag{3.7}$$

Here, $\hat{\rho}_0$ denotes the density matrix at time $t = 0$, i.e. $\hat{\rho}_0 = \hat{\rho}(t = 0)$. Differentiation of Eq. (3.7) with respect to time yields

$$\begin{aligned} \frac{\mathrm{d}\rho(t)}{\mathrm{d}t} &= -\frac{\mathrm{i}}{\hbar}\hat{H}\hat{\rho}(t) + \frac{\mathrm{i}}{\hbar}\hat{\rho}(t)\hat{H} \\ &= -\frac{\mathrm{i}}{\hbar}\left[\hat{H}, \hat{\rho}(t)\right]. \end{aligned} \tag{3.8}$$

This equation is called the Liouville-von Neumann equation, which we will call in short Liouville equation. It is the most fundamental equation in density matrix theory. We assume the tunneling part in Eq. (3.4) to be a small perturbation to our full system, i.e. the coupling between the system and the leads is weak (weak coupling limit), and rewrite the Hamiltonian as

$$\hat{H} = \hat{H}_0 + \hat{H}_{\text{tun}}. \tag{3.9}$$

We define $\hat{U}_0(t) \coloneqq \mathrm{e}^{-\frac{\mathrm{i}}{\hbar}\hat{H}_0 t}$ to transfer the density matrix into the interaction picture

$$\hat{\rho}^I(t) = \hat{U}_0^\dagger\hat{\rho}(t)\hat{U}_0. \tag{3.10}$$

By using eqs. (3.8) and (3.10) we deduce the Liouville equation in the interaction picture

$$\begin{aligned} \dot{\hat{\rho}}^I(t) = \frac{\mathrm{d}}{\mathrm{d}t}\hat{U}_0^\dagger(t)\hat{\rho}(t)\hat{U}_0(t) = \\ &+ \frac{\mathrm{i}}{\hbar}\hat{U}_0^\dagger(t)\hat{H}_0\hat{\rho}(t)\hat{U}_0(t) - \frac{\mathrm{i}}{\hbar}\hat{U}_0^\dagger(t)\hat{H}\hat{\rho}(t)\hat{U}_0(t) \\ &+ \frac{\mathrm{i}}{\hbar}\hat{U}_0^\dagger(t)\hat{\rho}(t)\hat{H}\hat{U}_0(t) - \frac{\mathrm{i}}{\hbar}\hat{U}_0^\dagger(t)\hat{\rho}(t)\hat{H}_0\hat{U}_0(t) \\ &= -\frac{\mathrm{i}}{\hbar}\left[\hat{H}^I_{\text{tun}}(t), \hat{\rho}^I(t)\right], \end{aligned} \tag{3.11}$$

with

$$\hat{H}^I_{\text{tun}}(t) = \hat{U}_0^\dagger(t)\hat{H}_{\text{tun}}\hat{U}_0(t) = \sum_{\substack{\eta i \\ \sigma \mathbf{k}}} \left(t^\eta_{i\mathbf{k}\sigma} \hat{c}^\dagger_{\eta\mathbf{k}\sigma}\, \mathrm{e}^{\frac{\mathrm{i}}{\hbar}\varepsilon_{\eta\mathbf{k}}t}\, \hat{d}^I_{i\sigma}(t) + \text{h.c.} \right). \tag{3.12}$$

The time evolution of the density operator in the interaction picture only depends on $\hat{H}^I_{\text{tun}}$. Since we assume the tunnelling Hamiltonian to be a small perturbation to our system we are able to solve Eq. (3.11) in the framework of time dependent perturbation theory. The formal solution of the Liouville equation (3.11) is

$$\hat{\rho}^I(t) = \hat{\rho}^I(t_0) - \frac{\mathrm{i}}{\hbar}\int_{t_0}^{t} \mathrm{d}t' \left[\hat{H}^I_{\text{tun}}(t), \hat{\rho}^I(t')\right]. \tag{3.13}$$

By substituting the formal solution Eq. (3.13) back into the Liouville equation we obtain

$$\dot{\hat{\rho}}^I(t) = -\frac{\mathrm{i}}{\hbar}\left[\hat{H}^I_{tun}(t), \hat{\rho}^I(t_0)\right] - \frac{1}{\hbar^2}\int_{t_0}^{t} \mathrm{d}t' \left[\hat{H}^I_{tun}(t), \left[\hat{H}^I_{tun}(t'), \hat{\rho}^I(t')\right]\right]. \tag{3.14}$$

We now rename the variables in Eq. (3.13) so that it reads

$$\hat{\rho}^I(t') = \hat{\rho}^I(t) - \frac{\mathrm{i}}{\hbar}\int_{t}^{t'} \mathrm{d}t'' \left[\hat{H}^I_{\text{tun}}(t''), \hat{\rho}^I(t'')\right] \tag{3.15}$$

and reinsert it once again into Eq. (3.14) to obtain

$$\begin{aligned} \dot{\hat{\rho}}^I(t) = &-\frac{\mathrm{i}}{\hbar}\left[\hat{H}^I_{tun}(t), \hat{\rho}^I(t_0)\right] - \frac{1}{\hbar^2}\int_{t_0}^{t} \mathrm{d}t' \left[\hat{H}^I_{tun}(t), \left[\hat{H}^I_{tun}(t'), \hat{\rho}^I(t)\right]\right] \\ &+ \frac{\mathrm{i}}{\hbar^3}\int_{t_0}^{t} \mathrm{d}t' \int_{t}^{t'} \mathrm{d}t'' \left[\hat{H}^I_{\text{tun}}(t), \left[\hat{H}^I_{\text{tun}}(t'), \left[\hat{H}^I_{\text{tun}}(t''), \hat{\rho}^I(t'')\right]\right]\right]. \end{aligned} \tag{3.16}$$

3.1.2. Time local Master Equation

Up to this point everything in our analytical treatment was exact but now we will start to make some approximations. We will restrict ourself to sequential tunnelling in this thesis, i.e. we will treat the dynamics in second order perturbation theory with respect to $\hat{H}_{\text{tun}}$. Therefore, we drop the last term in Eq. (3.16). Due to this we obtain an equation which is time local, i.e. the evolution of $\hat{\rho}$ at time t only depends on its value at time t and not on its past. Equation (3.16) describes the dynamics of the whole system. We are, however, interested in the central system and not the leads. Therefore, we introduce the reduced density matrix,

$$\hat{\rho}^I_\odot = \mathrm{Tr}_{\text{leads}}\left\{\hat{\rho}^I(t)\right\}, \tag{3.17}$$

which we get by tracing out the lead degrees of freedom. Furthermore, this helps in making the calculations more feasible. If we apply the trace over the leads to Eq. (3.16)

and drop the 3rd therm we obtain

$$\dot{\hat{\rho}}^I_\odot = -\frac{1}{\hbar^2}\int_{t_0}^{t} \mathrm{d}t'\, \mathrm{Tr}_{\mathrm{leads}}\left\{\left[\hat{H}^I_{\mathrm{tun}}(t),\left[\hat{H}^I_{\mathrm{tun}}(t'),\hat{\rho}^I(t)\right]\right]\right\}. \tag{3.18}$$

The first term is vanishing since $\hat{H}^I_{\mathrm{tun}}(t)$ does not conserve particle number in the leads, whereas the trace is particle conserving. At $t_0 = 0$ the leads and the system are uncorrelated, this allows us to factorize the total density matrix in a system and a leads part

$$\hat{\rho}^I(t_0) = \hat{\rho}_\odot(t_0)\hat{\rho}_{\mathrm{leads}}(t_0). \tag{3.19}$$

However, we can always write the density matrix as

$$\hat{\rho}^I(t) = \hat{\rho}^I_\odot(t)\hat{\rho}^I_{\mathrm{leads}}(t) + \Delta\hat{\rho}^I, \tag{3.20}$$

where $\Delta\hat{\rho}^I$ is of the order of $\hat{H}_{\mathrm{tun}}$, see page 277 of Ref. [36]. Thus, we neglect it in our second order treatment and factorize the density matrix at all times

$$\hat{\rho}^I(t) = \hat{\rho}^I_\odot(t)\hat{\rho}^I_{\mathrm{leads}}, \tag{3.21}$$

where we have dropped the time dependence in the density matrix of the leads because they are large reservoirs and thus have so many degrees of freedom that the interaction with the central system is negligible. The density matrix used to describe them was introduced in Eq. (2.76). By expanding the commutator in Eq. (3.18) we obtain

$$\begin{aligned}
\dot{\hat{\rho}}^I_\odot(t) = -\frac{1}{\hbar^2}\sum_{\eta\mathbf{k}}\sum_{\substack{i\sigma\\ j\sigma'}}\int_{t_0}^{t}\mathrm{d}t'\Big[& \\
& t^{\eta}_{i\mathbf{k}}t^{\eta *}_{j\mathbf{k}}\hat{d}^I_{i\sigma}(t)\hat{d}^{\dagger I}_{j\sigma'}(t')\hat{\rho}^I_\odot(t')\,\mathrm{e}^{\frac{\mathrm{i}}{\hbar}\varepsilon_{\eta\mathbf{k}}(t-t')}\,f^+_\eta(\varepsilon_{\mathbf{k}}) \\
& + t^{\eta *}_{i\mathbf{k}}t^{\eta}_{j\mathbf{k}}\hat{d}^{\dagger I}_{i\sigma}(t)\hat{d}^I_{j\sigma'}(t')\hat{\rho}^I_\odot(t')\,\mathrm{e}^{-\frac{\mathrm{i}}{\hbar}\varepsilon_{\eta\mathbf{k}}(t-t')}\,f^-_\eta(\varepsilon_{\mathbf{k}}) \\
& - t^{\eta}_{i\mathbf{k}}t^{\eta *}_{j\mathbf{k}}\hat{d}^I_{i\sigma}(t)\hat{\rho}^I_\odot(t')\hat{d}^{\dagger I}_{j\sigma'}(t')\,\mathrm{e}^{\frac{\mathrm{i}}{\hbar}\varepsilon_{\eta\mathbf{k}}(t-t')}\,f^-_\eta(\varepsilon_{\mathbf{k}}) \\
& + t^{\eta *}_{i\mathbf{k}}t^{\eta}_{j\mathbf{k}}\hat{d}^{\dagger I}_{i\sigma}(t)\hat{\rho}^I_\odot(t')\hat{d}^I_{j\sigma'}(t')\,\mathrm{e}^{-\frac{\mathrm{i}}{\hbar}\varepsilon_{\eta\mathbf{k}}(t-t')}\,f^+_\eta(\varepsilon_{\mathbf{k}}) \\
& + \mathrm{h.c.}\Big],
\end{aligned} \tag{3.22}$$

with $f^+_\eta(\varepsilon_{\mathbf{k}}) = \mathrm{Tr}_{\mathrm{leads}}\left\{\hat{c}^\dagger_{\eta\mathbf{k}\sigma}\hat{c}_{\eta\mathbf{k}'\sigma'}\hat{\rho}_{\mathrm{leads}}\right\}$ being the Fermi distribution in the lead η which has a chemical potential of μ_η and $f^-_\eta(\varepsilon_{\mathbf{k}}) = 1 - f^+_\eta(\varepsilon_{\mathbf{k}})$. We use

$$\hat{\rho}^I_\odot(t) = \mathrm{e}^{\frac{\mathrm{i}}{\hbar}\hat{H}_{\mathrm{mol}}t}\,\hat{\rho}_\odot(t)\,\mathrm{e}^{-\frac{\mathrm{i}}{\hbar}\hat{H}_{\mathrm{mol}}t} \tag{3.23}$$

to transform Eq. (3.22) back into the Schrödinger picture. Furthermore, we substitute $t'' = t - t'$ in the integral and let t_0 go to $-\infty$. This is, in this way of deriving the time local master equation, a part of our model but can also be derived in the Markov approximation, see for example refs. [36–38]. With all this we obtain the reduced density

matrix in the Schrödinger picture

$$\begin{aligned}\dot{\hat{\rho}}_{\odot}(t) = &-\frac{\mathrm{i}}{\hbar}\left[\hat{H}_{\mathrm{mol}},\hat{\rho}_{\odot}(t)\right] - \frac{1}{\hbar^2}\int_0^{\infty}\mathrm{d}t'\sum_{\eta\mathbf{k}}\sum_{\substack{i\sigma\\ j\sigma'}}\Big[\\ &t^{\eta}_{i\mathbf{k}}t^{\eta *}_{j\mathbf{k}}\hat{d}_{i\sigma}\hat{d}^{\dagger I}_{j\sigma'}(-t')\hat{\rho}_{\odot}(t)\,\mathrm{e}^{\frac{\mathrm{i}}{\hbar}\varepsilon_{\eta\mathbf{k}\sigma}t'}\,f^{+}_{\eta}(\varepsilon_{\mathbf{k}\sigma})\\ &+t^{\eta *}_{i\mathbf{k}}t^{\eta}_{j\mathbf{k}}\hat{d}^{\dagger}_{i\sigma}\hat{d}^{I}_{j\sigma'}(-t')\hat{\rho}_{\odot}(t)\,\mathrm{e}^{-\frac{\mathrm{i}}{\hbar}\varepsilon_{\eta\mathbf{k}\sigma}t'}\,f^{-}_{\eta}(\varepsilon_{\mathbf{k}\sigma})\\ &-t^{\eta}_{i\mathbf{k}}t^{\eta *}_{j\mathbf{k}}\hat{d}_{i\sigma}\hat{\rho}_{\odot}(t)\hat{d}^{\dagger I}_{j\sigma'}(-t')\,\mathrm{e}^{\frac{\mathrm{i}}{\hbar}\varepsilon_{\eta\mathbf{k}\sigma}t'}\,f^{-}_{\eta}(\varepsilon_{\mathbf{k}\sigma})\\ &-t^{\eta *}_{i\mathbf{k}}t^{\eta}_{j\mathbf{k}}\hat{d}^{\dagger}_{i\sigma}\hat{\rho}_{\odot}(t)\hat{d}^{I}_{j\sigma'}(-t')\,\mathrm{e}^{-\frac{\mathrm{i}}{\hbar}\varepsilon_{\eta\mathbf{k}\sigma}t'}\,f^{+}_{\eta}(\varepsilon_{\mathbf{k}\sigma})\\ &+\mathrm{h.c.}\Big],\end{aligned} \tag{3.24}$$

where we have renamed t'' to t'. As an example we will now focus on the second line in Eq. (3.24) to see how to proceed in the calculation. We can write for the time dependent creation operator

$$\begin{aligned}&\hat{d}^{\dagger I}_{j\sigma'}(-t) = \mathrm{e}^{-\frac{\mathrm{i}}{\hbar}\hat{H}_{\mathrm{mol}}t}\,\hat{d}^{\dagger}_{j\sigma'}\,\mathrm{e}^{\frac{\mathrm{i}}{\hbar}\hat{H}_{\mathrm{mol}}t} =\\ &\sum_{\substack{N\\ EE'}}\sum_{\substack{i\sigma\\ l\sigma''}}\mathrm{e}^{-\frac{\mathrm{i}}{\hbar}(E_N-E'_{N+1})t}\langle N+1Ei\sigma|\hat{d}^{\dagger}_{j\sigma'}|NE'l\sigma''\rangle\;|N+1Ei\sigma\rangle\langle NE'l\sigma''|.\end{aligned} \tag{3.25}$$

We then need to solve integrals of the form

$$\begin{aligned}&\sum_{\eta\mathbf{k}}\int_0^{\infty}\mathrm{d}t' t^{\eta}_{i\mathbf{k}}t^{\eta *}_{j\mathbf{k}}\,\mathrm{e}^{-\frac{\mathrm{i}}{\hbar}(E_N-E'_{N-1}-\varepsilon_{\eta\mathbf{k}\sigma})t'}\,f^{+}_{\eta}(\varepsilon_{\mathbf{k}\sigma})\\ &=\lim_{\lambda\to 0^+}\sum_{\eta\mathbf{k}}-\mathrm{i}\hbar t^{\eta}_{i\mathbf{k}}t^{\eta *}_{j\mathbf{k}}\frac{f^{+}_{\eta}(\varepsilon_{\mathbf{k}\sigma})}{(\underbrace{E_N-E'_{N+1}}_{=\Delta E}-\varepsilon_{\eta\mathbf{k}\sigma})-i\lambda}\\ &=\lim_{\lambda\to 0^+}\sum_{\eta\mathbf{k}}\int\mathrm{d}\varepsilon-\mathrm{i}\hbar\delta(\varepsilon-\varepsilon_{\mathbf{k}\sigma})t^{\eta}_{i\mathbf{k}}t^{\eta *}_{j\mathbf{k}}\frac{f^{+}_{\eta}(\varepsilon)}{\Delta E-\varepsilon-\mathrm{i}\lambda}\end{aligned} \tag{3.26}$$

We identify the tunnelling rate matrices

$$\Gamma^{\eta}_{\sigma i,\sigma j} = \frac{2\pi}{\hbar}\sum_{k}t^{\eta}_{i\mathbf{k}}t^{\eta *}_{j\mathbf{k}}\delta(\varepsilon-\varepsilon_{\mathbf{k}\sigma}), \tag{3.27}$$

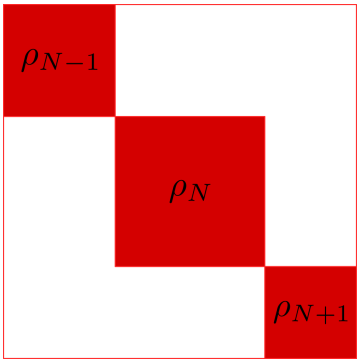

Figure 3.1.: The block diagonal form of the density matrix with respect to three different particle numbers. The white space is zero whereas the red spaces contain elements different from zero.

which vary slowly with respect to the energy integration. We can now rewrite Eq. (3.26) as

$$\begin{aligned}
&-\sum_\eta \frac{\hbar^2\Gamma^\eta_{\sigma i,\sigma j}}{2}\lim_{\lambda\to 0^+}\frac{\mathrm{i}}{\pi}\int \mathrm{d}\varepsilon f^+_\eta(\varepsilon)\frac{\Delta E-\varepsilon+\mathrm{i}\lambda}{(\Delta E-\varepsilon)^2+\lambda^2} = \\
&-\sum_\eta \frac{\hbar^2\Gamma^\eta_{\sigma i,\sigma j}}{2}\lim_{\lambda\to 0^+}\left(\int \mathrm{d}\varepsilon\Big(\underbrace{\frac{-\lambda f^+_\eta(\varepsilon)}{\pi[(\Delta E-\varepsilon)^2+\lambda^2]}}_{\delta_\lambda(\Delta E-\varepsilon)f^+_\eta(\varepsilon)}+\frac{\mathrm{i}(\Delta E-\varepsilon)^2}{[(\Delta E-\varepsilon)^2+\lambda^2]}\frac{f^+_\eta(\varepsilon)}{\pi(\Delta E-\varepsilon)}\Big)\right) = \\
&\sum_\eta \frac{\hbar^2\Gamma^\eta_{\sigma i,\sigma j}}{2}\left(f^+_\eta(\Delta E)-\frac{\mathrm{i}}{\pi}\mathcal{P}\int \mathrm{d}\varepsilon\frac{f^+_\eta(\varepsilon)}{\Delta E-\varepsilon}\right),
\end{aligned} \tag{3.28}$$

where $\mathcal{P}\int$ denotes Cauchy's principal value integration. The result of this integral is

$$\mathcal{P}\int \mathrm{d}\varepsilon\frac{f^+_\eta(\varepsilon)}{\Delta E-\varepsilon} = \Re\Psi^{(0)}(\frac{1}{2}+\frac{\mathrm{i}\beta}{2\pi}(\Delta E-\mu_\eta)), \tag{3.29}$$

the real part of the Digamma function, see Ref. [39]. We will denote this from now on as $\mathrm{p}_\eta(x) = \Re\psi^{(0)}(\frac{1}{2}+\frac{\mathrm{i}}{2\pi}(x-\mu_\eta))$. The density matrix is block diagonal with respect to the number of particles, N, on the central system, as illustrated in Fig. 3.1. Therefore, we introduce the projector

$$P_{NE} \coloneqq \sum_{i\sigma} |NEi\sigma\rangle\langle\sigma iEN|, \tag{3.30}$$

which projects $\hat{\rho}_\odot$ on the subspace with N particles and energy E. The sum over the indices i and σ distinguishes between degenerate states. In the following we use the notation

$$\rho^N_{EE'} = P_{NE}\hat{\rho}_\odot P_{NE'}. \tag{3.31}$$

Collecting the results obtained in the previous paragraph enables us to solve the time integral in Eq. (3.24) which then becomes

$$
\begin{aligned}
\dot{\rho}^N_{EE'} = &-\frac{\mathrm{i}}{\hbar}(E-E')\rho^N_{EE'} \\
&-\sum_{\eta F}\sum_{\substack{i\sigma\\ j\sigma'}}\frac{\Gamma^\eta_{\sigma i,\sigma j}}{2}P_{NE}\Bigg\{\hat{d}^\dagger_{i\sigma}\left[-\frac{\mathrm{i}}{\pi}\mathrm{p}_\eta(F-\hat{H}_{\mathrm{mol}})+f^-_\eta(F-\hat{H}_{\mathrm{mol}})\right]\hat{d}_{j\sigma'} \\
&+\hat{d}_{j\sigma'}\left[-\frac{\mathrm{i}}{\pi}\mathrm{p}_\eta(\hat{H}_{\mathrm{mol}}-F)+f^+_\eta(\hat{H}_{\mathrm{mol}}-F)\right]\hat{d}^\dagger_{i\sigma}\Bigg\}\rho^N_{FE'} \\
&-\sum_{\eta F}\sum_{\substack{i\sigma\\ j\sigma'}}\frac{\Gamma^\eta_{\sigma i,\sigma j}}{2}\rho^N_{EF}\Bigg\{\hat{d}^\dagger_{i\sigma}\left[+\frac{\mathrm{i}}{\pi}\mathrm{p}_\eta(F-\hat{H}_{\mathrm{mol}})+f^-_\eta(F-\hat{H}_{\mathrm{mol}})\right]\hat{d}_{j\sigma'} \\
&+\hat{d}_{j\sigma'}\left[\frac{\mathrm{i}}{\pi}\mathrm{p}_\eta(\hat{H}_{\mathrm{mol}}-F)+f^+_\eta(\hat{H}_{\mathrm{mol}}-F)\right]\hat{d}^\dagger_{i\sigma}\Bigg\}P_{NE'} \\
&+\sum_{\eta FF'}\sum_{\substack{i\sigma\\ j\sigma'}}\frac{\Gamma^\eta_{\sigma i,\sigma j}}{2}P_{NE}\Bigg\{\hat{d}^\dagger_{i\sigma}\rho^{N-1}_{FF'}\hat{d}_{j\sigma'}\left[\frac{\mathrm{i}}{\pi}\mathrm{p}_\eta(E'-F')+f^+_\eta(E'-F')\right]+\mathrm{h.c.} \\
&+\hat{d}_{j\sigma'}\rho^{N+1}_{FF'}\hat{d}^\dagger_{i\sigma}\left[\frac{\mathrm{i}}{\pi}\mathrm{p}_\eta(F'-E')+f^-_\eta(F'-E')\right]+\mathrm{h.c.}\Bigg\}P_{NE'}.
\end{aligned}
\tag{3.32}
$$

3.1.3. Interference blocking due to degenerate states

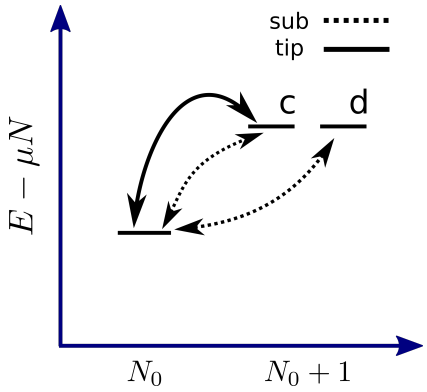

Figure 3.2.: Conceptional depiction of the blocking states. The coupled state (c) is connected to the N_0 state via the tip and the substrate. The decoupled state (d) though is only coupled via the substrate. The y-axis shows the grandcannonical energy of the states.

In this section we will take a short detour from the development of the transport formalism to introduce the concept of a blocking state. The first prerequisite for a blocking state to occur is a N particle non-degenerate state and a two degenerate $N+1$ particle state. The condition of degeneracy can be softened a bit in the sense that the energy splitting between the two states is smaller than the tunnelling rates. The second condition regards the transition amplitudes between the system and the leads. The ratio of these transition amplitudes at the source (substrate) and the drain (tip) must not be equal

$$\frac{\gamma_{1\text{sub}}}{\gamma_{2\text{sub}}} \neq \frac{\gamma_{1\text{tip}}}{\gamma_{2\text{tip}}}, \tag{3.33}$$

where the subscript 1 denotes a transition $N_0 \rightarrow N_0 + 1$ and 2 vice versa. Due to Eq. (3.33) there exists a linear combination of the $N_0 + 1$ particle states which is coupled to one of the leads but not the other. [40] In STMs the condition (3.33) is met since the tip and substrate have quite different transition amplitudes as we will see in the following chapters. It can be shown that the blocking state in an STM set-up is decoupled from the tip [41]. A state which is decoupled from the tip acts as a blocking state for current flowing from the substrate to the tip, since it can be populated via a substrate $\rightarrow$ molecule transition but not depopulated via the tip. This effect can be for example seen as negative differential conductance in single electron transistors. [40]

3.2. Scanning Tunnelling Microscopy

The scanning tunnelling microscope (STM) was invented at the IBM laboratories in Zürich by Gerd Binnig and Heinrich Rohrer in 1982 [11]. They were awarded a Nobel prize for the development in 1986. The fundamental physical mechanism behind the STM is quantum tunnelling. The system one wants to investigate is deposited on a substrate. The system can be for example a surface or an individual molecule. A metallic tip is positioned over the system with a distance of a few Å. If a bias is applied between the tip and the substrate tunnelling processes can occur between the substrate and the system and also between the system and the tip, thus, leading to a tunnel current. The tunnelling probability is dependent on the overlap of the corresponding wave functions and thus it is highly dependent on the distance of the tip and the substrate. In the original paper [11] Binnig and Rohrer used the so called “constant-

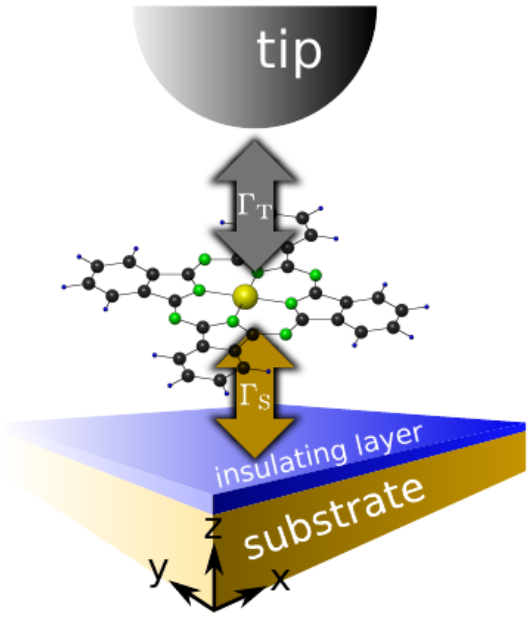

Figure 3.3.: Schematic picture of an STM single molecule junction. We see the insulating layer above the copper substrate which the molecules couples to with the rate Γ_{sub}. The tip couples with the rate Γ_{tip}. Taken from Ref. [23].

current" mode to obtain a surface topography of an Au (110) surface. In this method one moves the tip in all three spatial dimensions over the surface while keeping the current voltage at a constant value. Since the current is dependent on the distance of substrate and tip one can measure a surface topography by keeping the current constant and measuring the necessary movements of the tip in the z-dimension. The STM is dependent on a nonzero conductance in its tunnelling junction. Therefore, for almost 20 years STM studies of single molecules where limited to deposit the molecules directly on metals and semiconductors. In this case tough the electronic structure of the molecule is disturbed due to electronic coupling between the molecule and the substrate [42]. This problem can be solved by depositing a molecule on a thin insulating layer. Repp et al. [43] were able to obtain electronic images of unperturbed Pentacene orbitals by evaporating two mono-layers of NaCl onto Cu(111) and then adsorbing individual molecules onto the substrate. We will show in the following section how to describe transport across an STM junction, which can be seen in Fig. 3.3, on an insulating layer within the formalism presented in the previous section.

3.2.1. The Hamiltonian of an STM junction

The complete Hamiltonian to describe transport in an STM setup is

$$\hat{H} = \hat{H}_{\text{mol}} + \hat{H}_{\text{ic}} + \hat{H}_{\text{sub}} + \hat{H}_{\text{tip}} + \hat{H}_{\text{tun}}, \tag{3.34}$$

with $\hat{H}_{\text{mol}}$ describing the central system as introduced in Eq. (3.4), $\hat{H}_{\text{sub}}$ and $\hat{H}_{\text{tip}}$ describing the substrate and tip. They are corresponding to the leads in an STM setup and are described by Eq. (2.75). $\hat{H}_{\text{tun}}$ describes the tunnelling between the molecule and the tip/substrate. The additional term with respect to Eq. (3.4), $\hat{H}_{\text{ic}}$, describes image charge effects which are renormalizing the molecular Hamiltonian $\hat{H}_{\text{mol}}$. These effects are quite generic and appear also in single molecule junctions with different geometries , see e.g. the work by Kaasbjerg et al. [44]. We incorporate these effects with the effective Hamiltonian

$$\hat{H}_{\text{ic}} = -\delta_{\text{ic}} \left(\hat{N} - N_0\right)^2, \tag{3.35}$$

where $\hat{N}$ is the particle number operator, $N_0 = 3$ the number of electrons on the neutral molecule and $\delta_{ic} \approx 0.32$ eV is the strength of the renormalization. This value can be obtained by modelling the tip, molecule and substrate as capacitors and then comparing the average values of the electrostatic energies with the addition energy of the isolated molecule. An STM with an insulating layer between the molecule and the substrate is highly asymmetrical regarding the effect of the bias across the junction on the chemical potential, μ_η of the tip and substrate. The leads are kept at a quasi equilibrium chemical potential

$$\mu_\eta(t) = \mu_\eta^0 + \mathrm{c}_\eta |e| V_{\text{bias}}(t), \tag{3.36}$$

where c_η is the parameter describing how much of the bias voltage V_{bias} drops at the lead η. The dependence of the Fermi and principal functions on the chemical potential sets the regimes where transport can happen. We will assume in this thesis that the equilibrium chemical potential is the same for the tip and the substrate with value $\mu^0 = -4$ eV. To obtain the values for c_η and to also justify the strength of the image charge effect we will consider some electrostatic interactions between the molecule and its environment in the next section.

3.2.2. Electrostatic interactions

The following considerations concerning the electrostatic interactions in the junction can also be found in Ref. [45]. Depending on the geometry of the setup of a single molecule junction a substantial part of the applied bias voltage can drop across the molecule with

$$|\mathrm{c}_{\text{sub}}| + |\mathrm{c}_{\text{tip}}| + |\mathrm{c}_{\text{mol}}| = 1. \tag{3.37}$$

We model the tip and substrate as parallel plate capacitors

$$\begin{aligned} \mathrm{C}_{\mathrm{tip}} &= \varepsilon_0 \frac{A}{h}, \\ \mathrm{C}_{\mathrm{sub}} &= \varepsilon_0 \varepsilon_r \frac{A}{d}, \end{aligned} \tag{3.38}$$

where ε_0 is the vacuum permittivity, $\varepsilon_r = 5.9$ is the permittivity of NaCl, h is the tip-molecule distance, d the thickness of the NaCl layer and $A = 144$Å is an estimate of the CuPc surface. The addition (charging) energy of the neutral molecule is

$$U_0 = E_{N_0+1} - 2E_{N_0} + E_{N_0-1}, \tag{3.39}$$

from which we deduce a capacitance of the molecule as

$$\mathrm{C}_{\mathrm{mol}} = \frac{e^2}{U_0}, \tag{3.40}$$

where the e^2 in the nominator accounts for the fact that U_0 is an energy in the units of eV. If we connect these three capacitors in series we obtain an estimate of the potential drop at each one

$$\mathrm{c}_{\mathrm{sub/tip/mol}} = \frac{\mathrm{C}_{\mathrm{tot}}}{\mathrm{C}_{\mathrm{sup/tip/mol}}}, \tag{3.41}$$

with $\mathrm{C}_{\mathrm{tot}}^{-1} = \mathrm{C}_{\mathrm{sub}}^{-1} + \mathrm{C}_{\mathrm{tip}}^{-1} + \mathrm{C}_{\mathrm{mol}}^{-1}$ being the total capacitance of the junction. Deriving from these considerations we can calculate that for $h = 5$Å, $d = 8$Å and $U_0 = 2.7$ eV about a quarter of the bias is dropping across the molecule. For the relative drops at the substrate and tip we will use

$$\begin{aligned} \mathrm{c}_{\mathrm{sub}} &= 0.16, \\ \mathrm{c}_{\mathrm{tip}} &= -0.59. \end{aligned} \tag{3.42}$$

The strength of the image charge renormalization can be obtained with the same model if one assumes the substrate and tip to be grounded and then brings an elementary charge into the junction. For a more careful description we refer the interested reader to Ref. [45].

3.2.3. The single particle rate matrices

In this section we explain how we form the single particle rate matrices $\Gamma^{\eta}_{\sigma i,\sigma j}$, introduced in Eq. (3.27), for the tip and the substrate. The subscripts σ, σ' denote spin indices of the molecule and i, j are the orbitals. We allow the tip and substrate to be spin polarized. We express this by a measure P^{σ}_{η} of the strength of the polarization with $0 \leq P^{\sigma}_{\eta} \leq 1$, where $P^{\sigma}_{\eta} = 0$ means that the lead η is completely unpolarized, whereas $P^{\sigma}_{\eta} = 1$ expresses complete polarization. The direction of the polarization is expressed

with the azimuth φ and the inclination θ. We choose the z-axis to be the one of the CuPc molecule, as can be seen by the coordinate system in Fig. 3.3. We can thus write for the spin polarization vector

$$\mathbf{P}_\eta^\sigma = P_\eta^\sigma \begin{pmatrix} \sin(\theta^\eta)\cos(\varphi^\eta) \\ \sin(\theta^\eta)\sin(\varphi^\eta) \\ \cos(\theta^\eta) \end{pmatrix}. \tag{3.43}$$

Furthermore, we introduce the vector of Pauli matrices

$$\boldsymbol{\sigma} = \begin{pmatrix} \sigma_x \\ \sigma_y \\ \sigma_z \end{pmatrix}, \tag{3.44}$$

which are defined by

$$\sigma_x = \begin{pmatrix} 0 & 1 \\ 1 & 0 \end{pmatrix}, \ \sigma_y = \begin{pmatrix} 0 & -\mathrm{i} \\ \mathrm{i} & 0 \end{pmatrix}, \ \sigma_z = \begin{pmatrix} 1 & 0 \\ 0 & -1 \end{pmatrix}. \tag{3.45}$$

The rate matrices consist of two parts, the spin part and the angular momentum part,i.e.

$$\Gamma^\eta_{\sigma i,\sigma j} = \Gamma^\eta_{\sigma\sigma'} \otimes \Gamma^\eta_{ij}, \tag{3.46}$$

where the spin part is the same for the substrate and tip and is only depending on the polarization of the substrate (tip)

$$\Gamma^\eta_{\sigma\sigma'} = \frac{\hbar}{2}\left(\mathbb{1}_2 + \mathbf{P}_\eta^\sigma \cdot \boldsymbol{\sigma}\right)_{\sigma\sigma'} \tag{3.47}$$

In the angular momentum part Γ^η_{ij} exist some differences which we explore now. We will start with the substrate

$$\Gamma^{\mathrm{sub}}_{ij} = \frac{2\pi}{\hbar}\sum_{\mathbf{k}} t^{\mathrm{sub}*}_{i\mathbf{k}} t^{\mathrm{sub}}_{j\mathbf{k}} \delta\left(\varepsilon_{\eta\mathbf{k}\sigma} - \Delta E\right). \tag{3.48}$$

We introduce the rotation R_Φ of a symmetry angle Φ around the main symmetry axis. The frontier orbitals will under this transformation acquire a phase which is

$$R_\Phi|i\rangle = \mathrm{e}^{-\mathrm{i}l_i\Phi}, \tag{3.49}$$

where l_i is the angular momentum of the orbital $|i\rangle$. With this we can rewrite Eq. (3.48) as

$$\Gamma^{\mathrm{sub}}_{ij} = \frac{2\pi}{\hbar}\sum_{\mathbf{k}} A \langle i|R_\Phi^\dagger R_\Phi|\mathbf{k}\rangle \langle \mathbf{k}|R_\Phi^\dagger R_\Phi|j\rangle \delta(\varepsilon_{\eta\mathbf{k}\sigma} - \Delta E), \tag{3.50}$$

where $A = \varepsilon_{i\sigma}\varepsilon_{j\sigma}$. If we relabel $\mathbf{k}' = R_\Phi|k\rangle$ this becomes

$$\Gamma^{\mathrm{sub}}_{ij} = \frac{2\pi}{\hbar}\sum_{\mathbf{k}'} A\, \mathrm{e}^{\mathrm{i}\Phi(l_i - l_j)} \langle i|\mathbf{k}'\rangle \langle \mathbf{k}'|j\rangle \delta(\varepsilon_{\eta\mathbf{k}\sigma} - \Delta E) = \mathrm{e}^{i\Phi(l_i-l_j)}\Gamma^{\mathrm{sub}}_{ij}. \tag{3.51}$$

Since the frontier orbitals all have different angular momentum values we can conclude from Eq. (3.51) that the orbital part of the substrate tunnelling rate matrix will be diagonal, i.e.

$$\Gamma^{\text{sub}}_{ij} = \delta_{ij}\Gamma^{\text{sub}}_{ij}. \tag{3.52}$$

The tip however is completely localized. Therefore, we model the angular momentum part as the overlap of the wave functions of the frontier orbitals at the tip position

$$\Gamma^{\text{tip}}_{ij}(\mathbf{r}_{\text{tip}}) = \psi^*_i(\mathbf{r}_{\text{tip}})\psi_j(\mathbf{r}_{\text{tip}}). \tag{3.53}$$

With all this we write for the complete tunnelling rate matrices

$$\begin{aligned}
\Gamma^{\text{sub}}_{i\sigma,j\sigma'} &= \frac{\hbar}{2}\tilde{\Gamma}^{\text{sub}}_0\Big(\mathbb{1}_2 + \mathbf{P}^{\sigma}_{\text{sub}}\cdot\boldsymbol{\sigma}\Big)_{\sigma\sigma'} \otimes \mathbb{1}_4, \\
\Gamma^{\text{tip}}_{i\sigma,j\sigma'}(\mathbf{r}_{\text{tip}}) &= \frac{\hbar}{2}\tilde{\Gamma}^{\text{tip}}_0\Big(\mathbb{1}_2 + \mathbf{P}^{\sigma}_{\text{tip}}\cdot\boldsymbol{\sigma}\Big)_{\sigma\sigma'} \otimes \psi^*_i(\mathbf{r}_{\text{tip}})\psi_j(\mathbf{r}_{\text{tip}}),
\end{aligned} \tag{3.54}$$

with $\tilde{\Gamma}^{\text{sub}}_0$ and $\tilde{\Gamma}^{\text{tip}}_0$ being fitting parameters in the theory.

3.3. The THz-STM

To advance nanotechnology it is crucial to understand excitations happening at the nanoscale. In semiconductors a very successful tool to do this is terahertz spectroscopy. A system is usually excited via a first (pump) THz laser pulse. After a time delay, t_{del}, a second (probe) pulse is applied to gather information about the excitations caused by the first pulse, see refs. [46, 47]. There has been a lot of effort to integrate femtosecond lasers into STM setups with the goal of investigating optically excited vibrational and electronic states while still having the spatial resolution of an STM [48]. Cocker et al. managed in 2013 to couple terahertz pulses to an STM [19]. They excited InAs nanodots which were grown on GaAs by an optical pump pulse. For $t \approx 1-2$ ps after the photoexcitations the nanodots are negatively charged. For $t_{del} \approx 0.5-1$ ps they observed an enhancement in the signal. In 2016 the THz-STM was used for the first time to observe the mechanical oscillations of a Pentacene molecule directly in the time domain [20]. A pump-probe scheme where both pulses where THz pulses tuned in resonance with the Pentacene HOMO was used. The measured current was periodic with respect to the time delay between the two pulses and Fourier analysis revealed a distinct peak around a frequency of 0.5 THz. Their interpretation is that due to tunnelling of an electron from the molecule to the tip the molecule experiences an impulse, based on the abrupt change to Coulomb and van der Waals forces, which drives a dominantly vertical vibration. This changes the relative tip-molecule distance and thus manifests in different currents depending on t_{del}. Principally, this method should also open a door to probe electrical properties directly in the time domain.
We will explore this method in a theoretical way in this thesis with the formalism

presented in the previous section. The bias voltage as presented in Eq. (3.36)

$$\mu_\eta(t) = \mu_\eta^0 + \mathrm{c}_\eta |e| V_{\mathrm{bias}}(t), \tag{3.55}$$

will be generated by a laser pulse impinging into the STM junction. We still assume the chemical potential to be in quasi equilibrium because the change in the large reservoirs is of adiabatic nature with respect to their decay times. Equipped with a model for the CuPc molecule and a transport formalism for the THz-STM we will now start to focus on how to treat this system with numerical and analytical methods. The focus will be on spin-orbit induced dynamics in CuPc and how to make them accessible in electrical measurements.

4. The Two Orbital Model

We will now start to explore the dynamics of the CuPc-THz-STM junction. We will at first take a step back though, and use a simplified model to describe the molecule, to get a feeling which dynamics to expect from the molecule. In this model we will just take the two degenerate LUMOs of CuPc into account and completely neglect the spin.

4.1. Theoretical description of the model

We model the molecular Hamiltonian as

$$\hat{H}_{\mathrm{mol}} = \sum_{\ell_z=\pm 1} \left(\varepsilon + \ell_z \frac{\hbar\omega}{2} \right) \hat{n}_{\ell_z} + \frac{U}{2} \hat{N} \left(\hat{N} - 1 \right), \tag{4.1}$$

with $\varepsilon = 0.2\mathrm{eV}$ the single particle energy of the LUMO orbitals. We introduce an artificial splitting between them via $\ell_z \frac{\hbar\omega}{2} = \ell_z 50\mu\mathrm{eV}$, which is dependent on their angular momentum. The Coulomb interaction is included via the parameter $U = 1\mathrm{eV}$. The particle number operator $\hat{n}_{\ell_z}$ counts the number of particles in the orbital with angular momentum ℓ_z and $\hat{N}$ counts the total number of electrons on the molecule, i.e.

$$\hat{N} = \sum_{\ell_z} \hat{n}_{\ell_z}. \tag{4.2}$$

The tunneling Hamiltonian will be the one as described in Eq. (2.77)

$$\hat{H}_{\mathrm{tun}} = \sum_{\substack{\eta i \\ \sigma \mathbf{k}}} t^{\eta}_{i\mathbf{k}} \hat{c}^{\dagger}_{\eta\mathbf{k}\sigma} \hat{d}_{i\sigma} + \mathrm{h.c.} \tag{4.3}$$

and the leads are described by

$$\hat{H}_{\eta} = \sum_{\eta\mathbf{k}} \left(\varepsilon^{0}_{\eta\mathbf{k}} + \mathrm{c}_{\eta} e \Delta V_{\mathrm{bias}}(t) \right) \hat{n}_{\eta\mathbf{k}}, \tag{4.4}$$

where the bias change, ΔV_{bias}, is generated by a laser pulse. We assume the energy change to be adiabatic with respect to the decay times in the leads. This yields a

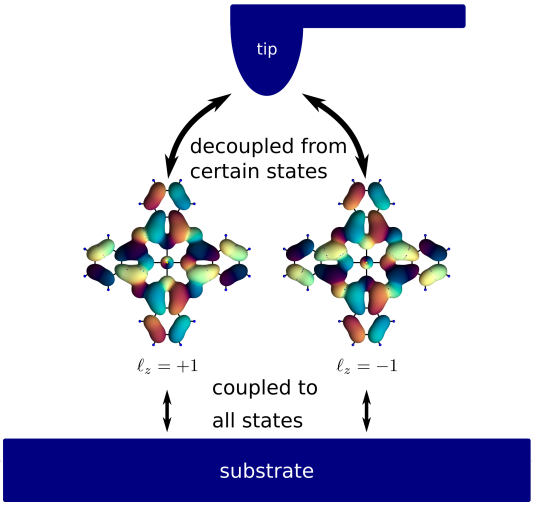

Figure 4.1.: Schematic view of the tunnelling events allowed from/to each lead. The tunnelling from and to the substrate is basis independent coupled to all states whereas the tunnelling from and to the tip is decoupled from some states.

quasi-equilibrium chemical potential

$$\mu_\eta = \mu_0 + \mathrm{c}_\eta e V_{\mathrm{bias}}(t), \tag{4.5}$$

with μ_0 being the equilibrium chemical potential which is the same for each lead and η denotes the tip or substrate. We choose the equilibrium chemical potential to be $\mu_0 = \varepsilon + \frac{U}{2} = 0.7\mathrm{eV}$ and we will work in the Coulomb blockade regime, i.e. $\mathrm{k_B T} \ll U$. For this simplified model we set $\mathrm{c_{sub}} = 0.15$ and $\mathrm{c_{tip}} = -0.85$ to account for the asymmetry in the bias drop across the junction and neglect the bias drop at the molecule. The single particle rates will be described by the angular momentum part introduced in eqs. (3.52) and (3.53) and read

$$\begin{aligned} \Gamma^{\mathrm{tip}}_{\ell_z \ell_z'}(\mathbf{r}_{\mathrm{tip}}) &= \tilde{\Gamma}^0_{\mathrm{tip}} \psi^*_{\ell_z}(\mathbf{r}_{\mathrm{tip}}) \psi_{\ell_z'}(\mathbf{r}_{\mathrm{tip}}), \\ \Gamma^{\mathrm{sub}}_{\ell_z \ell_z'} &= \tilde{\Gamma}^0_{\mathrm{sub}} \delta_{\ell_z \ell_z'}, \end{aligned} \tag{4.6}$$

with $\tilde{\Gamma}^0_{\mathrm{tip}} = \tilde{\Gamma}^0_{\mathrm{sub}} = 10^{-3}$ eV. Since $\Gamma^{\mathrm{sub}}_{\ell_z \ell_z'}$ is diagonal in any basis the substrate is coupled to all states in the molecule. The tip, however, is decoupled from certain states and thus the system can end up in a blocking state as introduced in Sec. 3.1.3. The Hamiltonian in Eq. (4.1) can be easily diagonalized to obtain the four eigenstates and corresponding eigenenergies

$$|0\rangle \to E_0 = 0, \tag{4.7}$$

$$|1\ell_{-1}\rangle \to E_{\ell_{-1}} = \varepsilon - \frac{\hbar\omega}{2}, \tag{4.8}$$

$$|1\ell_{+1}\rangle \to E_{\ell_{+1}} = \varepsilon + \frac{\hbar\omega}{2}, \tag{4.9}$$

$$|2\rangle \to E_2 = 2\varepsilon + U. \tag{4.10}$$

As a next step we will now focus on the many-body tunneling rate matrices of the system. The tunnelling rates between many-body states represent a natural tool for the description of transport phenomena in interacting nanojunctions. They play a fundamental role in the Master equation (3.32) and, as we will see in the next section, they are calculated starting from the single particle rate matrices introduced above.

4.2. Many-body tunnelling rates

We define the many-body tunnelling rate matrices as

$$\Gamma^{\eta}_{N\to N+1} \coloneqq \sum_{\ell\ell'} \langle N+1|\hat{d}^{\dagger}_{\ell'}|N\rangle \, \langle N|\hat{d}_{\ell}|N+1\rangle \, \Gamma^{\eta}_{\ell'\ell}. \tag{4.11}$$

In this section we will mainly focus on the description of the tip tunnelling. Since this process is responsible for coherences in our set-up and thus determines the dynamics we want to investigate. To simplify the notation we will drop the z subscript from the angular momentum quantum number ℓ because we always refer to the z component in this chapter. Furthermore, we will not explicitly write the position dependence of the tunneling rate matrices for the tip if it is not needed to understand the presented equations. For our simplified model the only transitions surviving in the Master equation (3.32) are the $1 \to 0$ and $2 \to 1$ transitions. We define the many-body tunneling matrix elements for the $1 \to 0$ transition

$$\left(\Gamma^{\text{tip}}_{01}\right)_{\ell'\ell} \coloneqq \langle 1\ell'|\hat{d}^{\dagger}_{\ell'}|0\rangle \, \langle 0|\hat{d}_{\ell}|1\ell\rangle \, \Gamma^{\text{tip}}_{\ell'\ell} = \Gamma^{\text{tip}}_{\ell'\ell} \tag{4.12}$$

and for the $2 \to 1$ transition

$$\left(\Gamma^{\text{tip}}_{12}\right)_{\ell'\ell} \coloneqq \langle 1\ell'|\hat{d}_{\bar{\ell}'}|2\rangle \, \langle 2|\hat{d}^{\dagger}_{\bar{\ell}}|1\ell\rangle \, \Gamma^{\text{tip}}_{\bar{\ell}\bar{\ell}'}, \tag{4.13}$$

with the notation $\bar{\ell} = -\ell$. In the following we will use the subscripts $+$ and $-$ to refer to the LUMO with angular momentum $\ell = +1$ and $\ell = -1$ respectively. Analysing the single particle tunnelling matrix yields for the diagonal elements

$$\begin{aligned}
\Gamma^{\text{tip}}_{++}(\mathbf{r}_{\text{tip}}) &= \tilde{\Gamma}^{0}_{\text{tip}} \psi^{*}_{+}(\mathbf{r}_{\text{tip}}) \psi_{+}(\mathbf{r}_{\text{tip}}) \\
&= \frac{\tilde{\Gamma}^{0}_{\text{tip}}}{2} \Big(\psi_{\text{x}}(\mathbf{r}_{\text{tip}}) - \text{i}\psi_{\text{y}}(\mathbf{r}_{\text{tip}})\Big)\Big(\psi_{\text{x}}(\mathbf{r}_{\text{tip}}) + \text{i}\psi_{\text{y}}(\mathbf{r}_{\text{tip}})\Big) \\
&= \tilde{\Gamma}^{0}_{\text{tip}} \psi_{-}(\mathbf{r}_{\text{tip}}) \psi^{*}_{-}(\mathbf{r}_{\text{tip}}) = \Gamma^{\text{tip}}_{--}(\mathbf{r}_{\text{tip}}),
\end{aligned} \tag{4.14}$$

where we have used the decomposition of the imaginary representation of the LUMOs into the real orbitals as introduced in Sec. 2.2.1 and depicted in Fig. 4.2.

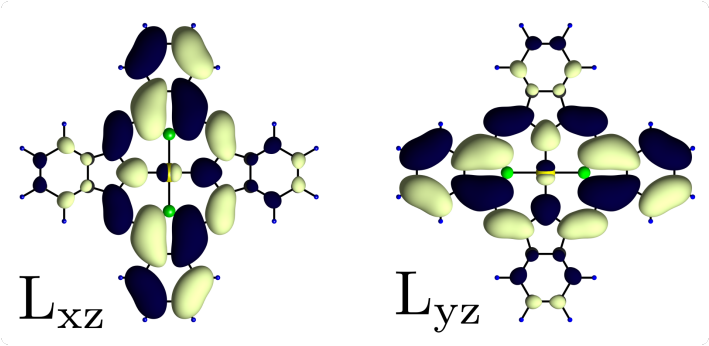

Figure 4.2.: Real representation of the LUMOs.

For the off-diagonal elements we find we find

$$\begin{aligned}\Gamma^{\text{tip}}_{+-}(\mathbf{r}_{\text{tip}}) &= \tilde{\Gamma}^0_{\text{tip}}\psi^*_+(\mathbf{r}_{\text{tip}})\psi_-(\mathbf{r}_{\text{tip}}) \\ &= \frac{\tilde{\Gamma}^0_{\text{tip}}}{2}\Big(\psi_{\text{x}}(\mathbf{r}_{\text{tip}}) - \text{i}\psi_{\text{y}}(\mathbf{r}_{\text{tip}})\Big)\Big(\psi_{\text{x}}(\mathbf{r}_{\text{tip}}) - \text{i}\psi_{\text{y}}(\mathbf{r}_{\text{tip}})\Big) \\ &= \tilde{\Gamma}^0_{\text{tip}}\left(\psi^*_-(\mathbf{r}_{\text{tip}})\psi_+(\mathbf{r}_{\text{tip}})\right)^* = \left(\Gamma^{\text{tip}}_{-+}(\mathbf{r}_{\text{tip}})\right)^*.\end{aligned} \tag{4.15}$$

$\Gamma^{\text{tip}}_{\ell\ell'}$ is therefore a hermitian matrix with equal elements on the diagonal. We turn our attention now to the matrix elements appearing in Eq. (4.13). We find

$$\begin{aligned}&\langle 1 \pm |\hat{d}_{\mp}|2\rangle \langle 2|\hat{d}^\dagger_{\mp}|1\pm\rangle = \left|\langle 2|\hat{d}^\dagger_{\mp}|1\pm\rangle\right|^2 = 1, \\ &\underbrace{\langle 1 + |\hat{d}_-|2\rangle}_{-1}\underbrace{\langle 2|\hat{d}^\dagger_+|1-\rangle}_{1} = \left(\langle 1 - |\hat{d}_+|2\rangle \langle 2|\hat{d}^\dagger_-|1+\rangle\right)^* = -1.\end{aligned} \tag{4.16}$$

This can be brought in the more compact form

$$\langle 1\ell'|\hat{d}_{\bar{\ell}'}|2\rangle \langle 2|\hat{d}^\dagger_{\bar{\ell}}|1\ell\rangle = \text{sgn}(\ell\ell') = \begin{cases} 1, & \text{if } \ell = \ell' \\ -1, & \text{if } \ell \neq \ell' \end{cases} \tag{4.17}$$

Putting together eqs. (4.13) - (4.17) we obtain

$$\begin{aligned}\left(\Gamma^{\text{tip}}_{12}\right)_{++} &= \Gamma^{\text{tip}}_{++} \\ \left(\Gamma^{\text{tip}}_{12}\right)_{--} &= \Gamma^{\text{tip}}_{--} \\ \left(\Gamma^{\text{tip}}_{12}\right)_{+-} &= -\Gamma^{\text{tip}}_{+-} \\ \left(\Gamma^{\text{tip}}_{12}\right)_{-+} &= -\Gamma^{\text{tip}}_{-+}.\end{aligned} \tag{4.18}$$

The description of the substrate tunnelling rate matrices is trivial

$$\Gamma^{\text{sub}}_{01} = \Gamma^{\text{sub}}_{21} = \tilde{\Gamma}^0_{\text{sub}}\mathbb{1}_2 =: \Gamma^{\text{sub}}. \tag{4.19}$$

We are now equipped with the necessary tools to explore the dynamics of our simplified model. This will be done in the next sections.

4.3. Dynamics of the system

To describe the dynamics of this simplified model we express the Master eq. (3.32) in the basis of the molecular Hamiltonian, defined in Eq. (4.7). We use the matrix structure of the many-body tunnelling rates described in the previous section. We analyse the blocks of our Master equation (3.32) as visualized in Fig. 3.1. Furthermore we introduce

$$\hat{H}_1 = \varepsilon \mathbb{1}_2 + \frac{\hbar\omega}{2}\sigma_z, \tag{4.20}$$

which is the Hamiltonian describing the one particle sub block. The zero particle sub block contains one element and is described by

$$\begin{aligned}\dot{\rho}^0 = &- \mathrm{Tr}\left[\Gamma^{\mathrm{sub}} f^+_{\mathrm{sub}}(\hat{H}_1 - E_0) + \Gamma^{\mathrm{tip}}_{01} f^+_{\mathrm{tip}}(\hat{H}_1 - E_0)\right]\rho^0 \\ &+ \mathrm{Tr}\left[\Gamma^{\mathrm{sub}} f^-_{\mathrm{sub}}(\hat{H}_1 - E_0)\rho^1\right] + \frac{1}{2}\mathrm{Tr}\left[f^-_{\mathrm{tip}}(\hat{H}_1 - E_0)\left\{\Gamma^{\mathrm{tip}}_{01}, \rho^1\right\}\right] \\ &+ \frac{\mathrm{i}}{2\pi}\mathrm{Tr}\left[\mathrm{p}_{\mathrm{tip}}(\hat{H}_1 - E_0)\left[\Gamma^{\mathrm{tip}}_{01}, \rho^1\right]\right],\end{aligned} \tag{4.21}$$

with $\{\bullet, \bullet\}$ being the anticommutator and $[\bullet, \bullet]$ the commutator. The two particle sub block also has only one element and the equation has a similar form

$$\begin{aligned}\dot{\rho}^2 = &- \mathrm{Tr}\left[\Gamma^{\mathrm{sub}} f^-_{\mathrm{sub}}(E_2 - \hat{H}_1) + \Gamma^{\mathrm{tip}}_{12} f^-_{\mathrm{tip}}(E_2 - \hat{H}_1)\right]\rho^2 \\ &+ \mathrm{Tr}\left[\Gamma^{\mathrm{sub}} f^+_{\mathrm{sub}}(E_2 - \hat{H}_1)\rho^1\right] + \frac{1}{2}\mathrm{Tr}\left[f^+_{\mathrm{tip}}(E_2 - \hat{H}_1)\left\{\Gamma^{\mathrm{tip}}_{12}, \rho^1\right\}\right] \\ &+ \frac{\mathrm{i}}{2\pi}\mathrm{Tr}\left[\mathrm{p}_{\mathrm{tip}}(E_2 - \hat{H}_1)\left[\Gamma^{\mathrm{tip}}_{12}, \rho^1\right]\right].\end{aligned} \tag{4.22}$$

The one particle sub block is a 2×2 matrix and has the following form

$$\begin{aligned}\dot{\rho}^1 = &- \frac{\mathrm{i}}{\hbar}\left[\hat{H}_1, \rho^1\right] \\ &- \sum_\eta \left\{\frac{\Gamma^\eta_{01}}{2}\left[f^-_\eta(\hat{H}_1 - E_0) - \frac{\mathrm{i}}{\pi}\mathrm{p}_\eta(\hat{H}_1 - E_0)\right]\rho^1 + \mathrm{h.c.}\right\} \\ &- \sum_\eta \left\{\frac{\Gamma^\eta_{12}}{2}\left[f^+_\eta(E_2 - \hat{H}_1) - \frac{\mathrm{i}}{\pi}\mathrm{p}_\eta(E_2 - \hat{H}_1)\right]\rho^1 + \mathrm{h.c.}\right\} \\ &+ \sum_\eta \frac{1}{2}\left\{\left\{f^+_\eta(\hat{H}_1 - E_0), \Gamma^\eta_{01}\right\} + \frac{\mathrm{i}}{\pi}\left[\mathrm{p}_\eta(\hat{H}_1 - E_0), \Gamma^\eta_{01}\right]\right\}\rho^0 \\ &+ \sum_\eta \frac{1}{2}\left\{\left\{f^-_\eta(E_2 - \hat{H}_1), \Gamma^\eta_{12}\right\} + \frac{\mathrm{i}}{\pi}\left[\mathrm{p}_\eta(E_2 - \hat{H}_1), \Gamma^\eta_{12}\right]\right\}\rho^2.\end{aligned} \tag{4.23}$$

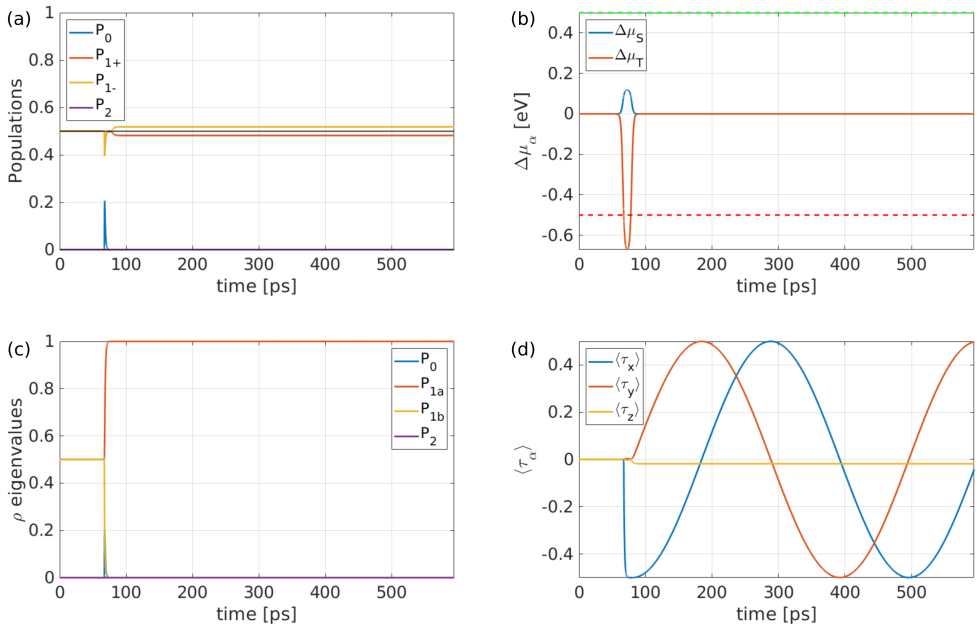

Figure 4.3.: Pseudo spin dynamics of the two orbitals model. (a) The populations of the different states can be seen. (b) The bias change in the substrate and tip due to the laser pulse are shown. The red line shows the threshold for the $1 \to 0$ tip transition and the green line for the $1 \to 2$ substrate transition. (c) Eigenvalues of the density matrix. (d) Evolution of the pseudospin due to the principal parts is depicted.

Since, the zero and two particle sub blocks of ρ only describe the population of the system no internal dynamics will take place if the system is populated with zero or two particles. The one particle block has the dynamics of a two level system with (pseudo) spin $1/2$. It contains the populations of the states $|1+\rangle$ and $|1-\rangle$ and also coherences between these states which can drive dynamics.
A numerical simulation of this system, with the tip located at $x = 5$Å and $y = 0$Å, can be seen in Fig. 4.3. In the beginning the system is in thermal equilibrium, i.e. one particle is on the molecule with an equal probability to be in the $\ell = +$ or $\ell = -$ state. This can be seen in the depiction of the populations in Fig. 4.3(a) and also the eigenvalues of the density matrix Fig. 4.3(c). After roughly 60 ps the bias pulse is applied and opens a $1 \to 0$ tip transition, see Fig. 4.3(b). Consequently we can observe in Fig. 4.3(a) that the system takes an excursion into the zero particle state but decays back to the one particle state before the transition is closed. The state in which the system is trapped in is the one particle blocking state of the type introduced in Sec. 3.1.3. Fig. 4.3(c) visualizes that the blocking state is a pure state because one of the eigenvalues of the density matrix is one. Anticipating the next section we just report here that we see pseudospin dynamics in Fig. 4.3(d). These dynamics enable the system to leave the blocking state after no more bias is applied.

4.4. Pseudo spin formulation of the two orbital model

We now want to reformulate our equations of motion (4.21)- (4.23) in terms of a pseudospin. Therefore, we firstly introduce the pseudospin operators

$$\hat{\tau}_x \coloneqq \frac{1}{2}\sigma_x, \quad \hat{\tau}_y \coloneqq \frac{1}{2}\sigma_y, \quad \text{and} \quad \hat{\tau}_z \coloneqq \frac{1}{2}\sigma_z, \tag{4.24}$$

with σ_i being the Pauli matrices. We can decompose the one particle sub block of the density matrix

$$\rho^1 = \frac{P_1}{2}\mathbb{1}_2 + \tau_x\sigma_x + \tau_y\sigma_y + \tau_z\sigma_z = \frac{P_1}{2}\mathbb{1}_2 + \boldsymbol{\tau}\cdot\boldsymbol{\sigma}, \tag{4.25}$$

where we have introduced the populations

$$P_1 = \operatorname{Tr}\rho^1 \tag{4.26}$$

and the expectation values of the pseudospin operators

$$\tau_i = \frac{1}{2}\operatorname{Tr}\left\{\rho^1\sigma_i\right\} = \langle\hat{\tau}_i\rangle\,. \tag{4.27}$$

To get a concise formulation we will express all matrices as a decomposition in terms of the Pauli matrices. We start with the many-body tunnelling rate matrices of the tip

$$\begin{aligned}\Gamma_{01}^{\text{tip}} &= \tilde{\Gamma}_{\text{tip}}^0\begin{pmatrix}|\psi_+|^2 & \psi_+^*\psi_- \\ \psi_-^*\psi_+ & |\psi_-|^2\end{pmatrix} = \frac{\tilde{\Gamma}_{\text{tip}}^0}{2}\begin{pmatrix}\psi_x^2+\psi_y^2 & \psi_x^2-\psi_y^2-2\mathrm{i}\psi_x\psi_y \\ \psi_x^2-\psi_y^2+2\mathrm{i}\psi_x\psi_y & \psi_x^2+\psi_y^2\end{pmatrix} \\ &= \frac{\tilde{\Gamma}_{\text{tip}}^0}{2}\left[\left(\psi_x^2+\psi_y^2\right)\mathbb{1} + \left(\psi_x^2-\psi_y^2\right)\sigma_x + 2\psi_x\psi_y\sigma_y\right]\end{aligned} \tag{4.28}$$

and

$$\Gamma_{12}^{\text{tip}} = \tilde{\Gamma}_{\text{tip}}^0\begin{pmatrix}|\psi_+|^2 & -\psi_+^*\psi_- \\ -\psi_-^*\psi_+ & |\psi_-|^2\end{pmatrix} = \frac{\tilde{\Gamma}_{\text{tip}}^0}{2}\left[\left(\psi_x^2+\psi_y^2\right)\mathbb{1} - \left(\psi_x^2-\psi_y^2\right)\sigma_x - 2\psi_x\psi_y\sigma_y\right], \tag{4.29}$$

where we have introduced the notation $\psi_{x/z} = \langle\hat{\mathbf{r}}|\mathrm{L}_{\mathrm{xz/yz}}\rangle$. We define the "average" tip tunnelling rate

$$\bar{\Gamma}^{\text{tip}} \coloneqq \frac{\tilde{\Gamma}_{\text{tip}}^0}{2}\left(\psi_x^2+\psi_y^2\right) \tag{4.30}$$

and the tip pseudospin polarization vector

$$\mathbf{P}_{\text{tip}}^{\tau} \coloneqq \begin{pmatrix}\frac{\psi_x^2-\psi_y^2}{\psi_x^2+\psi_y^2} \\ \frac{2\psi_x\psi_y}{\psi_x^2+\psi_y^2} \\ 0\end{pmatrix}. \tag{4.31}$$

This allows us to bring the tip tunnelling rates in eqs. (4.28) and (4.29) in the form

$$\Gamma_{01}^{\text{tip}} = \bar{\Gamma}^{\text{tip}} \left(\mathbb{1}_2 + \mathbf{P}_{\text{tip}}^{\tau} \cdot \boldsymbol{\sigma} \right) \tag{4.32a}$$

$$\Gamma_{12}^{\text{tip}} = \bar{\Gamma}^{\text{tip}} \left(\mathbb{1}_2 - \mathbf{P}_{\text{tip}}^{\tau} \cdot \boldsymbol{\sigma} \right), \tag{4.32b}$$

with $\boldsymbol{\sigma}$ being the vector of Pauli matrices as introduced in Eq. (3.44). To emphasise clearly why we call $\mathbf{P}_{\text{tip}}^{\tau}$ a polarization vector we introduce the angle

$$\Phi_{\text{tip}} \equiv \arctan\left(\frac{2\psi_x \psi_y}{\psi_y^2 - \psi_x^2} \right) - \frac{\pi}{2} \left[\text{sign}\left(\psi_x^2 - \psi_y^2 \right) - 1 \right], \tag{4.33}$$

to rewrite

$$\mathbf{P}_{\text{tip}}^{\tau} = \begin{pmatrix} \cos(\Phi_{\text{tip}}) \\ \sin(\Phi_{\text{tip}}) \\ 0 \end{pmatrix}. \tag{4.34}$$

The angle Φ_{tip} can be seen as the angle of polarization where the norm $\left|\mathbf{P}_{\text{tip}}^{\tau}\right|$ is the sharpness of the tip. This can be seen by assuming $\left|\mathbf{P}_{\text{tip}}^{\tau}\right| = 0$. The tip would then be completely delocalized and thus the tip tunnelling rate matrices would adopt a diagonal form analogous to the substrate. To get a compact form of our analytical expressions in the next chapter we also introduce the "average" tunnelling matrix for the substrate which is

$$\bar{\Gamma}^{\text{sub}} = \tilde{\Gamma}_{\text{sub}}^{0}. \tag{4.35}$$

The vector perpendicular to the molecule is $\mathbf{n}_{\text{mol}} = (0, 0, 1)$ since it is planar and we rewrite the one particle Hamiltonian as

$$\hat{H}_1 = \varepsilon \mathbb{1}_2 + \frac{\hbar\omega}{2} \mathbf{n}_{\text{mol}} \cdot \boldsymbol{\sigma} \tag{4.36}$$

Furthermore, we can decompose every analytical function as

$$f(\hat{H}_1) = \mathbb{1} \bar{f}(\hat{H}_1) + \frac{\delta f(\hat{H}_1)}{2} \mathbf{n}_{\text{mol}} \cdot \boldsymbol{\sigma}, \tag{4.37}$$

with

$$\begin{aligned} \bar{f}(\hat{H}_1) &= \frac{1}{2} \sum_{\ell} f(\hat{H}_{1,\ell\ell}), \\ \delta f(\hat{H}_1) &= \sum_{\ell} \ell f(\hat{H}_{1,\ell\ell}). \end{aligned} \tag{4.38}$$

We find for the Fermi functions and principal parts

$$\begin{aligned} \delta f_{\eta}(\hat{H}_1) &\propto \hbar\omega \ll \bar{\Gamma}^{\eta}, \\ \delta \text{p}_{\eta}(\hat{H}_1) &\propto \hbar\omega \ll \bar{\Gamma}^{\eta}, \end{aligned} \tag{4.39}$$

and thus will neglect this part and approximate them by

$$\begin{aligned} f_\eta &\approx \bar{f}_\eta(\hat{H}_1), \\ \mathrm{p}_\eta(\hat{H}_1) &\approx \bar{\mathrm{p}}_\eta(\hat{H}_1). \end{aligned} \tag{4.40}$$

The explicit reformulation of eqs. (4.21) - (4.23) in terms of populations and pseudospin is shown in App. A.2. With this formulation of the dynamics we will give an analytic evaluation of the dynamics in three different bias regime in the next section.

4.5. Analysis of the three different bias regimes

In this section, we will give an analytic description of the dynamics and we will compare this to our numerical results from Sec. 4.3. For the feasibility of deriving analytic solutions we need to work in the specific limit

$$\Delta E \ll \hbar\bar{\Gamma}^\eta \ll \mathrm{k_B}T \ll U, \tag{4.41}$$

and set the equilibrium chemical potential to $\mu_0 = \varepsilon + {}^{U}/_{2}$. We will analyse the pseudospin dynamics of the system in three different dynamical regimes, as shown in the numerical calculations displayed in Fig. 4.4. The first regime we will investigate is the free evolution of the system which is denoted as the grey box in Fig. 4.4, i.e. the bias is

$$V_{\mathrm{bias}} \ll \frac{U}{2|e c_{\mathrm{tip}}|}, \tag{4.42}$$

where the $\ll$ is taken with respect to the scale set by the temperature. As can be seen best for $V_{\mathrm{bias}} = 0$, but valid for the whole regime, the Fermi functions have the

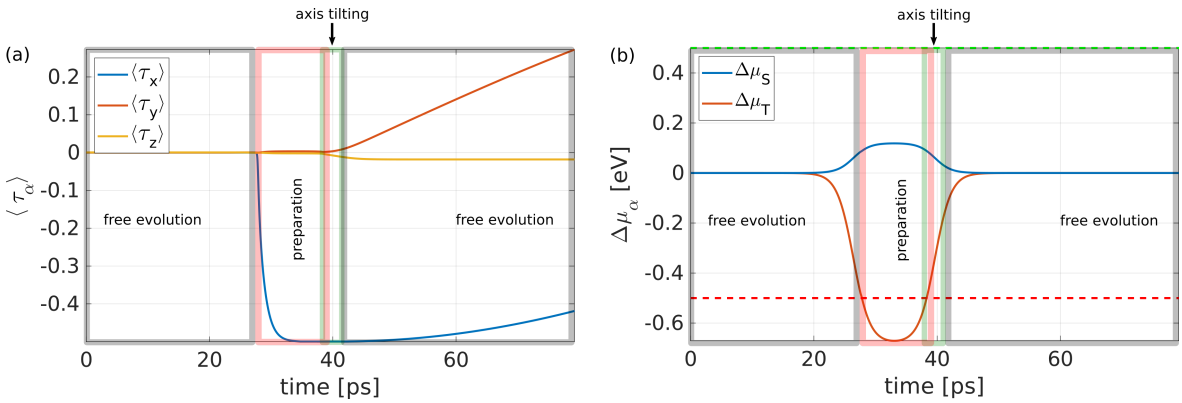

Figure 4.4.: The numerical results of (a) the pseudospin evolution and (b) the bias. The subdivision into the three regimes is depicted by color boxes. The grey box denotes free evolution, the green the tilting of the rotation axis and the red one the preparation phase of the system.

following values

$$\begin{aligned} f_\eta^+(\hat{H}_1 - E_0) &= f_\eta^-(E_2 - \hat{H}_1) = 1, \\ f_\eta^-(\hat{H}_1 - E_0) &= f_\eta^+(E_2 - \hat{H}_1) = 0. \end{aligned} \tag{4.43}$$

Since, we set our equilibrium chemical potential to $\mu_0 = \varepsilon + {}^U/_2$ it holds that

$$\mathrm{p}_\eta(E_2 - E_1) = \mathrm{p}_\eta(E_1 - E_0). \tag{4.44}$$

With this we are able, in this bias regime, to rewrite eqs. (4.21)- (4.23), analogous to Ref. [49], as equations for the populations P_0, P_1, P_2 and the pseudospin $\boldsymbol{\tau}$. They adopt the following form

$$\dot{P}_0 = -2\sum_\eta \bar{\Gamma}^\eta P_0 \tag{4.45}$$

$$\dot{P}_1 = 2\sum_\eta \bar{\Gamma}^\eta \left(P_0 + P_2\right) \tag{4.46}$$

$$\dot{P}_2 = -2\sum_\eta \bar{\Gamma}^\eta P_2 \tag{4.47}$$

$$\dot{\boldsymbol{\tau}} = \omega\left(\mathbf{n}_{\mathrm{mol}} \times \boldsymbol{\tau}\right) + \bar{\Gamma}^{\mathrm{tip}}\left(P_0 - P_2\right)\mathbf{P}_\tau^\eta. \tag{4.48}$$

The equations for the populations have to be complemented by the condition

$$P_0 + P_1 + P_2 = 1, \tag{4.49}$$

which is the fundamental condition that $\mathrm{Tr}\,\rho = 1$. With this one can easily see that the populations will be

$$P_0 = 0, \;\; P_1 = 1, \;\text{and}\; P_2 = 0, \tag{4.50}$$

on a timescale which is set by $\left(\bar{\Gamma}^{\mathrm{tip}}\right)^{-1}$. The reason why this holds is that the populations of the zero and two particle sub block are only decreasing in this regime. The only term which is then remaining in Eq. (4.48) is the precession of $\boldsymbol{\tau}$ around $\mathbf{n}_{\mathrm{mol}}$ with the frequency ω.

The second regime we investigate is reached when the bias is such that the $1 \to 0$ tip transition is open but no $1 \to 2$ substrate transition is allowed. It is represented by the red box in Fig. 4.4. This means that the bias needs to fulfill

$$\frac{U}{2|e\mathrm{c}_{\mathrm{tip}}|} \ll V_{\mathrm{bias}} \ll \frac{U}{2|e\mathrm{c}_{\mathrm{sub}}|}. \tag{4.51}$$

The only Fermi functions which are nonzero in this regime are

$$f_{\mathrm{tip}}^-(\hat{H}_1 - E_0) = f_{\mathrm{sub}}^+(\hat{H}_1 - E_0) = f_\eta^-(E_2 - \hat{H}_1) = +1. \tag{4.52}$$

Furthermore, we define

$$\begin{aligned} \bar{\mathrm{p}}_{\mathrm{tip}}(H_{01}) &\coloneqq \bar{\mathrm{p}}_{\mathrm{tip}}(\hat{H}_1 - E_0), \\ \bar{\mathrm{p}}_{\mathrm{tip}}(H_{21}) &\coloneqq \bar{\mathrm{p}}_{\mathrm{tip}}(E_2 - \hat{H}_1). \end{aligned} \tag{4.53}$$

With this we find for eqs. (4.21) - (4.23) in this regime, once again in analogy to Ref. [49],

$$\dot{P}_0 = -2\Gamma^{\text{sub}} P_0 + \bar{\Gamma}^{\text{tip}} P_1 + 2\bar{\Gamma}^{\text{tip}} \mathbf{P}^{\tau}_{\text{tip}} \cdot \boldsymbol{\tau}, \tag{4.54}$$

$$\dot{P}_1 = -\bar{\Gamma}^{\text{tip}} P_1 - 2\bar{\Gamma}^{\text{tip}} \mathbf{P}^{\tau}_{\text{tip}} \cdot \boldsymbol{\tau} + 2\Gamma^{\text{sub}} P_0 + 2\sum_{\eta} \bar{\Gamma}^{\eta} P_2, \tag{4.55}$$

$$\dot{P}_2 = -\sum_{\eta} 2\bar{\Gamma}^{\eta} P_2, \tag{4.56}$$

$$\dot{\boldsymbol{\tau}} = \left[\omega \mathbf{n}_{\text{mol}} - \frac{\bar{\Gamma}^{\text{tip}}}{\pi}\left[\bar{\text{p}}_{\text{tip}}(H_{01}) - \bar{\text{p}}_{\text{tip}}(H_{21})\right]\mathbf{P}^{\tau}_{\text{tip}}\right] \times \boldsymbol{\tau} \tag{4.57}$$

$$- \bar{\Gamma}^{\text{tip}} \boldsymbol{\tau} - \frac{\bar{\Gamma}^{\text{tip}}}{2} P_1 \mathbf{P}^{\tau}_{\text{tip}} - \bar{\Gamma}^{\text{tip}} P_2 \mathbf{P}^{\tau}_{\text{tip}}.$$

The populations fulfill

$$P_0 = 0, \; P_1 = 1 \text{ and } P_2 = 0. \tag{4.58}$$

Even though the transition $1 \to 0$ via the tip is in principle still open the system will remain in the one particle state. This is the interference blocking state we introduced in Sec. 3.1.3. The second line of Eq. (4.57) is solved by

$$\boldsymbol{\tau} = \frac{-\mathbf{P}^{\tau}_{\text{tip}}}{2}. \tag{4.59}$$

However, if we are over threshold the first line can be neglected. The first reason is that the timescale on which tunnelling events are happening is much shorter than the timescale set by the frequency ω, as can be seen in Fig. 4.3(d). The second reason is that difference of the principal parts appearing in Eq. (4.57) is highly localized around the threshold, which is $V_{\text{bias}} = {}^{U}/_{2|ec_{\text{tip}}|}$. This is shown in Fig. 4.5. However, this term has contributions on the same timescale as the tunneling events. Therefore, we define a third bias regime around

$$V_{\text{bias}} \approx \frac{U}{2|ec_{\text{tip}}|}, \tag{4.60}$$

with the extra condition that

$$\boldsymbol{\tau} \neq \mathbf{0}. \tag{4.61}$$

This regime is shown in the green box in Fig. 4.4. The principal parts tilts the axis of rotation in this regime so that precession does not only take place around the axis perpendicular to the molecule. Since the correction is rather small the complete blocking state is a good assumption after the preparation.
We have shown in this chapter that by subdividing the bias in three different regimes we are able to completely describe our numerical results shown in the last section with analytical solutions. An experimental access to the dynamics described in this section may be obtained via a pump-probe schemes. The effects of the dynamics on the potential measurements in this scheme will be shown in the next section.

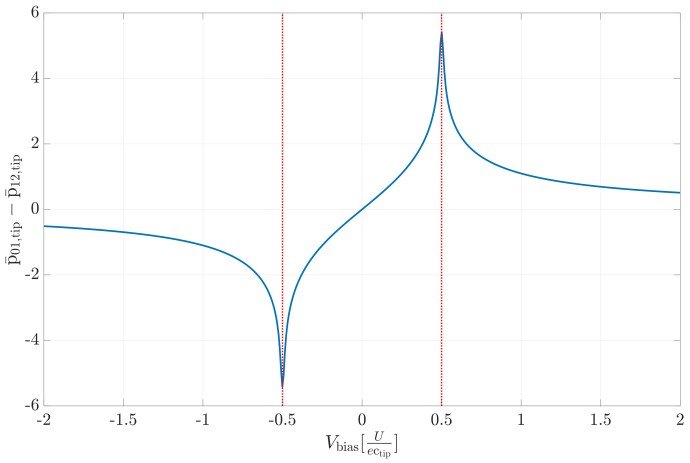

Figure 4.5.: The difference between the principal parts as appearing in Eq. (4.57). We report on the x-axis the bias in units of U/ec_{tip}. One can see that the term is highly localized around 0.5 which is exactly resonance for the $1 \to 0$ transition.

4.6. Pump-probe readout of the dynamics

The dynamics of our model may be explored experimentally via a pump-probe scheme. To this extent the system is prepared via a pump pulse and then after some time t_{del} a second pulse is applied to read out the state of the system.However, the pseudospin dynamics are not measurable directly in a THz-STM set-up. We will in this section make a connection between the internal pseudospin dynamics and the transferred charge per pump probe cycle, which is a measurable quantity. As we have seen in the previous section the free evolution of the pseudospin is described by a precession around the axis perpendicular the molecule

$$\dot{\boldsymbol{\tau}} = \omega \left(\mathbf{n}_{\text{mol}} \times \boldsymbol{\tau} \right). \tag{4.62}$$

We will assume a perfect preparation after the pump pulse, i.e.

$$\boldsymbol{\tau}(0) = -\frac{\mathbf{P}^{\tau}_{\text{tip}}}{2}. \tag{4.63}$$

Eqs. (4.62) and (4.63) read in components

$$\dot{\tau}_x = -\omega \tau_y \qquad \tau_x(0) = -\frac{1}{2}\cos(\Phi_{\text{tip}}) \tag{4.64}$$

$$\dot{\tau}_y = \omega \tau_x \qquad \tau_y(0) = -\frac{1}{2}\sin(\Phi_{\text{tip}}) \tag{4.65}$$

$$\dot{\tau}_z = 0 \qquad \tau_z(0) = 0. \tag{4.66}$$

These equations are solved by

$$\tau_x(t) = -\frac{1}{2}\cos(\omega t + \Phi_{\text{tip}}) \tag{4.67}$$

$$\tau_y(t) = -\frac{1}{2}\sin(\omega t + \Phi_{\text{tip}}) \tag{4.68}$$

$$\tau_z(t) = 0 \tag{4.69}$$

Already at this stage it is possible to make some predictions about the charge transferred by the probe pulse. If the time delay between the two pulses is $t_{\text{del}} = {}^{2\pi}/_{\omega}$ the system is in the one particle state specified by

$$\tau_x(\tfrac{2\pi}{\omega}) = -\frac{1}{2}\cos(2\pi + \Phi_{\text{tip}}) \tag{4.70}$$

$$\tau_y(\tfrac{2\pi}{\omega}) = -\frac{1}{2}\sin(2\pi + \Phi_{\text{tip}}) \tag{4.71}$$

$$\tau_z(\tfrac{2\pi}{\omega}) = 0. \tag{4.72}$$

This, however, is the initial state as given in Eq. (4.63) and visualized in Fig. 4.6(d) which is the interference blocking state. Thus the probe pulse will not transmit any charge, as shown in Fig. 4.6(c). The other extreme value of the charge transfer is reached when the time delay is $t_{\text{del}} = {}^{\pi}/_{\omega}$. The system is then in the state

$$\tau_x(\tfrac{\pi}{\omega}) = -\frac{1}{2}\cos(\pi + \Phi_{\text{tip}}) \tag{4.73}$$

$$\tau_y(\tfrac{\pi}{\omega}) = -\frac{1}{2}\sin(\pi + \Phi_{\text{tip}}) \tag{4.74}$$

$$\tau_z(\tfrac{\pi}{\omega}) = 0. \tag{4.75}$$

The system is then the "farthest" away from the blocking state so the charge transferred by the probe pulse will be maximal, see Fig. 4.7(d) and Fig. 4.7(c).

For a more general description of the charge transfer we need to calculate the expectation value of the $1 \to 0$ transition

$$\langle \Gamma_{01}^{\text{tip}} \rangle(t) = \left\langle \bar{\Gamma}^{\text{tip}} \begin{pmatrix} 1 & e^{i\Phi_{\text{tip}}} \\ e^{-i\Phi_{\text{tip}}} & 1 \end{pmatrix} \right\rangle(t) \equiv \text{Tr}\{\rho^1(t)\Gamma_{01}^{\text{tip}}\}. \tag{4.76}$$

We rewrite the one particle block of the density matrix as

$$\rho^1(t) = \frac{1}{2}\mathbb{1} - \frac{1}{2}\cos(\omega t + \Phi_{\text{tip}})\sigma_x - \frac{1}{2}\sin(\omega t + \Phi_{\text{tip}})\sigma_y. \tag{4.77}$$

As a first step we will calculate the transmitted charge of the pump pulse, i.e. the system is in thermal equilibrium and therefore $\rho^1_{\text{therm}} = {}^1/_2\mathbb{1}$. We find

$$\langle \Gamma_{01}^{\text{tip}} \rangle_{\text{therm}} = \frac{\bar{\Gamma}^{\text{tip}}}{2} \text{Tr}\left\{(\mathbb{1} + \cos(\Phi_{\text{tip}})\sigma_x + \sin(\Phi_{\text{tip}})\sigma_y)\,\mathbb{1}\right\} = \bar{\Gamma}^{\text{tip}}. \tag{4.78}$$

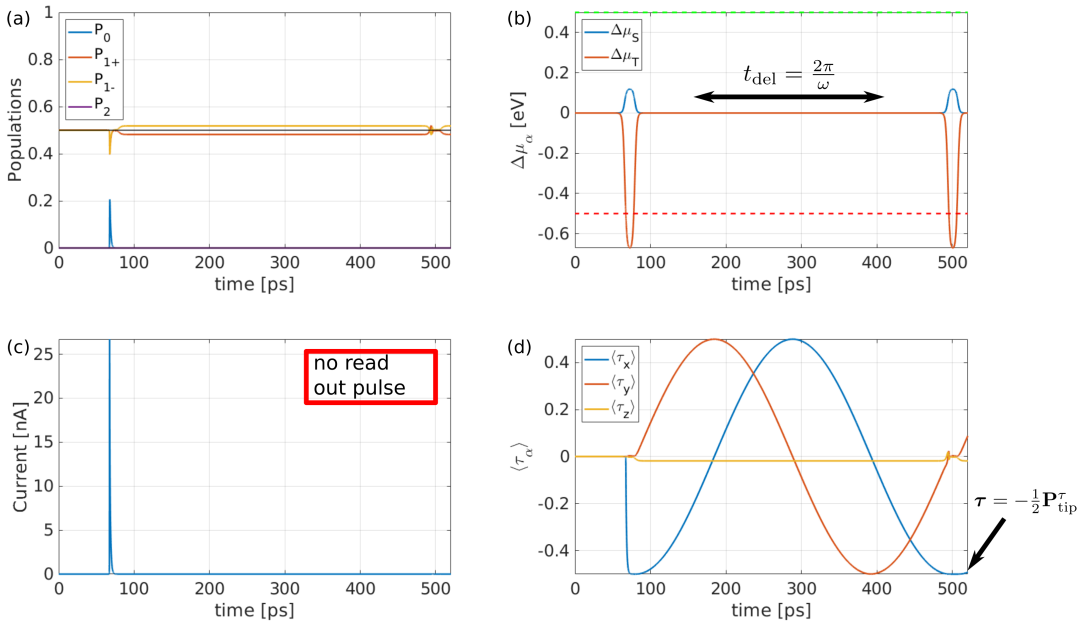

Figure 4.6.: Pump probe scheme with $t_{\text{del}} = 2\pi/\omega$ between the two pulses. We report the populations (a), the change in the chemical potential due to the pulses (b), the current per pulse (c) and the dynamics of the pseudospin (d). Since the system is again in the blocking state when the second pulse is applied, there is no current flowing during the second pulse.

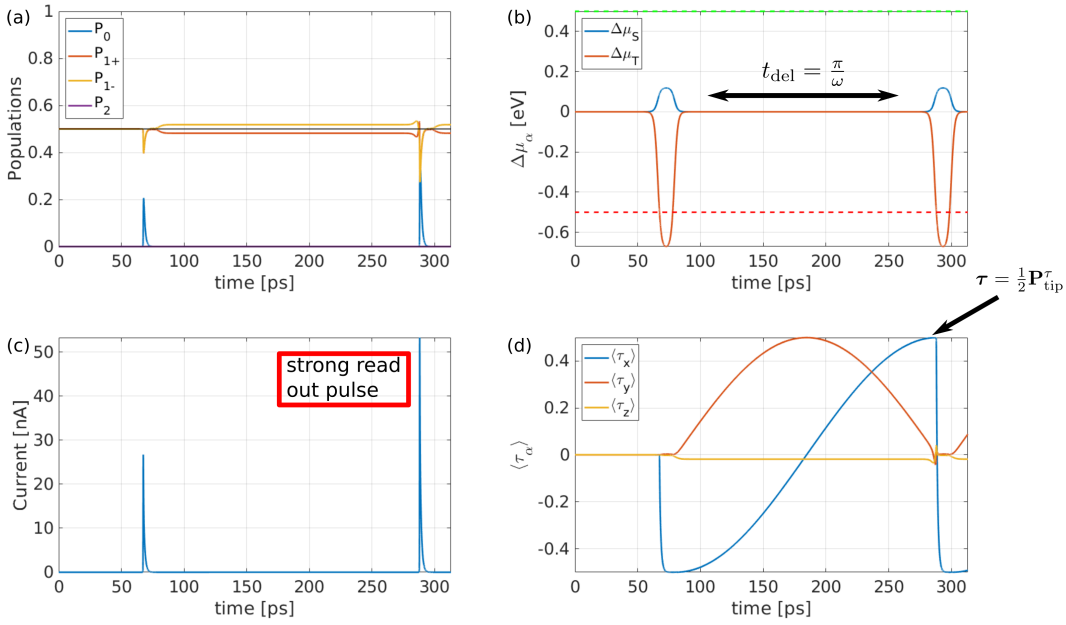

Figure 4.7.: Pump probe scheme with $t_{\text{del}} = \pi/\omega$ between the two pulses. We report the populations (a), the change in the chemical potential due to the pulses (b), the current per pulse (c) and the dynamics of the pseudospin (d). The pseudospin value $\boldsymbol{\tau}_x$ is farthest away from the blocking state thus there is a strong read out pulse visible in panel (c).

For the time dependent part we obtain

$$\begin{aligned}
&\langle \Gamma_{01}^{\text{tip}} \rangle(t) = \\
&\frac{\bar{\Gamma}^{\text{tip}}}{2} \operatorname{Tr}\left\{ (\mathbb{1} + \cos(\Phi_{\text{tip}})\sigma_x + \sin(\Phi_{\text{tip}})\sigma_y)\,(\mathbb{1} - \cos(\omega t + \Phi_{\text{tip}})\sigma_x - \sin(\omega t + \Phi_{\text{tip}})\sigma_y) \right\} = \\
&\frac{\bar{\Gamma}^{\text{tip}}}{2} \operatorname{Tr}\left\{ \mathbb{1}\left[1 - \cos(\Phi_{\text{tip}})\cos(\omega t + \Phi_{\text{tip}}) - \sin(\Phi_{\text{tip}})\sin(\omega t + \Phi_{\text{tip}})\right] \right\} = \\
&\bar{\Gamma}^{\text{tip}} \left[1 - \frac{1}{2}\Big(\cos(\omega t + 2\Phi_{\text{tip}}) + \cos(\omega t) \Big) - \frac{1}{2}\Big(\cos(\omega t) - \cos(\omega t + 2\Phi_{\text{tip}}) \Big) \right] = \\
&\bar{\Gamma}^{\text{tip}}\,(1 - \cos(\omega t))\,.
\end{aligned} \tag{4.79}$$

The mixed terms vanish between line 2 and 3 of the equation because it holds for the Pauli matrices that

$$\operatorname{Tr} \sigma_i = 0. \tag{4.80}$$

The transferred charge per pump-probe cycle will thus be proportional to the sum of Eq. (4.78) and Eq. (4.79). It needs to be fitted to the charge transferred via the pump pulse, i.e.

$$Q_{\text{tip}}(t) = Q_{\text{tip}}(0)\,(2 - \cos(\omega t))\,. \tag{4.81}$$

In Fig. 4.8 we see the charge transfer with the tip fixed at the positions $x = 5$Å and $y = 0$Å. However, the position dependence of the tip is implicitly included in the tunnelling rate matrix Γ_{01}^{tip} and therefore Eq. (4.76) is valid for the whole molecule. In Fig. 4.9 we show a map of the transferred charge along the positive x-axis of the molecule and a plot of the absolute value of the wave function. We see that our derived equation for the charge transfer holds along the axis. The regions where no transfer is happening is due to nodes in the wave function and thus there is no charge transfer to the tip possible.

We conclude that we are able to combine the internal pseudospin dynamics of our model with the measurable charge transfer. This is a very important result because otherwise there would be no chance to investigate our predicted dynamics by experiments. Equipped with the knowledge about the simplified model we will now return to the full molecule and investigate the coupled dynamics of spin and pseudospin.

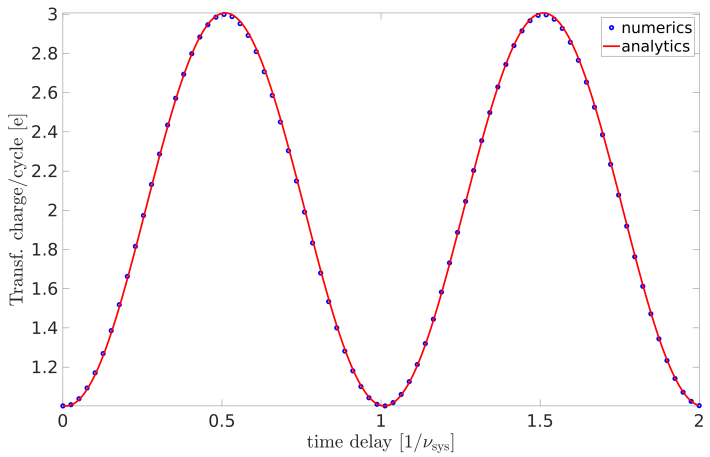

Figure 4.8.: Charge transfer per pump-probe cycle depending on the time delay between the two pulses with a fixed tip position at $x = 5$Å and $y = 0$Å.

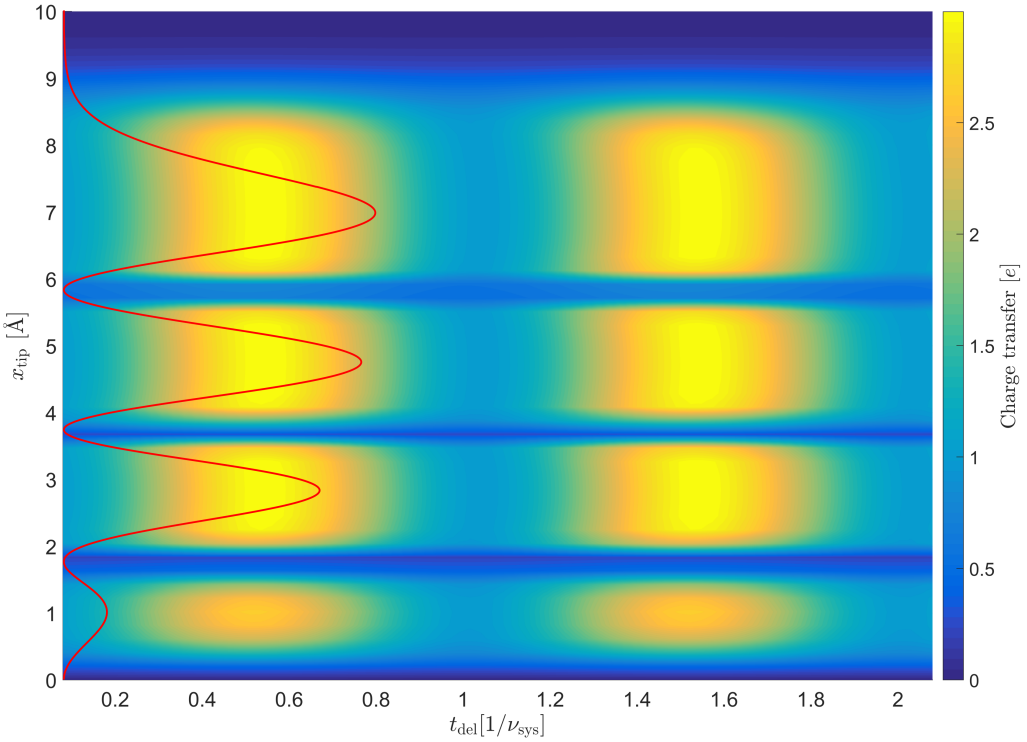

Figure 4.9.: Charge transfer per pump-probe cycle. The y position of the tip is fixed at $y = 0$Å, whereas the x position is varied between $x = 0$Å and $x = 10$Å. The red line shows the absolute value of ψ_x along the x-axis.

5. Numerical evaluation of the full system

Equipped with a better understanding of the orbital dynamics to expect in the system we will now turn our eye to the THz-STM set up with the full model describing the molecule. First, we will gather some theoretical prerequisites. After that we will investigate the dynamics of the full system numerically.

5.1. Theoretical prerequisites

In this section we collect the necessary theoretical prerequisites. First, we explore how to treat the Fock space, then how to handle the principal parts and finally we give a definition of our spin and pseudospin operators.

5.1.1. Treatment of the Fock space

As already mentioned in Sec. 2.2.3, the Fock space spanned by the molecular Hamiltonian (2.34) has a dimension of $4^4 = 256$. Since, we keep coherences in our transport

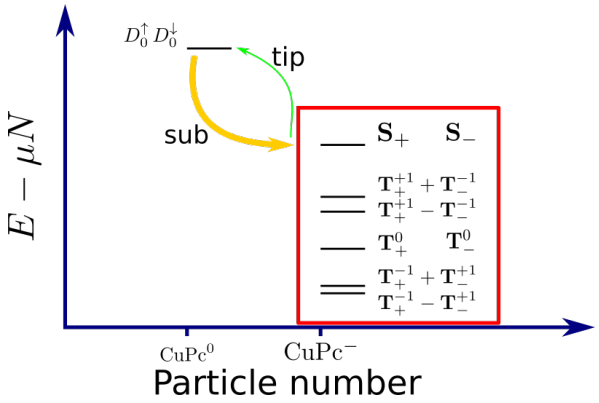

Figure 5.1.: Schematic depiction of the considered transitions in the system. We show on the x-axis the neutral and anionic state of CuPc and on the y-axis the grand canonical energy of the states.

calculations the corresponding Liouville space has a dimension of 256^2. Despite the possibility to numerically diagonalize the Hamiltonian the Liouville space is too big to make numerical transport calculations in a reasonable time frame. However, we are interested in transport at low energies. This enables us to only take the lowest lying states of the neutral and anionic molecule into account. They are shown in Fig. 5.1. In particular we will only consider the states discussed in Sec. 2.3 for tunnelling events. Such events are described by the real part of Eq. (3.32), i.e. the parts containing the Fermi functions. The ten states considered for transport make up our active Fock space of tunnelling events. The imaginary parts of Eq. (3.32) need a more careful treatment. First of all we exclude them in the parts of the equation which are connected to the increase of the sub block of the density matrix, i.e. the last two lines. We do this since the difference between the principal part functions appearing in these two lines is of order $\Gamma^{\eta}_{\sigma i,\sigma j}$ and thus would give us contributions to the Master equation which are of order $(\Gamma^{\eta}_{\sigma i,\sigma j})^2$. This however is inconsistent with our second order treatment of the transport set-up and leads to wrong numerical results.
In the parts of the equation we keep the imaginary parts we still have to be more careful than for the real parts of the equation. We do that since in the imaginary parts virtual transitions can happen which must be taken into account when doing transport calculations. To give an example on how to include the virtual transitions into this formulation we will take a look at the term

$$\begin{aligned}
&\sum_{\eta F}\sum_{\substack{i\sigma\\ j\sigma'}} P_{NE}\hat{d}^{\dagger}_{i\sigma}\mathrm{p}_{\eta}(F-\hat{H}_{\mathrm{mol}})\hat{d}_{j\sigma'}P_{NF}\rho P_{NE'} = \\
&\sum_{\eta F F'}\sum_{\substack{i\sigma\\ j\sigma'}}\sum |NE\rangle\langle EN|\hat{d}^{\dagger}_{i\sigma}\mathrm{p}_{\eta}(F-\hat{H}_{\mathrm{mol}})|N-1F'\rangle\langle F'N-1|\hat{d}_{j\sigma'}|NF\rangle\langle FN|\rho P_{NE'} = \\
&\sum_{\eta F F'}\sum_{\substack{i\sigma\\ j\sigma'}}\mathrm{p}_{\eta}(F-F')\langle EN|\hat{d}^{\dagger}_{i\sigma}|N-1F'\rangle\langle F'N-1|\hat{d}_{j\sigma'}|NF\rangle|NE\rangle\langle FN|\rho P_{NE'},
\end{aligned} \tag{5.1}$$

which is appearing in the first line of Eq. (3.32). We neglect the angular momentum quantum numbers in the projection operators to keep the formula clearly arranged. The sum over F only runs over the active Fock space, i.e. the low energy spectrum, whereas F' will run over all states in the $N-1$ particle spectrum. With this we include all virtual transitions which can happen into our numerical calculations. In the next section we will define an effective Hamiltonian for the imaginary parts which allows us to treat the numerics more efficiently.

5.1.2. Effective Hamiltonian for the principal parts

To obtain an effective Hamiltonian for the principle parts we define first

$$M = -\sum_{\eta F}\sum_{\substack{i\sigma\\ j\sigma'}}\frac{\Gamma^{\eta}_{\sigma i,\sigma j}}{2\pi}P_{NE}\left[\hat{d}^{\dagger}_{i\sigma}\mathrm{p}_{\eta}(F-\hat{H}_{\mathrm{mol}})\hat{d}_{j\sigma'}+\hat{d}_{j\sigma'}\mathrm{p}_{\eta}(\hat{H}_{\mathrm{mol}}-F)\hat{d}^{\dagger}_{i\sigma}\right]P_{NF}. \tag{5.2}$$

We define the effective Hamiltonian for the principal parts as

$$\hat{H}_{\mathrm{pp}} = \frac{M + M^{\dagger}}{2}. \tag{5.3}$$

This enables us to include the dependence of the density matrix on the principal parts into the Master equation (3.32) by

$$\dot{\rho} \propto -\mathrm{i}\left[\hat{H}_{\mathrm{pp}}, \rho\right]. \tag{5.4}$$

We will now turn our attention to the definition of the spin and pseudospin operators for our full system.

5.1.3. Spin and pseudospin operators

Since we are interested in the spin and pseudospin dynamics we need to define operators which are able to describe them. We define for the spin

$$\hat{S}_x = \frac{1}{2}\sum_{i\sigma\sigma'} \hat{d}^{\dagger}_{i\sigma}(\sigma_x)_{\sigma\sigma'}\hat{d}_{i\sigma'} \tag{5.5a}$$

$$\hat{S}_y = \frac{1}{2}\sum_{i\sigma\sigma'} \hat{d}^{\dagger}_{i\sigma}(\sigma_y)_{\sigma\sigma'}\hat{d}_{i\sigma'} \tag{5.5b}$$

$$\hat{S}_z = \frac{1}{2}\sum_{i\sigma\sigma'} \hat{d}^{\dagger}_{i\sigma}(\sigma_z)_{\sigma\sigma'}\hat{d}_{i\sigma'}, \tag{5.5c}$$

with i and j running over the complete set of frontier orbitals. For the pseudospin we only take the LUMOs into account and define the corresponding operators as

$$\hat{\tau}_x = \frac{1}{2}\left(\hat{n}_{\mathrm{H}} - 1\right)\sum_{\substack{\xi,\xi'=\pm\\ \sigma}} \hat{d}^{\dagger}_{\mathrm{L}\xi\sigma}(\sigma_x)_{\xi\xi'}\hat{d}_{\mathrm{L}\xi'\sigma}, \tag{5.6a}$$

$$\hat{\tau}_y = \frac{1}{2}\left(1 - \hat{n}_{\mathrm{H}}\right)\sum_{\substack{\xi,\xi'=\pm\\ \sigma}} \hat{d}^{\dagger}_{\mathrm{L}\xi\sigma}(\sigma_y)_{\xi\xi'}\hat{d}_{\mathrm{L}\xi'\sigma}, \tag{5.6b}$$

$$\hat{\tau}_z = \frac{1}{2}\sum_{\substack{\xi,\xi'=\pm\\ \sigma}} \hat{d}^{\dagger}_{\mathrm{L}\xi\sigma}(\sigma_z)_{\xi\xi'}\hat{d}_{\mathrm{L}\xi'\sigma}. \tag{5.6c}$$

We define the pseudospin operators in this way to ensure that they fulfill

$$[\hat{\tau}_\alpha, \hat{\tau}_\beta] = \mathrm{i}\varepsilon_{\alpha\beta\gamma}\hat{\tau}_\gamma \tag{5.7}$$

on the triplet anionic subspace, with $\varepsilon_{\alpha\beta\gamma}$ being the Levi-Civita symbol. We now have all necessary ingredients to turn our eyes to the numerical simulations of the full system. We do this in the next chapters.

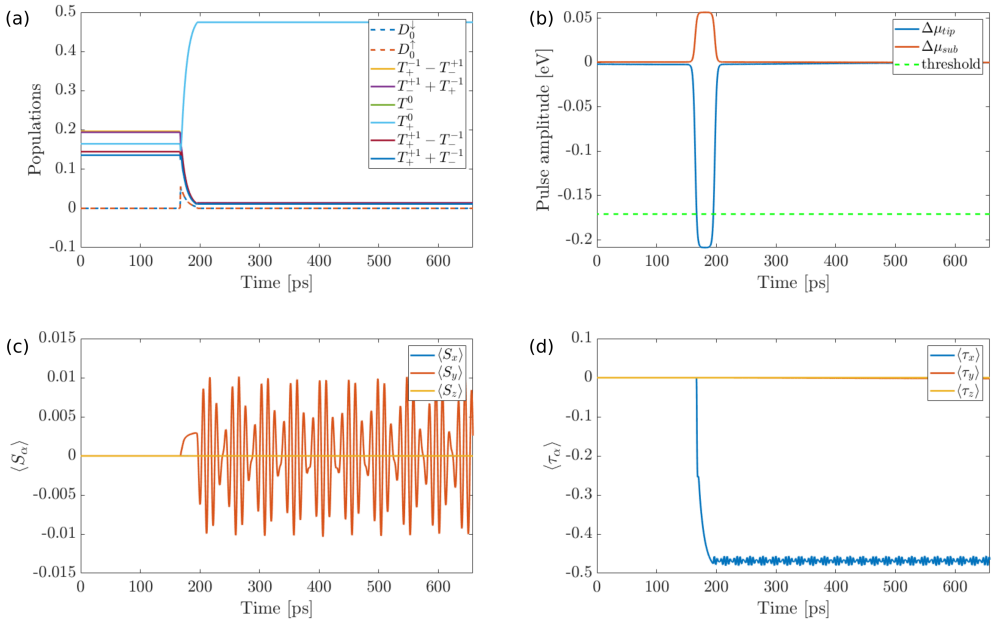

Figure 5.2.: Simulation of the full system driven by a laser pulse of width 30ps. We report in (a) the populations of the system, (b) the bias change in each lead due to the laser pulse, (c) the expectation value of the spin and (d) the expectation value of the pseudospin.

5.2. Simulations with unpolarized leads

We will now show the numerically obtained results for the full system. As a first step we will investigate the effect of the pulse width on the dynamics and then turn our attention to the effect of spin polarized leads.

5.2.1. Blocking state in the full system

If we once again set the tip at the position $x = 5$Å and $y = 0$Å we expect to find the same orbital blocking state as in the simplified two orbitals model since it should only depend on the LUMOs which we took into account in our model. We report the simulation of the system without spin polarized leads in Fig. 5.2. All simulations presented in this chapter have been performed at a temperature of $T = 30$K and we will neglect the singlet states of the anionic low energy spectrum. This is justified since they do not have any influence on the spin-orbit dynamics of the system. We set $\mu_0 = -4$eV for our system which has the effect that in thermal equilibrium the molecule will be in its anionic state. We see in the plot of the populations, Fig. 5.2(a), that before a laser pulse is applied the system is in thermal equilibrium, i.e. all triplet states have a nonzero probability of being occupied with small differences due to sizable energy splittings on the temperature scale. After around 180ps a laser pulse is applied to open

the transition from the anionic to the neutral state for 30ps which can be seen by the chemical potential of the tip crossing the green threshold line in Fig. 5.2(b). We can see now a similar behaviour as exhibited by the model. In the populations, Fig. 5.2(a), we see that the probability to occupy the neutral state rises when the transition opens, but then decays even though the transition is in principle still open. We also see in the population plot that after the transition is closed the mainly occupied states are the two degenerate triplet states $|\mathbf{T}^0_\pm\rangle$.
To get an understanding why the populations are showing this behaviour let's assume that the term containing λ_2 in the molecular Hamiltonian, see Eq. (2.34), would be zero. The four vanishing triplet states would then be eigenstates of the total spin operator $\hat{S}^2 = \hat{S}_x^2 + \hat{S}_y^2 + \hat{S}_z^2$. Hence, superselection rules prohibit the preparation of a superposition of these states. The term containing λ_2 introduces small admixtures to states with different total spin and thus they do not vanish completely but have a very little probability of being occupied.
The states $|\mathbf{T}^0_\pm\rangle$ are exactly degenerate and therefore can not be responsible for internal dynamics. Consequently, in Fig. 5.2(c) and Fig. 5.2(d) we see a very small amplitude in the oscillations of the spin and pseudospin expectation values, respectively. The corresponding dynamics would probably be too small to be measured experimentally. Therefore we will not analyse them in more detail. As we will see in the next section for a shorter laser pulse we ill not completely reach the blocking state and obtain much more pronounced dynamics.

5.2.2. Shorter pulse to drive the system

In the last section we saw that for a long pulse the system approaches the blocking state and that the coherent dynamics are then probably not measurable. If we shorten the time interval in which the transition from the anionic to the neutral state via the tip is open by a factor of ten, i.e. it is open for 3ps as shown in Fig. 5.3(b), we see in Fig. 5.3(a) that the system does not have enough time to decay back into the anionic state. Therefore the lowest and highest lying triplet states, which are almost completely depopulated if the transition is open for a long time, have a much higher probability to be occupied and correspondingly the pseudospin oscillations occur with a much higher amplitude, see Fig. 5.3(d) and Fig. 5.2(d). The oscillations of the spin however are still very small, see Fig. 5.2(c), but we can already conclude that $\langle S_y \rangle$ seems to be coupled to $\langle \tau_x \rangle$ by the spin orbit interaction. Furthermore we see beatings in the pseudospin oscillations which can be analysed by means of Fast Fourier Transform. We find that the faster frequency is generated by coherences between $|\mathbf{T}^{-1}_+ - \mathbf{T}^{+1}_-\rangle$ and $|\mathbf{T}^{+1}_+ + \mathbf{T}^{-1}_-\rangle$ and the slower one by the ones between $|\mathbf{T}^{-1}_+ + \mathbf{T}^{+1}_-\rangle$ and $|\mathbf{T}^{+1}_+ - \mathbf{T}^{-1}_-\rangle$. We show the Fourier spectrum in Fig. 5.4 with a schematic depiction of the triplet states ordered by their energies in the inset. The red and green arrows show which states are responsible for which frequency. We report in Fig. 5.5(a) the transferred charge per pump probe cycle. We vary the time delay between the end of the pump pulse and the beginning of the probe pulse between $t_{\mathrm{del}} = 0$ps and $t_{\mathrm{del}} = 50$ps. In Fig. 5.5(b) we report the

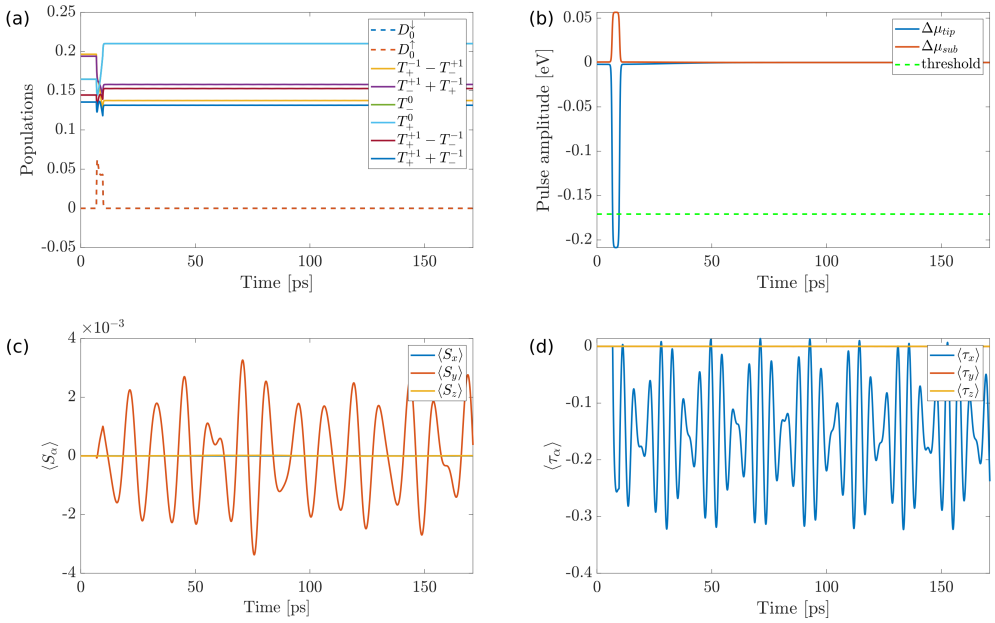

Figure 5.3.: Simulation of the full system driven by a laser pulse of width 3ps. We report in (a) the populations of the system, (b) the bias change in each lead due to the laser pulse, (c) the expectation value of the spin with $\langle S_x \rangle = \langle S_z \rangle = 0$ and (d) the expectation value of the pseudospin with $\langle \tau_y \rangle = \langle \tau_z \rangle = 0$.

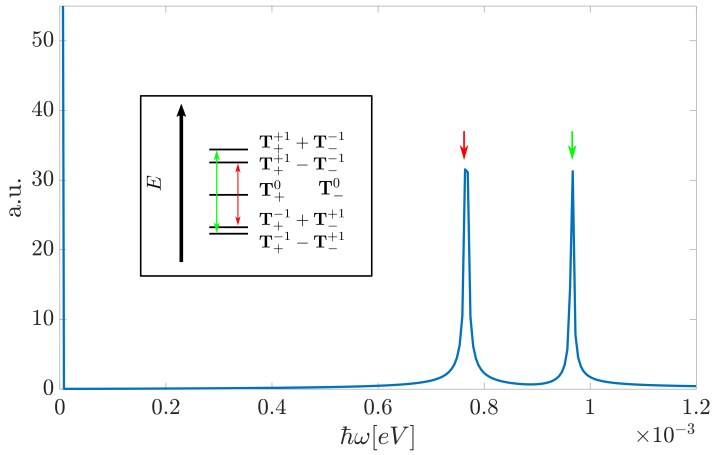

Figure 5.4.: FFT analysis of the oscillations in τ_x. We see two distinct frequencies. In the inset we report a schematic depiction of the triplet states ordered by their energy. The arrows denote which states are responsible for which frequency.

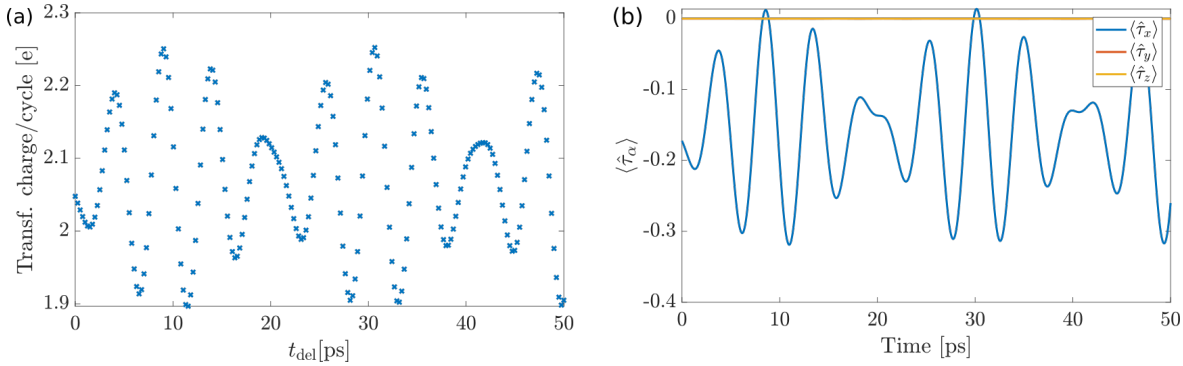

Figure 5.5.: The pump probe scheme to read out the orbital dynamics in the full system. We see in (a) the transferred charge per pump probe cycle given in electrons. In (b) the corresponding dynamics are reported where we have shifted the time axis so that the time corresponds to the delay time between the two pulses.

corresponding pseudospin dynamics. In fact Fig. 5.5(b) is a cut of Fig. 5.3(d) where we have relabeled the x-axis so that $t = 0$ps corresponds to the state of the system at $t_{\text{del}} = 0$ps. Remember that from the model evaluated in Chapter 4 we know that the blocking state and thus the minimal charge transferred per pump probe cycle is reached if $\tau_x = -0.5$, $\tau_y = 0$ and $\tau_z = 0$. By comparison of Fig. 5.5(a) and Fig. 5.5(b) we see a striking resemblance of the pseudospin dynamics and the calculated transferred charge. We also see that the closer the system gets to the blocking state the smaller the transferred charge becomes. Similarly to the model this is a pseudospin valve effect with the difference that in the model we had a precession around the axis perpendicular to the molecule and in this case only the τ_x component of the pseudospin is oscillating. A way of enhancing the dynamics of the spin is to introduce spin polarization in the leads. We will do this in the next section.

5.3. Effects of a spin polarized tip

In this section we will explore the effects of a spin polarized tip. We will consider a spin polarization described by the polarization vector

$$\mathbf{P}^{\sigma}_{\text{tip}} = \begin{pmatrix} 0 \\ 0 \\ 1 \end{pmatrix}. \tag{5.8}$$

This leads to the effect that only electrons with spin up will be able to tunnel from the molecule to the tip. First we will see what happens in the system if we open the transition from the anionic to the neutral state for a long time and then in a second step shorten the pulse time and thus the opening of the transition.

5.3.1. Long pulse to drive the system

We report the numerical evolution of the system driven by a long pulse and a spin polarized tip, as introduced in Eq. (5.8), in Fig. 5.6. Fig. 5.6(a) shows the populations of the system. The spin polarization leads to a complete breaking of the superselection rules and thus the triplet states with $S_z \neq 0$ have a much higher probability to be populated than in Fig. 5.2(a). In Fig. 5.6(b) we see the change of the chemical potential due to the laser pulse. The transition is open for 30ps. In Fig. 5.6(c) one can see that during the time interval in which the transition is open the expectation value for the z-component of the molecule approaches $S_z = \downarrow$. This can be understood by the fact that only electrons with $S_z = \uparrow$ are allowed to tunnel from the molecule to the tip and thus the expectation value of the z-component will be lowered by 0.5. Furthermore, we can observe oscillations in all three spin components in Fig. 5.6(c). However, the oscillations in S_x and S_y have such a small amplitude that we will not investigate them in detail and from now on if we talk about spin oscillations we will refer to the S_z-component.
Also in the spin dynamics beatings appear, but if we compare them to the pseudo spin dynamics, see Fig. 5.6(d), it is obvious that the contributing frequencies are much smaller. Taking a look at Fig. 5.6(d) we see that in contrast to Fig. 5.2(d) oscillations are also present in the y- and z-component of the pseudospin. The oscillation of the y-component is a beating of two fast frequencies whereas the z-component one of slow frequencies. We can conclude that these oscillations are due to spin orbit coupling since the only thing that changed between Fig. 5.2 and Fig. 5.6 is that the system is prepared in a state with a nonzero expectation value of the S_z-component.

5.3.2. Short pulse to drive the system

In this section we investigate what happens if we shorten the time interval in which the transition from the anionic to the neutral state is open from 30ps to 3ps. We see in Fig. 5.7(a) the populations of the system. The difference between the probabilities of different states being occupied is smaller compared to their difference observed for a longer pulse, see Fig. 5.6(b). This is consistent with the observations we made for the system without a spin polarized tip, see Sec. 5.2. In Fig. 5.7(b) we report again the bias change of the system. We find for the spin, see Fig. 5.7(c), the same behaviour as for the driving with a longer laser pulse. In analogy to Sec. 5.2 we find that the pseudospin oscillations have a larger amplitude compared to driving with a long pulse.

In Fig. 5.8 we report the simulation of pump probe schemes in the system with a spin polarized tip. We vary the delay time between the two pulses from $t_{\text{del}} = 30$ps to $t_{\text{del}} = 217$ps to show the charge transfer during one period of the spin oscillation. The corresponding charge transfer per pump probe cycle is shown in Fig. 5.8(a). Figs. 5.8(b) and 5.8(c) show the corresponding spin and pseudospin dynamics respectively. We have

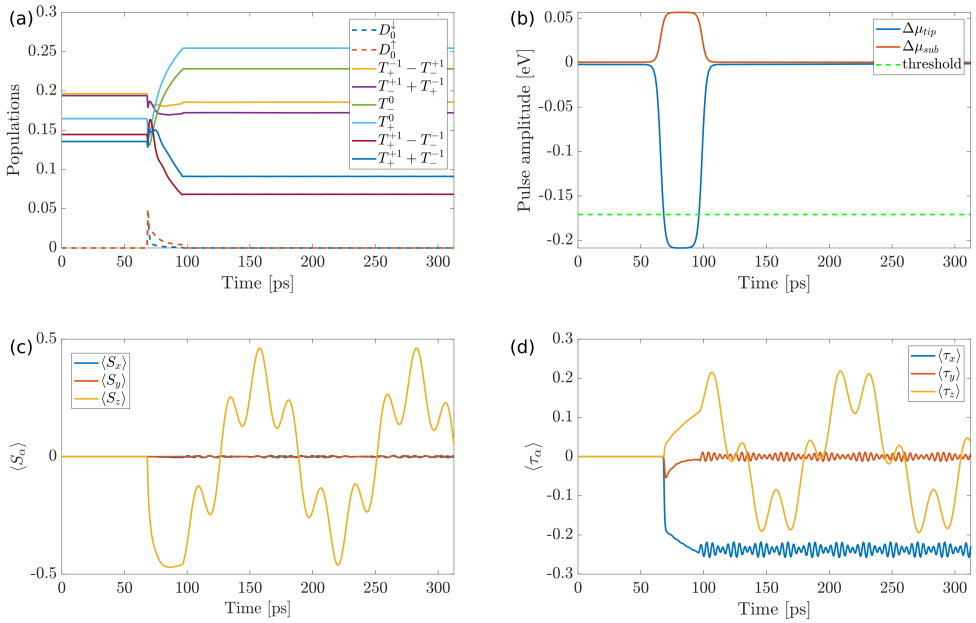

Figure 5.6.: Simulation of the full system driven by a laser pulse of width 30ps. The tip is polarized with a value of $S_z^{\text{tip}} = \uparrow$. We report in (a) the populations of the system, (b) the bias change in each lead due to the laser pulse, (c) the expectation value of the spin and (d) the expectation value of the pseudospin.

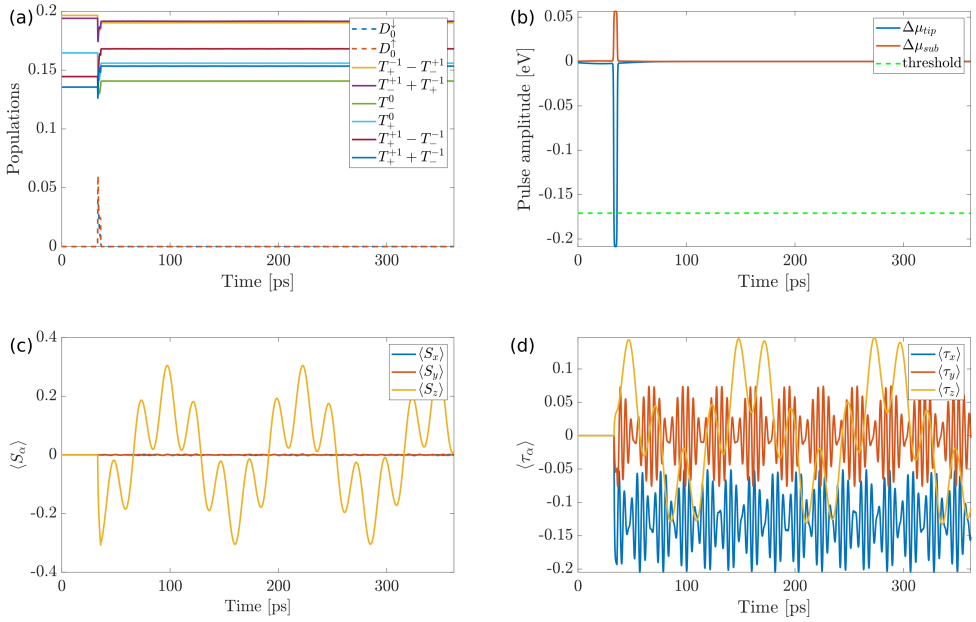

Figure 5.7.: Simulation of the full system driven with a laser pulse of width 3ps. The tip is polarized with a value of $S_z^{\text{tip}} = \uparrow$. We report in (a) the populations of the system, (b) the bias change in each lead due to the laser pulse, (c) the expectation value of the spin and (d) the expectation value of the pseudospin.

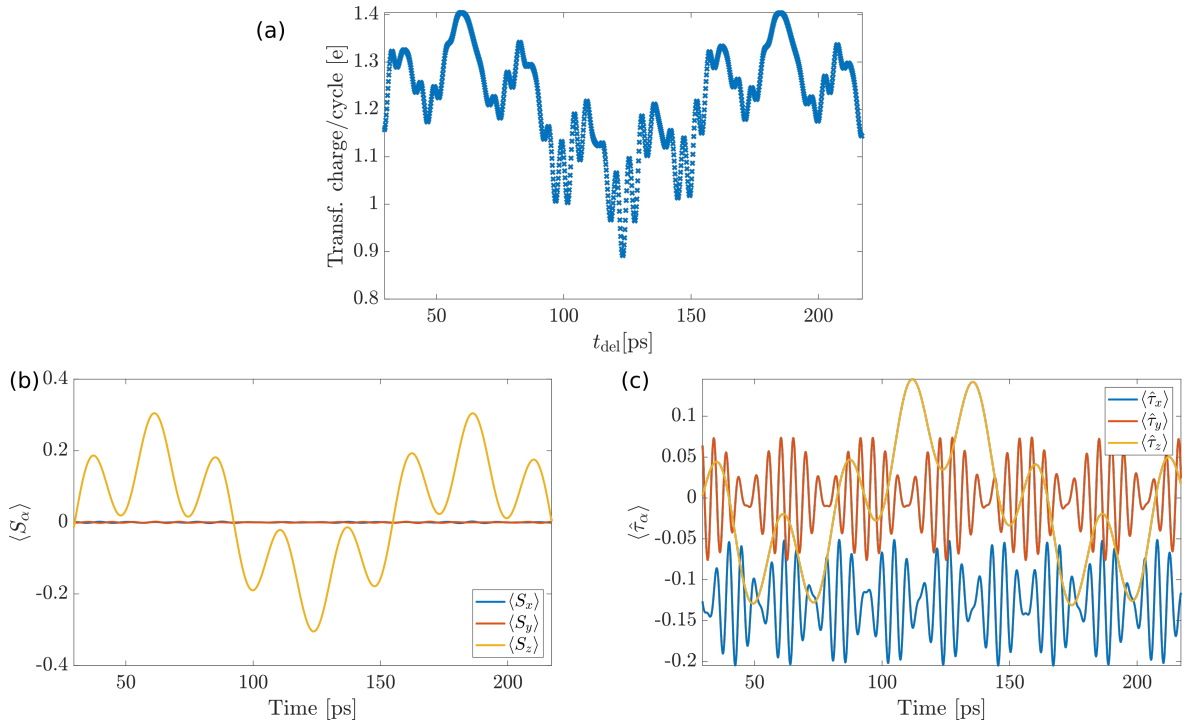

Figure 5.8.: The pump probe scheme to read out the spin orbit induced dynamics in the full system with a spin polarized tip. We report (a) the transferred charge per pump probe cycle given in electrons, (b) the corresponding spin dynamics and (c) the pseudospin dynamics. We have relabeled the time axis in (b) and (c) so that it corresponds to the delay time between the two pulses.

relabeled the time axis so that the time on which we report the dynamics correspond to delay times between the two pulses. We can see in Fig. 5.8 a spin valve effect on which a pseudospin valve effect is superimposed. The better the alignment between (pseudo) spin and the corresponding (pseudo) spin polarization of the tip is the larger is the transferred charge per pump probe cycle. This is qualitatively the same effect we observed in our simplified model in Chap. 4.

We will now conclude our numerical investigation of the system. We have seen in this chapter that it is possible to drive spin orbit dynamics in CuPc in an THz-STM setup. We saw in this chapter that the spin and pseudospin show an oscillatory coherent dynamics which has qualitatively the same effect on the transferred charge per pump probe cycle as in the simplified model. In contrast to our model the oscillatory dynamics in this chapter do not only consist of one frequency but show beatings. Furthermore, one can conclude that interactions between the spin and pseudospin dynamics are present. We found in the model that the free pseudospin dynamics are described by

$$\dot{\boldsymbol{\tau}} = \omega(\mathbf{n}_{\mathrm{mol}} \times \boldsymbol{\tau}). \tag{5.9}$$

Due to the interactions such a simple description is not possible for the full model anymore. In the next chapter we take the correlators between spin and pseudospin into account to get a description of the free dynamics of our triplet states.

6. Free evolution of the triplet states

In this chapter we investigate the dynamics of the triplet states with an analytical approach. We focus on the free evolution of those states, i.e. $V_{\text{bias}} = 0$. We start with a expansion of the reduced density matrix in its irreducible components and follow for this purpose Chap. 4 of Ref. [36]. We already saw in Sec. 4.4 that we could rewrite the one particle sub block of the density matrix in terms of its populations and components of the pseudospin operator. This is a special case of the expansion of the density matrix in its irreducible components for (pseudo) spin $1/2$ particles. We will now show the general form of this expansion which then can also be used to describe our triplet states which have a pseudospin of $1/2$ but also a spin of 1.

6.1. Irreducible components of the density matrix

For simplicity, we drop the hat notation for operators and will always indicate their expectation values by bra-ket notation. If one considers an ensemble of particles which are characterized by angular momentum values of J one can write the density matrix of this ensemble as

$$\rho = \sum_{JKQ} \langle T(J)^{\dagger}_{KQ} \rangle T(J)_{KQ}. \tag{6.1}$$

Here, K denotes the total angular momentum and Q its z-component. $T(J)_{KQ}$ are the tensor operators for a system with angular momentum J. The number of possible tensor operators for an ensemble is restricted by the condition

$$-K \leq Q \leq K. \tag{6.2}$$

The tensor operator with rank $K = 0$ is a scalar operator and is proportional to the unity matrix

$$T(J)_{00} = \frac{1}{\sqrt{2J+1}} \mathbb{1}. \tag{6.3}$$

To describe the tensor operators of rank $K = 1$ we introduce the angular momentum vector

$$\mathbf{J} = \begin{pmatrix} J_x \\ J_y \\ J_z \end{pmatrix}, \tag{6.4}$$

from which we can deduce the spherical vector components as

$$J_\pm = \mp\frac{1}{\sqrt{2}}(J_x \pm \mathrm{i}J_y) \quad \text{and} \quad J_0 = J_z, \tag{6.5}$$

with $J_\pm$ being the raising/lowering operator. The tensor operators of rank $K = 1$ are related to the spherical vector components via

$$T(J)_{1Q} = \sqrt{\frac{3}{(2J+1)(J+1)J}}\; J_Q. \tag{6.6}$$

In a similar fashion the tensor operators of rank $K = 2$, also called quadrupole moments, are related to quadratic combinations of the angular momentum vector components J_x, J_y and J_z by

$$\begin{aligned} T(J)_{20} &= \frac{N_2}{\sqrt{6}}(3J_z^2 - \mathbf{J}^2) \\ T(J)_{2\pm1} &= \mp\frac{N_2}{2}\left[(J_xJ_z + J_xJ_z) \pm \mathrm{i}(J_yJ_z + J_zJ_y)\right] \\ T(J)_{2\pm2} &= \frac{N_2}{2}\left[J_x^2 - J_y^2 \pm \mathrm{i}(J_xJ_y + J_yJ_x)\right], \end{aligned} \tag{6.7}$$

with

$$N_2 = \sqrt{\frac{30}{(2J+3)(2J+1)J(2J-1)(J+1)}}. \tag{6.8}$$

The triplet states we are interested in are a combination of a pseudospin part with $J = 1/2$ and a spin part with $J = 1$. Therefore, we will in the next section take a look on how to construct a density matrix for particles with $J = 1/2$ and $J = 1$ separately before combining everything together.

6.2. Spin and pseudospin tensors

In this section we will give expressions for the density matrix in terms of its irreducible components for particles with $J = 1/2$ and $J = 1$. This is done because we need to describe the pseudospin part of the triplet states which has angular momentum $J = 1/2$ and the spin part with $J = 1$. We will start with the $J = 1/2$ case.

6.2.1. (Pseudo) Spin tensors for (pseudo) spin 1/2 particles

Eq. (6.1) implies that for spin 1/2 particles the only tensors we need to take into account are of rank $K = 0$ and $K = 1$. We thus find for the monopole term given by Eq. (6.3)

$$T(1/2)_{00} = \frac{1}{\sqrt{2}}\mathbb{1}. \tag{6.9}$$

The tensors of rank $K = 1$ are connected to the corresponding spherical spin operators by Eq. (6.6). For a system with $J = 1/2$ we can identify the angular momentum operators as

$$J_i = \frac{1}{2}\sigma_i, \quad i = x, y, z, \tag{6.10}$$

with the Pauli matrices σ_i. The tensor operators of rank $K = 1$ are

$$T(1/2)_{1Q} = \sqrt{2}J_Q \tag{6.11}$$

and their expectation values are

$$\langle T(1/2)^\dagger_{1Q}\rangle = \sqrt{2}\,\langle J^\dagger_Q\rangle\,, \tag{6.12}$$

where J_Q is given by Eq. (6.5). Plugging the results in Eq. (6.1) we find for the density matrix of spin 1/2 particles

$$\begin{aligned}\rho^{1/2} &= \sum_{KQ}\langle T(1/2)^\dagger_{KQ}\rangle\, T(1/2)_{KQ}\\ &= \frac{1}{2}\mathbb{1} + \sum_{Q}\langle T(1/2)^\dagger_{1Q}\rangle\, T(1/2)_{1Q}\\ &= \frac{1}{2}\mathbb{1} + \frac{1}{2}\,\mathrm{Tr}\left\{\rho\sigma_x\right\}\sigma_x + \frac{1}{2}\,\mathrm{Tr}\left\{\rho\sigma_y\right\}\sigma_y + \frac{1}{2}\,\mathrm{Tr}\left\{\rho\sigma_z\right\}\sigma_z.\end{aligned} \tag{6.13}$$

This is the expansion we used in Eq. (4.25) to describe the one particle sub block of our density matrix. Now we know how to expand the density matrix for spin 1/2 particles in terms of its irreducible components. We will in the next section do this for spin 1 particles.

6.2.2. (Pseudo) Spin tensors for (pseudo) spin 1 particles

The first thing we need on our way to describe the expansion of the density matrix for spin 1 particles are the definitions of the spin operators describing them. They are given by

$$S_x = \frac{1}{\sqrt{2}}\begin{pmatrix} 0 & 1 & 0 \\ 1 & 0 & 1 \\ 0 & 1 & 0 \end{pmatrix}, \quad S_y = \frac{1}{\sqrt{2}}\begin{pmatrix} 0 & -\mathrm{i} & 0 \\ \mathrm{i} & 0 & -\mathrm{i} \\ 0 & \mathrm{i} & 0 \end{pmatrix}, \quad S_z = \begin{pmatrix} 1 & 0 & 0 \\ 0 & 0 & 0 \\ 0 & 0 & -1 \end{pmatrix}. \tag{6.14}$$

The monopole tensor is given by

$$T(1)_{00} = \frac{1}{\sqrt{3}}\mathbb{1}. \tag{6.15}$$

By setting $J_i = S_i$ we find for the tensors of rank $K = 1$

$$\langle T(1)^\dagger_{1Q} \rangle = \frac{\langle J_Q \rangle}{\sqrt{2}}, \tag{6.16}$$

where J_Q is again given by Eq. (6.5). The quadratic combinations of the angular momentum operators can be constructed according to Eq. (6.7) with $N_2 = 1$. Therefore, we can conclude that the density matrix for spin 1 particles has the following form

$$\rho^1 = \frac{1}{3}\mathbb{1} + \sum_Q \langle T(1)^\dagger_{1Q} \rangle \, T(1)_{1Q} + \sum_Q \langle T(1)^\dagger_{2Q} \rangle \, T(1)_{2Q}. \tag{6.17}$$

6.3. Time evolution of the density matrix

We will now derive analytic expressions for the spin and pseudospin dynamics which were numerically explored in Chap. 5. We use the effective Hamiltonian describing the triplet states given in Eq. (2.74). It reads

$$\hat{H}^{\mathrm{eff}} = \alpha_5 \mathbb{1}_6 + \begin{pmatrix} \alpha_1/2 & 0 & 0 & 0 & 0 & \alpha_2 \\ 0 & \alpha_4 & 0 & 0 & 0 & 0 \\ 0 & 0 & -\alpha_1/2 & \alpha_3 & 0 & 0 \\ 0 & 0 & \alpha_3 & -\alpha_1/2 & 0 & 0 \\ 0 & 0 & 0 & 0 & \alpha_4 & 0 \\ \alpha_2 & 0 & 0 & 0 & 0 & \alpha_1/2 \end{pmatrix}. \tag{6.18}$$

It has the following eigenvalues

$$\begin{aligned} E_1 &= \alpha_4 + \alpha_5, & E_2 &= \alpha_4 + \alpha_5, & E_3 &= \frac{1}{2}(\alpha_1 - 2\alpha_2 + 2\alpha_5), \\ E_4 &= \frac{1}{2}(\alpha_1 + 2\alpha_2 + 2\alpha_5), & E_5 &= \frac{1}{2}(-\alpha_1 - 2\alpha_3 + 2\alpha_5), & E_6 &= \frac{1}{2}(-\alpha_1 + 2\alpha_3 + 2\alpha_5). \end{aligned} \tag{6.19}$$

The time evolution of the density matrix is given by the Liouville - von Neumann equation

$$\dot{\rho}(t) = -\frac{\mathrm{i}}{\hbar}\left(\hat{H}^{\mathrm{eff}}\rho(t) - \rho(t)\hat{H}^{\mathrm{eff}}\right). \tag{6.20}$$

Let $\mathbf{v}_a$ be the eigenvector of the effective Hamiltonian corresponding to the eigenvalue E_a. We define a transformation matrix as

$$M \coloneqq [\mathbf{v}_1, \ldots, \mathbf{v}_6]\,. \tag{6.21}$$

We transform ρ into the eigenbasis of $\hat{H}^{\mathrm{eff}}$ by

$$\rho_H = M\rho M^\dagger. \tag{6.22}$$

In this basis the Liouville - von Neumann equation can be solved by

$$(\rho_H(t))_{ab} = \sum_{a,b=1}^{6} \mathrm{e}^{-\frac{\mathrm{i}}{\hbar}(E_a - E_b)t}\,(\rho_H(0))_{ab}\,. \tag{6.23}$$

Now, that we know the time evolution of the density matrix describing our triplet states we will investigate how to obtain equations for the dynamics of the spin, pseudospin and their correlators.

6.4. Dynamics of the spin and pseudospin

Equipped with the knowledge about the expansion of density matrices for (pseudo) spin $1/2$ and (pseudo) spin 1 particles from Sec. 6.2 we will construct a basis in which we can expand the density matrix for the triplet states. Our triplet states have a spin angular momentum value of $J_S = 1$ and a pseudospin angular momentum value of $J_P = 1/2$. Therefore, a basis which allows us to expand the density matrix of the triplet states has to incorporate both of these spaces.
We use for the pseudospin operators the notation

$$\tau_x = \frac{1}{2}\sigma_x, \quad \tau_y = \frac{1}{2}\sigma_y, \quad \tau_z = \frac{1}{2}\sigma_z. \tag{6.24}$$

We define a basis for the $J_P = 1/2$ space, by using the spherical components of the pseudospin operators, as

$$\mathcal{B}^c_{1/2} = \left\{ \frac{1}{\sqrt{2}}\mathbb{1}_2, \sqrt{2}\tau_z, -(\tau_x + \mathrm{i}\tau_y), \tau_x - \mathrm{i}\tau_y \right\}, \tag{6.25}$$

where the c stands for complex since we use the spherical components of the pseudospin operators, which contain imaginary parts, to define the basis. For the spin operators we use the definition given in Eq. (6.14) and define a basis for the $J_S = 1$ space, again by using the spherical components, by

$$\begin{aligned} \mathcal{B}^c_1 = \Bigg\{ & \frac{1}{\sqrt{3}}\mathbb{1}_3, \frac{1}{\sqrt{2}}S_z, \frac{-1}{2}(S_x + \mathrm{i}S_y), \frac{1}{2}(S_x - \mathrm{i}S_y), \frac{1}{\sqrt{6}}(2S_z^2 - S_x^2 - S_y^2), \\ & \frac{-1}{2}\Big[S_xS_z + S_zS_x + \mathrm{i}(S_yS_z + S_zS_y)\Big], \frac{1}{2}\Big[S_xS_z + S_zS_x - \mathrm{i}(S_yS_z + S_zS_y)\Big], \\ & \frac{1}{2}\Big[S_xS_x - S_yS_y + \mathrm{i}(S_xS_y + S_yS_x)\Big], \frac{1}{2}\Big[S_xS_x - S_yS_y - \mathrm{i}(S_xS_y + S_yS_x)\Big] \Bigg\}, \end{aligned} \tag{6.26}$$

where again the c stands for complex with the same reason as for the pseudospin. A basis in which we can expand the density matrix describing the triplet states is therefore

$$\mathcal{B}^c = \mathcal{B}^c_{1/2} \otimes \mathcal{B}^c_1, \tag{6.27}$$

since it incorporates the spaces of $J_P = 1/2$ and $J_S = 1$. By identifying the tensor operators introduced in Sec. 6.1 we can conclude that the density matrix is then determined by the correlators

$$\langle T(1/2)_{KQ} T(1)_{K'Q'} \rangle \tag{6.28}$$

because they are the expansion coefficients of ρ in the basis $\mathcal{B}^c$.
However, it is also possible to define a basis directly by the angular momentum operators. For the pseudospin $1/2$ part we can define a basis, using directly the angular momentum operators, by

$$\mathcal{B}^r_{1/2} = \{\mathbb{1}_2, \tau_z, \tau_x, \tau_y\}, \tag{6.29}$$

where the r stands for real since in this basis no more imaginary parts are present. For the spin 1 part we need the angular momentum operators and additional quadratic combinations of them. We can take the real parts of the basis $\mathcal{B}^c_1$ for the quadratic combinations and then define the real basis for the spin 1 part by

$$\begin{aligned} \mathcal{B}^r_1 = \Big\{ & \mathbb{1}_3, S_z, S_x, S_y, 2S_z^2 - S_x^2 - S_y^2, S_xS_z + S_zS_x, \\ & S_yS_z + S_zS_y, S_x^2 - S_y^2, S_xS_y + S_yS_x \Big\}. \end{aligned} \tag{6.30}$$

In analogy to Eq. (6.27) we get the complete basis of the density matrix by

$$\mathcal{B}^r = \mathcal{B}^r_{1/2} \otimes \mathcal{B}^r_1. \tag{6.31}$$

By introducing the notations

$$\begin{aligned} P &= \mathbb{1}_6, \\ S_{3z^2} &= 2S_z^2 - S_x^2 - S_y^2, \\ S_{xz} &= S_xS_z + S_zS_x, \\ S_{yz} &= S_yS_z + S_zS_z, \\ S_{x^2y^2} &= S_x^2 - S_y^2, \\ S_{xy} &= S_xS_y + S_yS_x, \end{aligned} \tag{6.32}$$

we can write Eq (6.31) in the explicit form

$$\mathcal{B}^r = \begin{pmatrix} P & S_z & S_x & S_y & S_{3z^2} & S_{xz} & S_{yz} & S_{x^2y^2} & S_{xy} \\ \tau_z & \tau_zS_z & \tau_zS_x & \tau_zS_y & \tau_zS_{3z^2} & \tau_zS_{xz} & \tau_zS_{yz} & \tau_zS_{x^2y^2} & \tau_zS_{xy} \\ \tau_x & \tau_xS_z & \tau_xS_x & \tau_xS_y & \tau_xS_{3z^2} & \tau_xS_{xz} & \tau_xS_{yz} & \tau_xS_{x^2y^2} & \tau_xS_{xy} \\ \tau_y & \tau_yS_z & \tau_yS_x & \tau_yS_y & \tau_yS_{3z^2} & \tau_yS_{xz} & \tau_yS_{yz} & \tau_yS_{x^2y^2} & \tau_yS_{xy} \end{pmatrix}. \tag{6.33}$$

The components of the density matrix in this basis are now the expectation values of the operators comprising the basis $\mathcal{B}^r$. It holds for an arbitrary operator O that

$$\langle O(t)\rangle = \mathrm{Tr}\left\{O\rho(t)\right\}. \tag{6.34}$$

Therefore we can obtain all expectation values for our pseudospin τ_i operators, spin S_i operators, quadrupole moments for the spin and their correlators in this way. Exemplarily, we give the solution for τ_x here

$$\begin{aligned} \langle\tau_x(t)\rangle =& \frac{1}{12}\Big\{4\Big[\langle\tau_x\rangle - \langle\tau_xS_{3z^2}\rangle\Big] \\ &+ \Big[3\langle S_{x^2y^2}\rangle + 4\langle\tau_x\rangle + 2\langle\tau_xS_{3z^2}\rangle\Big]\cos\Big[(\alpha_1+\alpha_2-\alpha_3)\,t\Big] \\ &+ \Big[-3\langle S_{x^2y^2}\rangle + 4\langle\tau_x\rangle + 2\langle\tau_xS_{3z^2}\rangle\Big]\cos\Big[(\alpha_1-\alpha_2+\alpha_3)\,t\Big] \\ &- 6\Big[\langle\tau_yS_z\rangle + \langle\tau_zS_{xy}\rangle\Big]\sin\Big[(\alpha_1+\alpha_2-\alpha_3)t\Big] \\ &- 6\Big[\langle\tau_yS_z\rangle - \langle\tau_zS_{xy}\rangle\Big]\sin\Big[(\alpha_1-\alpha_2+\alpha_3)t\Big]\Big\} \end{aligned} \tag{6.35}$$

where all expectation values on the right hand side have to be calculated at t_0. We show in Fig. 6.1 a numerical simulation of the system, with the same parameters as in Sec. 5.3.2. We superimpose in Fig. 6.1(c) and Fig. 6.1(d) the analytical solutions obtained for the spin and pseudospin expectation values. Therefore we choose an initial time t_0 after the transition from the anionic to the neutral state is closed and use $\rho(t_0)$ to calculate all the correlators appearing in Eq. (6.35) and the corresponding equations for different expectation values. We see in Fig. 6.1 that our analytical solutions for the free evolution match the numerical ones perfectly. Thus, we are able to describe the free evolution of our triplet states with respect to arbitrary initial conditions. We

have shown that we understand the dependence of the spin and pseudospin dynamics on their correlators in a quantitative way.

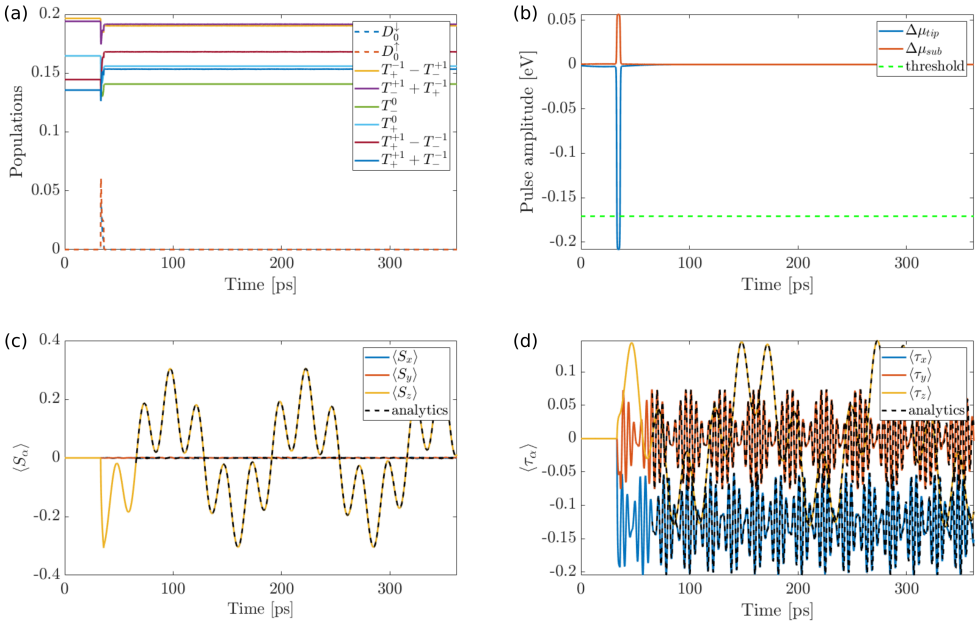

Figure 6.1.: Simulation of the full system driven with a laser pulse of width around 3ps. The tip is polarized with a value of $S_z^{\text{tip}} = \uparrow$. We report in (a) the populations of the system, (b) the bias change in each lead due to the laser pulse, (c) the expectation value of the spin and (d) the expectation value of the pseudospin. In (c) and (d) the analytical solutions for the free evolutions are superimposed on the numerical results.

7. Conclusion

In this thesis we investigated spin-orbit induced dynamics in a CuPc molecule. We considered a single molecule junction consisting of a CuPc molecule in a THz-STM setup. We first derived a many-body model able to describe a CuPc molecule. By choosing the molecular orbital basis for our description we were able to determine the subset of orbitals needed to describe transport at low energies. Symmetry arguments enabled us to reduce the number of Coulomb integrals needed to obtain a complete description of the electronic interactions in the system. Then, we introduced the spin-orbit coupling into our model by evaluating a general spin-orbit interaction operator only on the copper atom and projecting it on the set of frontier orbitals. By analysing the spectrum of this model we found the states relevant for transport at low bias voltages which we later used in our numerical and analytical calculations. To describe transport through our junction we showed the derivation of a general transport formalism for the reduced density matrix where we included the geometry of an STM and the effects of coupling laser pulses to the system.
Then, we showed that already in a simplified model of the molecule with two quasi degenerate orbitals we find pseudospin precession. We investigated this numerically and were able to describe the precession completely within our analytical transport formalism. The connection between the pseudospin precession and transferred charge per pump probe cycle was shown numerically and analytically.
In the full model we discovered again pseudospin oscillations but this time coupled to spin dynamics. We saw in our numerical simulations that the shorter the time interval, in which the transition from the anionic to the neutral state is possible, the more pronounced the pseudospin dynamics of our system become. We found that in order to enlarge the spin oscillations in our system we need to spin polarize the tip of the STM. The reason this increases the amplitude of the spin oscillation is the complete breaking of superselection rules.
Simulations of pump probe schemes in the full model show a pseudospin valve effect when the tip is unpolarized and a combined spin and pseudospin valve effect if a spin polarization is present in the tip. This might provide a way of obtaining information about the spin-orbit induced dynamics via electronic measurements.
Lastly we investigated the free evolution of the anionic triplet states and showed that we can describe the dynamics of the spin and pseudospin analytically. By decomposing the density matrix in its irreducible components we found the dependence of the spin and pseudospin dynamics on the correlators between the spin operators, pseudospin operators and the quadrupole moments for the spin. Even though, considerable progress was made in describing a single CuPc molecule in a THz-STM junction there still re-

main some open questions. The first question is if it is possible to derive an analytical expression for the charge transfer in a pump probe cycle depending on the spin and pseudospin dynamics, analogous to the one derived for the simplified model. Also a better understanding of the preparation done by the pump pulse would be desirable. As explored in our spectrum analysis of CuPc there are degenerate states present and therefore one should investigate if the Jahn-Teller effect [50] plays a role in our CuPc-THz-STM junction. Since our transport formalism is quite general it should in principal be extendable to arbitrary molecules as long as one is able to find a satisfying many-body model for them. So there are a lot of possible candidate molecules to be investigated in the future.

A. Appendix

A.1. Effect of the split pair hopping on the low energy spectrum

The split pair hopping term $\tilde{J}^P_{H+-}$ creates admixtures in the low energy spectrum of the molecular Hamiltonian (2.34). We write

$$\hat{H}^P_{H+-} = \frac{1}{2} \sum_{\tau,\tau'=\pm} \sum_{\sigma} \tilde{J}^P_{H\tau\tau'} \hat{d}^\dagger_{\mathrm{L}\tau\sigma} \hat{d}^\dagger_{\mathrm{L}\tau'\bar{\sigma}} \hat{d}_{\mathrm{H}\sigma} \hat{d}_{\mathrm{H}\bar{\sigma}}, \tag{A.1}$$

to explore the effect of the split pair hopping on the low energy spectrum. On the doubly degenerate neutral groundstate the split pair hopping has the following effect

$$\begin{aligned} \hat{H}^P_{H+-} |D^\uparrow_0\rangle &= \frac{1}{2} \sum_{\tau,\tau'=\pm} \sum_{\sigma} \hat{d}^\dagger_{\mathrm{S}\uparrow} \hat{d}^\dagger_{\mathrm{L}\tau\sigma} \hat{d}^\dagger_{\mathrm{L}\tau'\bar{\sigma}} |0\rangle, \\ \hat{H}^P_{H+-} |D^\downarrow_0\rangle &= \frac{1}{2} \sum_{\tau,\tau'=\pm} \sum_{\sigma} \hat{d}^\dagger_{\mathrm{S}\downarrow} \hat{d}^\dagger_{\mathrm{L}\tau\sigma} \hat{d}^\dagger_{\mathrm{L}\tau'\bar{\sigma}} |0\rangle. \end{aligned} \tag{A.2}$$

Therefore, the split pair hopping introduces small admixtures into the neutral groundstates. These admixtures are the same for both neutral ground states. However, they are very small and only introduce a constant shift, thus we neglected them in our spectrum analysis.
The effect on the anionic low energy states is

$$\begin{aligned} \hat{H}^P_{H+-} |\mathbf{S}_\tau\rangle &= \frac{1}{2} \frac{1}{\sqrt{2}} \left(\hat{d}^\dagger_{\mathrm{S}\uparrow} \hat{d}^\dagger_{\mathrm{L}\tau\downarrow} \hat{d}^\dagger_{\mathrm{L}\tau\uparrow} \hat{d}^\dagger_{\mathrm{L}\bar{\tau}\downarrow} - \hat{d}^\dagger_{\mathrm{S}\downarrow} \hat{d}^\dagger_{\mathrm{L}\tau\uparrow} \hat{d}^\dagger_{\mathrm{L}\tau\downarrow} \hat{d}^\dagger_{\mathrm{L}\bar{\tau}\uparrow} \right) |0\rangle \\ \hat{H}^P_{H+-} |\mathbf{T}^{+1}_\tau\rangle &= \frac{1}{2} \hat{d}^\dagger_{\mathrm{S}\uparrow} \hat{d}^\dagger_{\mathrm{L}\tau\uparrow} \hat{d}^\dagger_{\mathrm{L}\tau\downarrow} \hat{d}^\dagger_{\mathrm{L}\bar{\tau}\uparrow} |0\rangle \\ \hat{H}^P_{H+-} |\mathbf{T}^{0}_\tau\rangle &= \frac{1}{2} \frac{1}{\sqrt{2}} \left(\hat{d}^\dagger_{\mathrm{S}\uparrow} \hat{d}^\dagger_{\mathrm{L}\tau\downarrow} \hat{d}^\dagger_{\mathrm{L}\tau\uparrow} \hat{d}^\dagger_{\mathrm{L}\bar{\tau}\downarrow} + \hat{d}^\dagger_{\mathrm{S}\downarrow} \hat{d}^\dagger_{\mathrm{L}\tau\uparrow} \hat{d}^\dagger_{\mathrm{L}\tau\downarrow} \hat{d}^\dagger_{\mathrm{L}\bar{\tau}\uparrow} \right) |0\rangle \\ \hat{H}^P_{H+-} |\mathbf{T}^{-1}_\tau\rangle &= \frac{1}{2} \hat{d}^\dagger_{\mathrm{S}\downarrow} \hat{d}^\dagger_{\mathrm{L}\tau\downarrow} \hat{d}^\dagger_{\mathrm{L}\tau\uparrow} \hat{d}^\dagger_{\mathrm{L}\bar{\tau}\downarrow} |0\rangle. \end{aligned} \tag{A.3}$$

Similarly, to the effect on the neutral ground states the split pair hopping introduces small admixtures into the anionic low energy states. However, they are all of the same type with the SOMO occupied by one electron and three electrons in the LUMOs.

Again, this only introduces a small constant energy shift of all states and we therefore neglected the effect in our spectrum analysis.

A.2. Reformulation of the two orbital model equations into populations and pseudospin

We will show how to reformulate eqs. (4.21) - (4.23) into equations for the populations P_0, P_1, P_2 and the vector of pseudospin expectation values $\boldsymbol{\tau}$. By using the approximations

$$\begin{aligned} f_\eta(\hat{H}_1) &\approx \bar{f}_\eta(\hat{H}_1), \\ \mathrm{p}_\eta(\hat{H}_1) &\approx \bar{\mathrm{p}}_\eta(\hat{H}_1), \end{aligned} \tag{A.4}$$

and using the notation

$$H_{10} \equiv \hat{H}_1 - E_0, \quad H_{21} \equiv E_2 - \hat{H}_1 \tag{A.5}$$

we can reformulate eqs. (4.21) - (4.23). We find for Eq. (4.21)

$$\begin{aligned} \dot{\rho}^0 = &- \left[2\bar{\Gamma}^{\mathrm{sub}} \bar{f}^+_{\mathrm{sub}}(H_{10}) + 2\bar{\Gamma}^{\mathrm{tip}} \bar{f}^+_{\mathrm{tip}}(H_{10})\right] \rho_0 \\ &+ \mathrm{Tr}\left[\Gamma^{\mathrm{sub}} \bar{f}^-_{\mathrm{sub}}(H_{10}) \rho^1\right] + \mathrm{Tr}\left[\bar{f}^-_{\mathrm{tip}}(H_{10}) \Gamma^{\mathrm{tip}}_{01} \rho^1\right], \end{aligned} \tag{A.6}$$

where for the first two terms we used the fact that Γ^{sub} and $\bar{f}^+_\eta$ are diagonal and for $\Gamma^{\mathrm{tip}}_{01}$ everything except the diagonal part is traceless. For the fourth term we used that $\bar{f}^-_{\mathrm{tip}}$ is diagonal and the cyclic property of the trace, the fifth term vanishes since $\bar{p}_{\mathrm{tip}}$ is diagonal and by also using the cyclic property of the trace. With similar arguments we find for Eq. (4.22)

$$\begin{aligned} \dot{\rho}^2 = &- \left[2\bar{\Gamma}^{\mathrm{sub}} \bar{f}^-_{\mathrm{sub}}(H_{21}) + 2\bar{\Gamma}^{\mathrm{tip}} \bar{f}^-_{\mathrm{tip}}(H_{21})\right] \rho^2 \\ &+ \mathrm{Tr}\left[\Gamma^{\mathrm{sub}} \bar{f}^+_{\mathrm{sub}}(H_{21}) \rho^1\right] + \mathrm{Tr}\left[\bar{f}^+_{\mathrm{tip}}(H_{21}) \Gamma^{\mathrm{tip}}_{12} \rho^1\right]. \end{aligned} \tag{A.7}$$

Eq. (4.23) adopts the following form

$$\begin{aligned} \dot{\rho}^1 = &- \frac{\mathrm{i}}{\hbar}\left[\hat{H}_1, \rho^1\right] \\ &- \sum_\eta \frac{1}{2}\left\{\bar{f}^-_\eta(H_{10})\left\{\Gamma^\eta_{01}, \rho^1\right\} - \frac{\mathrm{i}}{\pi}\bar{\mathrm{p}}_\eta(H_{10})\left[\Gamma^\eta_{01}, \rho^1\right]\right\} \\ &- \sum_\eta \frac{1}{2}\left\{\bar{f}^+_\eta(H_{21})\left\{\Gamma^\eta_{12}, \rho^1\right\} - \frac{\mathrm{i}}{\pi}\bar{\mathrm{p}}_\eta(H_{21})\left[\Gamma^\eta_{12}, \rho^1\right]\right\} \\ &+ \sum_\eta \bar{f}^+_\eta(H_{10})\Gamma^\eta_{01}\rho^0 + \sum_\eta \bar{f}^-_\eta(H_{21})\Gamma^\eta_{12}\rho^2, \end{aligned} \tag{A.8}$$

where we rewrite the hermitian conjugate as an anticommutator for the Fermi functions and a commutator for the principal parts. The commutators in the last two lines vanish because $\bar{\mathrm{p}}_\eta$ is proportional to the identity.
Now we start to reformulate the equations in terms of the populations and the pseudospin. Since ρ^0 and ρ^2 only contain one element we can just rewrite

$$P_0 = \rho^0 \quad \text{and} \quad P_2 = \rho^2. \tag{A.9}$$

For ρ_1 we use the decomposition introduced in Eq. (4.25)

$$\rho_1 = \frac{P_1}{2}\mathbb{1}_2 + \tau_x\sigma_x + \tau_y\sigma_y + \tau_z\sigma_z = \frac{P_1}{2}\mathbb{1}_2 + \boldsymbol{\tau}\cdot\boldsymbol{\sigma}, \tag{A.10}$$

with

$$P_1 = \operatorname{Tr}\rho^1 \tag{A.11}$$

and

$$\tau_i = \frac{1}{2}\operatorname{Tr}\left\{\rho^1\sigma_i\right\} = \langle\hat{\tau}_i\rangle\,. \tag{A.12}$$

Furthermore we use the form of the tunnelling rate matrices in terms of the pseudospin polarization

$$\begin{aligned}\bar{\Gamma}^\eta_{01} &= \bar{\Gamma}^\eta\left(\mathbb{1}_2 + \mathbf{P}^\tau_\eta\cdot\boldsymbol{\sigma}\right)\\ \bar{\Gamma}^\eta_{21} &= \bar{\Gamma}^\eta\left(\mathbb{1}_2 - \mathbf{P}^\tau_\eta\cdot\boldsymbol{\sigma}\right),\end{aligned} \tag{A.13}$$

where $\mathbf{P}^\tau_{\mathrm{sub}} = 0$. With this we find for eq. (A.8)

$$\begin{aligned}\dot{P}_1 = &-\sum_\eta \bar{\Gamma}^\eta\left[\bar{f}^-_\eta(H_{10}) + \bar{f}^+_\eta(H_{21})\right]P_1\\ &+\sum_\eta 2\bar{\Gamma}^\eta\left[\bar{f}^+_\eta(H_{10})P_0 + \bar{f}^-_\eta(H_{21})P_2\right].\end{aligned} \tag{A.14}$$

The commutators vanish because $\bar{\mathrm{p}}_\eta$ is diagonal and the trace is invariant under cyclic permutations. For the anticommutators only the parts proportional to the identity survive since the Pauli matrices are trace less.
For the pseudospin part we need the relations

$$[\mathbf{a}\cdot\boldsymbol{\sigma}, \mathbf{b}\cdot\boldsymbol{\sigma}] = 2\mathrm{i}(\mathbf{a}\times\mathbf{b})\cdot\boldsymbol{\sigma} \tag{A.15}$$

and

$$\{\mathbf{a}\cdot\boldsymbol{\sigma}, \mathbf{b}\cdot\boldsymbol{\sigma}\} = 2\mathbf{a}\cdot\mathbf{b}. \tag{A.16}$$

With this we find

$$\begin{aligned}\dot{\boldsymbol{\tau}} =& \frac{1}{2}\,\mathrm{Tr}\left\{\rho^1\boldsymbol{\sigma}\right\} = \\ & \omega\left(\mathbf{n}_{\mathrm{mol}}\times\boldsymbol{\tau}\right) - \frac{\bar{\Gamma}^{\mathrm{tip}}}{\pi}\Big[\bar{\mathrm{p}}_\eta(H_{10}) - \bar{\mathrm{p}}_\eta(H_{21})\Big]\mathbf{P}^\tau_{\mathrm{tip}}\times\boldsymbol{\tau} \\ & - \frac{1}{2}\sum_\eta \bar{f}^-_\eta(H_{10})\bar{\Gamma}^\eta\left[P_1\mathbf{P}^\tau_\eta + \boldsymbol{\tau}\right] - \frac{1}{2}\sum_\eta \bar{f}^+_\eta\bar{\Gamma}^\eta\left[-P_1\mathbf{P}^\tau_\eta + \boldsymbol{\tau}\right] \\ & + \bar{\Gamma}^{\mathrm{tip}}\Big[\bar{f}^+_{\mathrm{tip}}(H_{10})P_0 - \bar{f}^-_{\mathrm{tip}}(H_{21})P_2\Big]\mathbf{P}^\tau_{\mathrm{tip}}.\end{aligned} \tag{A.17}$$

Acknowledgments

First and foremost I am deeply grateful to my supervisor Andrea Donarini for countless hours of help, discussions, encouragement and always having a positive mindset towards this project. It was a pleasure to work with you for the past year and I am looking forward on continuing working together.
Furthermore, I want to thank Milena Grifoni for nurturing a very nice atmosphere in her research group, always having a friendly ear and interesting discussions.
A big thank you is in order to my office mates Jakob Schlör, Christoph Rohrmeier and Thomas Naimer. It was a pleasure sharing this office with you for the past year and our undertakings out of the university were always a good retreat from the sometimes frustrating world of science.
A big thank you to Vanessa Junk, Jakob Schlör, Lotte Frankerl and Luca Magazzu for proofreading the manuscript and providing very valuable criticism.
The corner crew Andreas Haag, Christian Baumgartner, Lorenz Fuchs and Thomas Huber, of course has to be also mentioned here. The amount of bullshit which can exit your mouths is astonishing but very much entertaining.
Of those guys I still have to highlight Andreas "Mausi" Haag who essentially suffered with me through shockingly many years of studying. Thanks for sticking with me in the good and bad times in these past years and on many more to come!
Thanks to Maria Camarasa for convincing me to stay for my doctorate and randomly cheering me on in times of stress. Little things can make a big difference.
Special thanks to my girlfriend Antonia for being the awesome person she is and always believing in my ability to finish this thesis.
I want to thank my mother, Beate Metzger, and my sister, Lotte Frankerl for support in all kind of ways. Without you I could not have made it through the last years.

References

[1] G. E. Moore, IEEE solid-state circuits society newsletter **11**, 33 (2006).

[2] L. Eeckhout, IEEE Micro **37**, 4 (2017).

[3] A. Aviram and M. A. Ratner, Chemical Physics Letters **29**, 277 (1974).

[4] C. Joachim, J. K. Gimzewski, R. R. Schlittler, and C. Chavy, Phys. Rev. Lett. **74**, 2102 (1995).

[5] R. H. M. Smit, Y. Noat, C. Untiedt, N. D. Lang, M. C. van Hemert, and J. M. van Ruitenbeek, Nature **419**, 906 (2002).

[6] B. Xu and N. J. Tao, Science **301**, 1221 (2003).

[7] M. Thoss and F. Evers, The Journal of Chemical Physics **148**, 030901 (2018).

[8] Y. Xue, S. Datta, and M. A. Ratner, Chemical Physics **281**, 151 (2002).

[9] G. Cuniberti, G. Fagas, and K. Richter, *Introducing molecular electronics: A brief overwiev* (Springer, 2006).

[10] E. Scheer and J. Cuevas, *Molecular electronics: an introduction to theory and experiment* (World Scientific, 2017).

[11] G. Binnig, H. Rohrer, C. Gerber, and E. Weibel, Phys. Rev. Lett. **49**, 57 (1982).

[12] A. M. Baró, R. Miranda, J. Alamán, N. García, G. Binnig, H. Rohrer, C. Gerber, and J. L. Carrascosa, Nature **315**, 253 (1985).

[13] O. Dulub, L. A. Boatner, and U. Diebold, Surface Science **519**, 201 (2002).

[14] W. Steurer, J. Repp, L. Gross, I. Scivetti, M. Persson, and G. Meyer, Phys. Rev. Lett. **114**, 036801 (2015).

[15] I.-W. Lyo and P. Avouris, Science **253**, 173 (1991).

[16] B. C. Stipe, M. A. Rezaei, and W. Ho, Science **280**, 1732 (1998).

[17] M. Hangyo, M. Tani, and T. Nagashima, International Journal of Infrared and Millimeter Waves **26**, 1661 (2005).

[18] K. Yoshioka, I. Katayama, Y. Minami, M. Kitajima, S. Yoshida, H. Shigekawa, and J. Takeda, Nature Photonics **10**, 762 (2016).

[19] T. L. Cocker, V. Jelic, M. Gupta, S. J. Molesky, J. A. Burgess, G. De Los Reyes, L. V. Titova, Y. Y. Tsui, M. R. Freeman, and F. A. Hegmann, Nature Photonics **7**, 620 (2013).

[20] T. L. Cocker, D. Peller, P. Yu, J. Repp, and R. Huber, Nature **539**, 263 (2016).

[21] G. Czycholl, *Theoretische Festkörperphysik Band 1* (Springer, 2016).

[22] M. Born and R. Oppenheimer, Annalen der Physik **389**, 457 (1927).

[23] B. Siegert, "STM transport through copper phthalocyanine on thin insulating films", PhD thesis (University of Regensburg, 2015).

[24] J. C. Slater and G. F. Koster, Phys. Rev. **94**, 1498 (1954).

[25] W. B. Jensen, Journal of Chemical Education **90**, 802 (2013).

[26] S. Froyen and W. A. Harrison, Phys. Rev. B **20**, 2420 (1979).

[27] B. Siegert, A. Donarini, and M. Grifoni, Beilstein Journal of Nanotechnology **6**, 2452 (2015).

[28] M.-S. Liao and S. Scheiner, The Journal of Chemical Physics **114**, 9780 (2001).

[29] M. J.B., *Atomic structure calculations. I.Hartree-Fock energy results for the elements hydrogen to lawrencium*, tech. rep. (Los Alamos Scientific Laboratory of the University of California, 1967).

[30] F. Evangelista, V. Carravetta, G. Stefani, B. Jansik, M. Alagia, S. Stranges, and A. Ruocco, The Journal of Chemical Physics **126**, 124709 (2007).

[31] C. Uhlmann, I. Swart, and J. Repp, Nano Letters **13**, 777 (2013).

[32] D. De Oteyza, A. El-Sayed, J. Garcia-Lastra, E. Goiri, T. Krauss, A. Turak, E. Barrena, H. Dosch, J. Zegenhagen, A. Rubio, et al., The Journal of chemical physics **133**, 214703 (2010).

[33] J. Bendix, M. Brorson, and C. E. Schaffer, Inorganic Chemistry **32**, 2838 (1993).

[34] J. Bardeen, Physical Review Letters **6**, 57 (1961).

[35] S. Sobczyk, "STM transport theory for π-conjugated molecules on thin insulating films", PhD thesis (Universität Regensburg, 2012).

[36] K. Blum, *Density Matrix Theory and Applications* (Springer, 2012).

[37] C. Timm, Phys. Rev. B **77**, 195416 (2008).

[38] H.-P. Breuer and F. Petruccione, *The theory of open quantum systems* (Oxford University Press on Demand, 2002).

[39] S. Koller, "Spin phenomena and higher order effects in transport across interacting quantum-dots", PhD thesis (University of Regensburg, 2010).

[40] G. Begemann, D. Darau, A. Donarini, and M. Grifoni, Phys. Rev. B **77**, 201406 (2008).

[41] S. Sobczyk, A. Donarini, and M. Grifoni, Phys. Rev. B **85**, 205408 (2012).

[42] A. Altibelli, C. Joachim, and P. Sautet, Surface science **367**, 209 (1996).

[43] J. Repp, G. Meyer, S. M. Stojković, A. Gourdon, and C. Joachim, Phys. Rev. Lett. **94**, 026803 (2005).

[44] K. Kaasbjerg and K. Flensberg, Phys. Rev. B **84**, 115457 (2011).

[45] B. Siegert, A. Donarini, and M. Grifoni, Phys. Rev. B **93**, 121406 (2016).

[46] R. Ulbricht, E. Hendry, J. Shan, T. F. Heinz, and M. Bonn, Rev. Mod. Phys. **83**, 543 (2011).

[47] P. U. Jepsen, D. G. Cooke, and M. Koch, Laser & Photonics Reviews **5**, 124 (2011).

[48] S. Grafström, Journal of Applied Physics **91**, 1717 (2002).

[49] M. G. Schultz and F. von Oppen, Phys. Rev. B **80**, 033302 (2009).

[50] I. B. Bersuker, Chemical Reviews **101**, PMID: 11709858, 1067 (2001).

Erklärung

Ich habe diese Arbeit selbständig verfasst und keine anderen als die angegebenen Quellen und Hilfsmittel verwendet und nicht an einer anderen Hochschule zur Erlangung eines akademischen Grades eingereicht. Die vorgelegten Druckexemplare sind identisch mit der vorgelegten elektronischen Version der Arbeit. Ich wurde über wissenschaftlich korrektes Arbeiten und Zitieren aufgeklärt und kenne die Rechtsfolgen nach §24 Abs. 5.

Moritz Frankerl